Title
Fundamental and in situ Microscopy Studies of III-V Nanoscale Wires and Particles

Author
Ngo, Chilan

Publication Date
2015

Peer reviewed|Thesis/dissertation

UNIVERSITY OF CALIFORNIA

Los Angeles

Fundamental and *in situ* Microscopy Studies of III-V Nanoscale Wires and Particles

A dissertation submitted in partial satisfaction of the

Requirements for the degree of Doctor of Philosophy

in Materials Science and Engineering

by

Chilan Ngo

2015

ABSTRACT OF THE DISSERTATION

Fundamental and *in situ* Microscopy Studies

of III-V Nanoscale Wires and Particles

by

Chilan Ngo

Doctor of Philosophy in Materials Science and Engineering

University of California, Los Angeles, 2015

Professor Suneel K. Kodambaka, Chair

In this work, I first demonstrate the synthesis of ternary III-V alloy (e.g., InPSb) nanowires via self-catalyzed vapor-liquid-solid (VLS) growth techniques using indium catalyst, which then promotes inquiry into the physical properties of a similar catalyst seed material (e.g., gallium) in an effort to elucidate key parameters for potentially tuning particle size, and consequently wire size. Understanding the behavior of group III metals such as droplets provides fundamental insight into liquid-catalyzed nanowire growth. Mechanistic insight on gallium droplet growth and evaporation kinetics is ascertained by systematic variation of parameters coupled with the use of powerful techniques such as *in situ* transmission electron microscopy (TEM) and focused ion beam (FIB) milling. Observing the kinetics of pure gallium in contrast with gallium containing a native oxide shell, in addition to growth and diffusion studies of gallium droplets, facilitates knowledge integration towards an interconnected development

continuum route as proposed by the Materials Genome Initiative (MGI). Herein, I demonstrate the integration of synthetic and analytical techniques to synergistically form the basis towards obtaining a general, fundamental understanding of particle growth systems. Obtaining a mechanistic understanding of particle evolution/devolution by synergistically employing computational and analytical methods will advance nanotechnology and materials science by promoting a drive towards the intuitive design of next-generation, application-specific materials with enhanced properties for future applications, rather than relying on their serendipitous discovery through trial and error.

The dissertation of Chilan Ngo is approved.

Mark S. Goorsky

Brian C. Regan

Suneel K. Kodambaka, Committee Chair

University of California, Los Angeles

2015

To Beep, for a decade of support and sanity

TABLE OF CONTENTS

LIST OF FIGURES

LIST OF TABLES

ACKNOWLEDGEMENT

First of all, I would like to thank my advisor, Professor Suneel Kodambaka, for supervision, flexibility, and support during my pursuit of various research and collaborative projects. Also, I gratefully acknowledge Professors Mark Goorsky, Chris Regan, and Yu Huang for graciously serving as members of my dissertation committee.

I am indebted to Noah Bodzin, Dr. Sergey Prikhodko, Dr. Arie Venkart, Dr. Matt Mecklenburg, Dr. Marta Pozuelo, and Dr. Ivo Atanisov for both friendship and providing foundation for my pursuit of electron microscopy techniques. I am also thankful to Dr. Esther Lan for years of labwork and teaching together, as well as her wholehearted support for any of my endeavors. To my collaborators and friends, I am deeply grateful for your brilliance, hard work, and enthusiasm for working with me: Dr. Justinas Palisaitas, Dr. Jeremy Leong, soon-to-be-Dr. Steve Hawks, Dr. Tara Yoder, Dr. Joshua Shapiro, Dr. Baolai Liang, and all other colleagues, as well as the supervisors who made all of our work possible, notably Professors Per Persson, Ryan Richards, and Cristian Ciobanu.

To my group members/mentors/Drs., Jeung Hun Park, Abbas Ebnonassir, and Saurabh Sharma, I would not have survived without your ideas and moral support through the passage of my PhD. For the surviving and past group members, it has been an immense pleasure to have you sticking with me, brightening the lab, and continuing the legacy of Kodambaka Science: Sing Mok, Dian Yu, Mikey Chin, Pedro Arias, Josh Fankhauser, An-Di Sheu, Hongyan Lee, Dr. Jon Quan, *et al*. Also, my beloved former undergraduate "minions" cannot by forgotten: Dean Cheik, Phil Depond, Edit Ovasapyan, and Linda Wong. I look forward to seeing each of your careers develop!

Finally, my deepest gratitude goes to the unwavering love and support of my family and friends. Fellow MSE graduate students (especially the Dungeon crew): you are many and unjustly unnamed, but your friendship has kept the dream alive and I hope that my presence in E-V has been as uplifting to you as yours have been to me. Above all, I would like to thank my parents and brother for neverending encouragement, inspiration, deliveries of homemade Vietnamese food, and all else done to keep me both literally and figuratively alive – this journey would have been impossible without you.

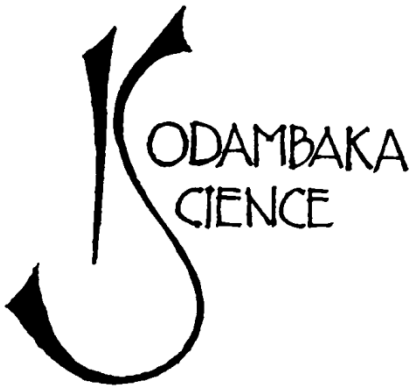

VITA

2009	B.S., Chemistry/Materials Science, Organic Concentration University of California, Los Angeles
2012	M.S., Materials Science and Engineering University of California, Los Angeles

Publications

- C. Ngo and S. Kodambaka, "*In situ* Transmission Electron Microscopy Observations of Ga Dynamics on Focused Ion Beam Milled Surfaces" *In progress*
- C. Ngo and S. Kodambaka, "*In situ* Studies of Gallium Droplet Evaporation and Influence of Atmospheric Oxidation" *In progress*
- Y. Ji, G. J. Leong, C. Ngo, M. Menart, S. Kodambaka, & R. M. Richards, "Palladium Nanoparticles Intercalated in Mesoporous Silica as a Robust Catalyst System" *In progress*
- S.A. Hawks, G. Zhang, C. Ngo, D.T. Scholes, H. Kang, J.C. Aguirre, S.H. Tolbert, & B.J. Schwartz, "Extensive Penetration of Evaporated Metal into Fullerene Films: Nanostructure and Influence on Device Architecture" *In progress*
- T.S. Yoder, J.E. Cloud, G.J. Leong, D.F. Molk, M. Tussing, J. Moirelli, C. Ngo, S. Kodambaka, M.E. Eberhart, R.M. Richards, and Y. Yang, "Iron pyrite nanocrystal inks: Solvothermal synthesis, digestive ripening, and reaction mechanism" *Chemistry of Materials*, **26** 6743-6751 (2014).

- J.P. Bell, J.E. Cloud, J. Cheng, C. Ngo, S. Kodambaka, A. Sellinger, S.K.R. Williams, and Y. Yang, "N-bromosuccinimide-based bromination and subsequent functionalization of hydrogen-terminated silicon quantum dots" *RSC Advances* **4**, 51105-51110 (2014).
- G.J. Leong, A. Ebnonnasir, M.C. Schulze, M.B. Strand, C. Ngo, D. Maloney, S.L. Frisco, H.N. Dinh, B. Pivovar, G.H. Gilmer, S. Kodambaka, C.V. Ciobanu, and R.M. Richards, "Shape-directional growth of Pt and Pd nanoparticles" *Nanoscale* **6**, 11364-11371 (2014).
- Jouanny, J. Palisaitis, C. Ngo, P.H. Mayrhofer, L. Hultman, P.O.Å. Persson, and S. Kodambaka, "*In situ* transmission electron microscopy studies of the kinetics of Pt-Mo alloy diffusion in ZrB_2 thin films" *Applied Physics Letters* **103**, 121601 (2013).
- S. Kodambaka, C. Ngo, J. Palisaitis, P.H. Mayrhofer, L. Hultman, and P.O.Å. Persson, "Kinetics of Ga droplet decay on thin carbon films" *Applied Physics Letters* **102**, 161601 (2013).
- C. Ngo, H. Zhou, M. Mecklenburg, M. Pozuelo, B.C. Regan, Q.F. Xiao, V.B. Shenoy, R.F. Hicks, and S. Kodambaka, "Effect of precursor flux on compositional evolution in $InP_{1-x}Sb_x$ nanowires grown via self-catalyzed vapor-liquid-solid process" *Journal of Crystal Growth* **336**, 14-19 (2011).
- Y. Liu, J. Hu, C. Ngo, S. Prikhodko, S. Kodambaka, J. Li, and R. Richards, "Gram-scale wet chemical synthesis of wurtzite-8H nanoporous ZnS spheres with high photo catalytic activity" *Applied Catalysis B: Environmental* 106, 212-219 (2011).

CHAPTER 1 INTRODUCTION

1.1 Overview

The focus of this work is to study III-V nanowire growth and liquid metal catalyst kinetics via microscopy. Understanding group III behavior, particular in the form of droplets, provides fundamental insight into nanowire growth. Fundamental understanding is one of the crucial steps to developing any emerging technology, and the implementation of new materials and devices is best done in conjunction with studying the basic processes controlling material properties. For instance, semiconducting nanowires may be fabricated into numerous devices based solely on observation of how they function as products. However, maximum efficiency is obtained when fundamental properties of the nanomaterials themselves are studied, understood, and then applied. One of these fundamental and highly-studied topics is to understand growth mechanisms controlling the wide variety of nanoscale materials in the literature, as well as to understand dynamics of catalyst materials that facilitate growth of these functional nanomaterials.

1.2 III-V nanowires via VLS growth

The development of semiconducting nanowires has been groundbreaking in the pursuit of both fundamental knowledge and the creation of an extensive variety of applications, particularly in electronic and energy-related fields.[1–3] The field of nanowires is broad to the point of taking another review paper to tabulate the reviews to-date. One 2004 review notes an "overwhelming number of articles" just on the synthesis of one-dimensional nanostructures in the year prior to its publication.[4] Just over ten years later, the field continues to expand. A vast range of optoelectronic, electromechanical, photonic, and other devices has been fabricated using nanowires of various morphologies and compositions as key building blocks;[5,6] these

applications include solar cells,[7–11] field-effect transistors,[12–14] LEDs,[15–18] lasers,[19–22] and biosensors.[23–25] Nanowires of group III-V materials (e.g., alloys of Al/Ga/In and N/P/As/Sb) in particular exhibit electrical and optical properties that make them ideal for a wide variety of fields. However, the exact mechanisms controlling growth – as well as the ideal applications of these mechanisms – are still a current topic of exploration and debate. Of widespread interest is the understanding and systematic control of nanowire size, composition, morphology, and structure as a function of growth conditions: time, temperature, type of catalyst, substrate material and patterning, etc.[26–28] III-V nanowires in particular, as opposed to simpler materials such as Si and Ge, exhibit a wide range of growth behaviors and resultant properties. One such variation is the growth of minority crystal phases instead of the bulk phase of the material (i.e., between zinc blende and wurtzite), which is a function of growth parameters such as temperature and precursor flux.

Common nanowire growth techniques include bottom-up methods such as metalorganic chemical vapor deposition (MOCVD),[29–31] molecular-beam epitaxy (MBE),[31–34] solution phase growth,[35–36] and aerosol growth,[37] as well as laser ablation for controlled top-down synthesis.[38–40] Bottom-up methods commonly employ the vapor-liquid-solid (VLS) mechanism due to its flexibility, relative ease of use, and high rate of success in producing large quantities of single-crystalline nanowires.[3,4,41] In this broadly-used approach first proposed by Wagner and Ellis,[42] a liquid catalyst droplet is used to promote 1D growth of a solid phase through a controlled supply of precursors in the vapor phase. VLS growth is able to produce nanowires with high uniformity in nanoscale diameter and with extended length scales past one micron.[4]

1.3 Liquid droplet catalysts via for VLS

One of the key components of the VLS growth system is the liquid droplet catalyst, which directly controls or influences the resultant nanowire size, location, structure, morphology, and growth direction.[3,43,44] For example, stability of the catalyst-nanowire interface during isothermal growth is necessary to avoid undesirable features such as kinking,[45] while supersaturation of the catalyst (among other things) may cause thermodynamically less stable crystal phases to precipitate into the nanowire.[46–48] Diameter of nanowires is controlled by the catalyst diameter, which has been tuned in some materials to grow nanowires of specific size – a necessary property for precision-controlled synthesis of nanoscale devices, such as high-efficiency nanowire-based solar cells.[49–51]

Due to the crucial nature of the catalyst to nanowire growth, studying liquid catalyst metals such as Au or group III elements gives necessary insight into catalyst behavior. Although Au was the first widespread catalyst for VLS growth, foreign metals may contaminate and reduce the quality of semiconducting nanostructures. For instance, Au catalysts for Si nanowires may introduce mid-bandgap electronic states that degrade carrier mobility.[52,53] To avoid foreign catalysts, other materials are now commonly used to facilitate self-catalyzed growth – notably the group III element in III-V materials (e.g., Ga for GaAs and In for InP). Understanding the behavior of group III metals such as droplets provides fundamental insight into nanowire growth.

1.4 *In situ* microscopy

Of the many techniques used to characterize nanowires and other nanoscale materials, the electron microscope is a key tool for understanding fundamental properties and behavior. *In situ* electron microscopy studies in particular have given unique and critical insight on material

growth,[54–56] beginning around the 1950s with *in situ* observations of evaporated metal films.[57] Nanowire growth in particular has gained valuable mechanistic insight from *in situ* transmission electron microscopy (TEM) experiments, notably with the first direct, visual demonstration of VLS growth with Au-catalyzed Ge wires[58] and more recently with atomic resolution observation of layer-by-layer sapphire growth at the catalyst-nanowire interface, mediated by a liquid Al catalyst.[59] *In situ* microscopy studies specifically involving Ga droplets include the study of droplet size distribution[60] and "running" surface droplets on GaAs,[61] which provide insight on epitaxy, nanoscale fabrication techniques, droplet kinetics, and growth of related III-V materials.

1.5 Gallium

Two of the most powerful uses of Ga are as the liquid catalyst for self-catalyzed III-V nanowire growth, and as the most common ion source for focused ion beam (FIB) milling.[62] Low-melting metals such as gallium and related alloys have also received significant attention due to their unique physical and chemical properties that drive several emerging technologies.[63] A few attractive properties include low vapor pressure, excellent wettability, and good thermal and electrical conductivities, which can be employed in a variety of applications such as hydrogen- and energy-storage materials,[64] alloying additives – notably for energy applications,[65–72] coolants in microelectronics,[63,73–76] and in nuclear reactors.[77,78] More recently, nanoscale gallium particles have been shown to have promising material characteristics for the use in mercury-free nanoscale temperature sensors and electrical switches,[79–82] plasmonics,[72,83–91] "self-healing" Li-battery electrodes,[92–95] and catalysts for growth of not only nanowires[97,98] but also graphene.[98–102]

1.6 Scope of dissertation

This dissertation addresses research performed using electron microscopy and spectroscopy techniques to investigate the growth and dynamics of group III-V nanowires and group III liquid droplets. Following the introductory chapter, the second chapter examines growth of InPSb "nanocream cone" nanowires in light of precursor flux and the existence of an unexpected crystal phase found at the droplet-wire interface. The third chapter focuses on the evaporation behavior and influence of native oxide on Ga droplets deposited via molecular beam epitaxy and heated *in situ*. Next, the fourth chapter investigates the dynamics of Ga droplets produced by *in situ* heating of FIB cross-sections, notably droplet decay via Ostwald ripening. In the fifth chapter, the prior investigation is extended to include droplet dynamics of Ga over a range of times and temperatures, and includes investigation of "pure" Ga droplets versus oxidized droplets in the third chapter. In the sixth chapter, conclusions and future work are discussed for results presented in the previous chapters.

1.7 References

1 L. Samuelson, C. Thelander, M. T. Björk, M. Borgström, K. Deppert, K. A. Dick, A. E. Hansen, T. Mårtensson, M. Panev, A. I. Persson, W. Seifert, N. Sköld, M. W. Larsson, and L. R. Wallenberg, "Semiconductor nanowires for 0D and 1D physics and applications" *Physica E: Low-dimensional Systems and Nanostructures* **25**, 313–318 (2004).

2 H. J. Fan, P. Werner, and M. Zacharias, "Semiconductor Nanowires: From Self-Organization to Patterned Growth" *Small* **2**, 700–717 (2006).

3 A. I. Hochbaum and P. Yang, "Semiconductor Nanowires for Energy Conversion" *Chem. Rev*. **110**, 527–546 (2010).

4 M. Law, J. Goldberger, and P. Yang, "Semiconductor Nanowires and Nanostructures" *Annu. Rev. Mater. Res*. **34**, 83 (2004).

5 Y. Huang, X. Duan, Y. Cui, L. J. Lauhon, K.-H. Kim, and C. M. Lieber, "Logic Gates and Computation from Assembled Nanowire Building Blocks" *Science* **9**, 1313–1317 (2001).

6 X. Duan, Y. Huang, Y. Cui, J. Wang, and C. M. Lieber, "Indium phosphide nanowires as building blocks for nanoscale electronic and optoelectronic devices" *Nature* **409**, 66–69 (2001).

7 B. Tian, X. Zheng, T. J. Kempa, Y. Fang, N. Yu, G. Yu, J. Huang, and C. M. Lieber, "Coaxial silicon nanowires as solar cells and nanoelectronic power sources" *Nature* **449**, 885–889 (2007).

8 B. Tian, T. J. Kempa, and C. M. Lieber, "Single nanowire photovoltaics" *Chem. Soc. Rev.* **38**, 16–24 (2009).

9 Y. Dong, B. Tian, T. J. Kempa, and C. M. Lieber, "Coaxial group III—nitride nanowire photovoltaics" *Nano Lett.* **9**, 2183–7 (2009).

10 M. D. Kelzenberg, D. B. Turner-Evans, B. M. Kayes, M. A. Filler, M. C. Putnam, N. S. Lewis, and H. A. Atwater, "Photovoltaic measurements in single-nanowire silicon solar cells" *Nano Lett.* **8**, 710–4 (2008).

11 R. R. LaPierre, A. C. E. Chia, S. J. Gibson, C. M. Haapamaki, J. Boulanger, R. Yee, P. Kuyanov, J. Zhang, N. Tajik, N. Jewell, and K. M. A. Rahman, "III–V nanowire photovoltaics: Review of design for high efficiency" *Phys. Status Solidi RRL* **7**, 815–830 (2013).

12 Y. Cui, Z. Zhong, D. Wang, W. U. Wang, and C. M. Lieber, "High Performance Silicon Nanowire Field Effect Transistors" *Nano Lett.* **3**, 149–152 (2003).

13 T. Bryllert, L. E. Wernersson, L. E. Froberg, and L. Samuelson, "Vertical high-mobility wrap-gated InAs nanowire transistor" *IEEE Electron Device Lett.* **27**, 323–5 (2006).

14 S. Vandenbrouck, K. Madjour, D. Theron, Y. Dong, Y. Li, C. M. Lieber, and C. Gaquiere, "12 GHz *F*MAX GaN/AlN/AlGaN nanowire MISFET" *IEEE Electron Device Lett.* **30**, 322–4 (2009).

15 F. Qian, S. Gradecak, Y. Li, C. Y. Wen, and C. M. Lieber, "Core/multishell nanowire heterostructures as multicolor, high-efficiency light-emitting diodes" *Nano Lett.* **5**, 2287–91 (2005).

16 E. D. Minot, F. Kelkensberg, M. vanKouwen, J. A. vanDam, L. P. Kouwenhoven, V. Zwiller, M. T. Borgstrom, O. Wunnicke, M. A. Verheijen, and E. P. A. M. Bakkers, "Single quantum dot nanowire LEDs" *Nano Lett.* **7**, 367–71 (2007).

17 C. P. T. Svensson, T. Mårtensson, J. Trägårdh, C. Larsson, M. Rask, D. Hessman, L. Samuelson, and J. Ohlsson, "Monolithic GaAs/InGaP nanowire light emitting diodes on silicon" *Nanotech.* **19**, 305201 (2008).

18 J. Tatebayashi, A. Lin, P. S. Wong, R. F. Hicks, and D. L. Huffaker, "Visible light emission from self-catalyzed GaInP/GaP core-shell double heterostructure nanowires on silicon" *J. Appl. Phys.* **108**, 034315 (2010).

19 M. H. Huang, S. Mao, H. Feick, H. Yan, Y. Wu, H. Kind, E. Weber, R. Russo, and P. Yang, "Room-temperature ultraviolet nanowire nanolasers" *Science* **292**, 1897–1899 (2001).

20 X. Duan, Y. Huang, R. Agarwall, and C. M. Lieber, "Single-nanowire electrically driven lasers" *Nature* **421**, 241–245 (2003).

21 S. Gradecak, F. Qian, Y. Li, H. -G. Park, and C. M. Lieber, "GaN nanowire lasers with low lasing thresholds" *Appl. Phys. Lett.* **87** 173111 (3 pp) (2005).

22 M. A. Zimmler, J. Bao, F. Capasso, S. Muller, and C. Ronning, "Laser action in nanowires: observation of the transition from amplified spontaneous emission to laser oscillation" *Appl. Phys. Lett.* **93** 051101–3 (2008).

23 F. Patolsky, G. Zheng, O. Hayden, M. Lakadamyali, X. Zhuang, and C. M. Lieber, "Electrical detection of single viruses" *Proc. Nat. Ac. Sci. Un. Stat. Am.* **101**, 14017–14022 (2004).

24 G. Zheng, F. Patolsky, Y. Cui, W. U. Wang, and C. M Lieber, "Multiplexed electrical detection of cancer markers with nanowire sensor arrays" *Nat. Biotech.* **23**, 1294–1301 (2005).

25 N. L. Rosi and C. A. Mirkin, "Nanostructures in Biodiagnostics" *Chem. Rev.* **105**, 1547–1562 (2005).

26 S. A. Dayeh, E. T. Yu, and D. Wang, "III-V nanowire growth mechanism: V/III ratio and temperature effects" *Nano Lett.* **7**, 2486-2490 (2007).

27 K. A. Dick, P. Caroff, J. Bolinsson, M. E. Messing, J. Johansson, K. Deppert, L. R. Wallenberg, and L. Samuelson, "Control of III–V nanowire crystal structure by growth parameter tuning" *Semiconductor Sci. Tech.* **25**, 024009 (2010).

28 J. Johansson, L. S. Karlsson, C. P. T. Svensson, T. Mårtensson, B. A. Wacaser, K. Deppert, L. Samuelson, and W. Seifert, "Structural properties of ⟨111⟩ B-oriented III–V nanowires" *Nature Mater.* **5**, 574-580 (2006).

29 K. Hiruma, H. Murakoshi, M. Yazawa, and T. Katsuyama, "Self-organized growth of GaAsInAs heterostructure nanocylinders by organometallic vapor phase epitaxy" *J. Cryst. Growth* **163**, 226–231 (1996).

30 W. Seifert, M. Borgström, K. Deppert, K. A. Dick, J. Johansson, M. W. Larsson, T. Mårtensson, N. Sköld, C. P. T. Svensson, B. A. Wacaser, L. R. Wallenberg, and L. Samuelson, "Growth of one-dimensional nanostructures in MOVPE" *J. Cryst. Growth* **272**, 211–220 (2004).

31 J. Johansson, B. A. Wacaser, K. A. Dick, and W. Seifert, "Growth related aspects of epitaxial nanowires" *Nanotech.* **17**, S355 (2006).

32 M. Piccin, G. Bais, V. Grillo, F. Jabeen, S. De Franceschi, E. Carlino, M. Lazzarino, F. Romanato, L. Businaro, S. Rubini, F. Martelli, and A. Franciosi, "Growth by molecular beam epitaxy and electrical characterization of GaAs nanowires" *Phys. E* **37**, 134–7 (2007).

33 Z. H. Wu, X. Mei, D. Kim, M. Blumin, H. E. Ruda, J. Q. Liu and K. L. Kavanagh, "Growth, branching, and kinking of molecular-beam epitaxial <1 1 0> GaAs nanowires" *Appl. Phys. Lett.* **83**, 3368–70 (2003).

34 P. Krogstrup, R. Popovitz-Biro, E. Johnson, M. H. Madsen, J. Nygård, and H. Shtrikman, "Structural Phase Control in Self-Catalyzed Growth of GaAs Nanowires on Silicon (111)" *Nano Lett.* **10**, 4475–4482 (2010).

35 T. J. Trentler, K. M. Hickman, S. C. Goel, A. M. Viano, P. C. Gibbons, and W. E. Buhro, "Solution-Liquid-Solid Growth of Crystalline Ill-V Semiconductors: An Analogy to Vapor-Liquid-Solid Growth" *Science* **270**, 1791–1794 (1995).

36 J. D. Holmes, K. P. Johnston, R. C. Doty and B. A. Korgel, "Control of thickness and orientation of solution-grown silicon nanowires" *Science* **287**, 1471–3 (2000).

37 M. Heurlin, M. H. Magnusson, D. Lindgren, M. Ek, L. R. Wallenberg, K. Deppert, K., and L. Samuelson, "Continuous gas-phase synthesis of nanowires with tunable properties" *Nature* **492**, 90–94 (2012).

38 X. Duan and C. M. Lieber, "Laser-assisted catalytic growth of single crystal GaN nanowires" *J. Am. Chem. Soc.* **122**, 188–9 (2000).

39 A. M. Morales and C. M. Lieber, "A Laser Ablation Method for the Synthesis of Crystalline Semiconductor Nanowires" *Science* **279**, 208–211 (1998).

40 D. P. Yu, C. S. Lee, I. Bello, X. S. Sun, Y. H. Tang, G. W. Zhou, Z. G. Bai, Z. Zhang, and S. Q. Feng, "Synthesis of nano-scale silicon wires by excimer laser ablation at high temperature" *Solid State Comm.* **105**, 403–407 (1998).

41 S. A. Fortuna and X. Li, "Metal-catalyzed semiconductor nanowires: a review on the control of growth directions" *Semicond. Sci. Technol.* **25**, 024005(16pp) (2010).

42 R. S. Wagner and W. C. Ellis, "The VLS mechanism of whisker growth. " *Trans. Met. Soc. AIME* **233**, 1054 (1965).

43 M. S. Song, J. H. Jung, Y. Kim, Y. Wang, J. Zou, H. J. Joyce, Q. Gao, H. H. Tan and C. Jagadish, "Vertically standing Ge nanowires on GaAs(110) substrates" *Nanotechnology* **19,** 125602 (2008).

44 K. A. Dick, K. Deppert, L. Samuelson, L. R. Wallenberg and F. M. Ross, "Control of GaP and GaAs nanowire morphology through particle and substrate chemical modification" *Nano Lett.* **8** 4087–91 (2008).

45 R. S. Wagner and C. J. Ooherty, "Mechanism of branching and kinking during VLS crystal growth" *J. Electrochem. Soc.* **115**, 93–9 (1968).

46 F. Glas, J.-C. Harmand, and G. Patriarche, "Why does wurtzite form in nanowires of III-V zinc blende semiconductors?" *Phys. Rev. Lett.* **99**, 146101 (2007).

47 K. A. Dick, P. Caroff, J. Bolinsson, M. E. Messing, J. Johansson, K. Deppert, L. R. Wallenberg, and L. Samuelson, "Control of III–V nanowire crystal structure by growth parameter tuning" *Semicon Sci. and Tech.* **25**, 024009 (2010).

48 C. Ngo, H. Zhou, M. Mecklenburg, M. Pozuelo, B. C. Regan, Q. F. Xiao, V. B. Shenoy, R. F. Hicks, and S. Kodambaka, "Effect of precursor flux on compositional evolution in $InP_{1-x}Sb_x$ nanowires grown via self-catalyzed vapor–liquid–solid process" *J. Cryst. Growth* **336**, 14–19 (2011).

49 M. S. Gudiksen and C. M. Lieber, "Diameter-selective synthesis of semiconductor nanowires" *J. Am. Chem. Soc.* **122**, 8801–2 (2000).

50 Y. Wu, H. Yan, M. Huang, B. Messer, J. H. Song, and P. Yang, "Inorganic semiconductor nanowires: rational growth, assembly, and novel properties" *Chem. Eur. J.* **8**, 1260–68 (2002).

51 F. Matteini, V. G. Dubrovskii, D. Rüffer, G. Tütüncüog˘lu, Y. Fontana, and A. F. I. Morral, "Tailoring the diameter and density of self-catalyzed GaAs nanowires on silicon" *Nanotechnology* **26**, 105603 (8pp) (2015).

52 T. Kamins, "Semiconductor nanowires for electronics and sensors" *WE-Heraeus Semin. Semiconducting Nanowires: Physics, Materials and Devices* **397,** (2007).

53 T. I. Kamins, R. Stanley Williams, Y. Chen, Y-L. Chang, and Y. A. Chang, "Chemical vapor deposition of Si nanowires nucleated by $TiSi_2$ islands on Si" *Applied Physics Letters* **76**, 562–564 (2000).

54 C. Y. Wen, M. C. Reuter, J. Bruley, J. Tersoff, S. Kodambaka, E. A. Stach, and F. M. Ross, "Formation of compositionally abrupt axial heterojunctions in silicon-germanium nanowires" *Science* **326**, 1247–1250 (2009).

55 F. M. Ross, "Controlling nanowire structures through real time growth studies" *Rep. Prog. Phys.* **73**, 114501 and references therein (2010).

56 L. E. Martin, K. Deppert, L. Samuelson, and L. R. Wallenberg, "Straight and kinked InAs nanowire growth observed *in situ* by transmission electron microscopy " *Nano Research* **7**, 1188–1194 (2014).

57 T. A. McLauchlan, R. S. Sennett, and G. D. Scott, "Continuous observations with the electron microscope on the formation of evaporated films of silver, gold, and tin" *Canadian J. Res.* **28**, 530–534 (1950).

58 Y. Wu and P. Yang, "Direct observation of vapor-liquid-solid nanowire growth" *J. Am. Chem. Soc*. **123**, 3165–66 (2001).

59 S. H. Oh, M. F. Chisholm, Y. Kauffmann, W. D. Kaplan, W. Luo, M. Rühle, and C. Scheu, "Oscillatory Mass Transport in Vapor-Liquid-Solid Growth of Sapphire Nanowires" *Science* **22**, 489–493 (2010).

60 Z. Y. Zhou, W. X. Yang, D. E. Jesson, and J. Tersoff, "Time evolution of the Ga droplet size distribution during Langmuir evaporation of GaAs(001)" *App. Phys. Lett.* **97**, 191914 (2010).

61 J. Tersoff, D. E. Jesson, and W. X. Tang, "Running Droplets of Gallium from Evaporation of Gallium Arsenide" *Science* **324**, 236–238 (2009).

62 L. A. Giannuzzi and F. A. Stevie, eds, "Introduction to focused ion beams: instrumentation, theory, techniques and practice" *Springer Science & Business Media* (2005).

63 V. Y. Prokhorenko, V. V. Roshchupkin, M. A. Pokrasin, S. V. Prokhorenko, and V.V. Kotov, "Liquid Gallium: Potential Uses as a Heat-Transfer Agent" *High Temp.* **38**, 954–968 (2000).

64 B. Sakintuna, F. Lamari-Darkrim, and M. Hirscher, "Metal hydride materials for solid hydrogen storage: A review" *Int. J. Hydrogen Energy* **32**, 1121–1140 (2007).

65 T. Ueno and S. Yamada, "Performance of energy harvester using iron–gallium alloy in free vibration" *Magnetics, IEEE Transactions on* **47**, 2407–2409 (2011).

66 S. Ahmed, K. B. Reuter, Q. Huang, H. Deligianni, L. T. Romankiw, S. Jaime, and P. P. Grand, "Electrodeposited Gallium Alloy Thin Films Synthesized by Solid State Reactions for CIGS Solar Cell" *J. Electrochem. Soc.* **159**, D129–D134 (2011).

67 X. -D. Niu, H. Yamaguchi, X.-J. Ye, and Y. Iwamoto, "Characteristics of a MHD power generator using a low-melting-point Gallium alloy" *Elect. Eng.* **96**, 37–43 (2014).

68 E. Altamirano, J. A. de los Reyes, F. Murrieta, and M. Vrinat, "Hydrodesulfurization of 4, 6–dimethyldibenzothiophene over Co (Ni) MoS_2 catalysts supported on alumina: Effect of gallium as an additive" *Cat. Today* **133**, 292–298 (2008).

69 J. N. D. de León, M. Picquart, M. Villarroel, M. Vrinat, F. J. Gil Llambias, F. Murrieta, and J. A. De Los Reyes, "Effect of gallium as an additive in hydrodesulfurization WS 2/γ-Al 2 O 3 catalysts" *J. Mol. Ca. A: Chemical* **323**, 1–6 (2010).

70 Q. Li and N. J. Bjerrum, "Aluminum as anode for energy storage and conversion: a review" *J. Power Sources* **110**, 1–10 (2002).

71 M. Paramasivam, M. Jayachandran, and S. V. Iyer, "Influence of alloying additives on the performance of commercial grade aluminium as galvanic anode in alkaline zincate solution for use in primary alkaline batteries" *J. App. Electrochem.* **33**, 303–309 (2003).

72 J. V. Naidich and J. N. Chuvashov, "Wettability and contact interaction of gallium-containing melts with non-metallic solids" *J. Mat. Sci.* **18**, 2071–2080 (1983).

73 H. Ge and Jing Liu, "Keeping smartphones cool with gallium phase change material" *J. Heat Transfer* **135**, 054503 (2013).

74 Y. -G. Deng and J. Liu, "Corrosion development between liquid gallium and four typical metal substrates used in chip cooling device" *Appl. Phys. A* **95**, 907–915 (2009).

75 K. -Q. Ma and J. Liu, "Heat-driven liquid metal cooling device for the thermal management of a computer chip" *J. Phys. D: Appl. Phys.* **40**, 4722 (2007).

76 K. -Q. Ma, and J. Liu, "Liquid metal cooling in thermal management of computer chips" *Frontiers Energy Power Eng. China* **1**, 384–402 (2007).

77 S. D. Park and I. C. Bang, "Feasibility of flooding the reactor cavity with liquid gallium coolant for IVR-ERVC strategy" *Nucl. Engi. Desi.* **258**, 13–18 (2013).

78 T. Sawada, A. Netchaev, H. Ninokata, and H. Endo, "Gallium-cooled liquid metallic-fueled fast reactor" *Prog. Nucl. Energy* **37**, 313–319 (2000).

79 Y. Gao and Y. Bando, "*Nanotechnology*: Carbon nanothermometer containing gallium" *Nature* **415**, 599 (2002).

80 Z. Liu, Y. Bando, J. Hu, K. Ratinac, and S. P. Ringer, "A novel method for practical temperature measurement with carbon nanotube nanothermometers" *Nanotechno.* **17**, 3681 (2006).

81 Y. B. Li, Y. Bando, D. Golberg, and Z. W. Liu, "Ga-filled single-crystalline MgO nanotube: Wide-temperature range nanothermometer" *App. Phys. Lett.* **83**, 999–1001 (2003).

82 P. S. Dorozhkin, S. V. Tovstonog, D. Golberg, J. Zhan, Y. Ishikawa, M. Shiozawa, H. Nakanishi, K. Nakata, and Y. Bando, "A Liquid-Ga-Filled Carbon Nanotube: A Miniaturized Temperature Sensor and Electrical Switch" *Small* **1**, 1088–1093 (2005).

83 M. Losurdo, C. Yi, A. Suvorova, S. Rubanov, T. -H. Kim, M. M. Giangregorio, W. Jiao, A. V. Krasavin, and N. I. Zheludev, "Active plasmonics: Controlling signals in Au/Ga waveguide using nanoscale structural transformations" *App. Phys. Lett.* **84**, 1416–1418 (2004).

84 P. C. Wu, T. -H. Kim, A. S. Brown, M. Losurdo, G. Bruno, and H. O. Everitt, "Real-time plasmon resonance tuning of liquid Ga nanoparticles by *in situ* spectroscopic ellipsometry" *App. Phys. Lett.* **90**, 103119 (2007).

85 P. C. Wu, C. G. Khoury, T. -H. Kim, Y. Yang, M. Losurdo, G. V. Bianco, T. Vo-Dinh, A. S. Brown, and H. O. Everitt, "Demonstration of surface-enhanced Raman scattering by tunable, plasmonic gallium nanoparticles" *J. Am. Chem. Soc.* **131**, 12032–12033 (2009).

86 P. Albella, B. Garcia-Cueto, F. González, F. Moreno, P. C. Wu, T. -H. Kim, A. Brown, Y. Yang, H. O. Everitt, and G. Videen, "Shape matters: plasmonic nanoparticle shape enhances interaction with dielectric substrate" *Nano Lett.* **11**, 3531–3537 (2011).

87 S. R. C. Vivekchand, C. J. Engel, S. M. Lubin, M. G. Blaber, W. Zhou, J. Y. Suh, G. C. Schatz, and T. W. Odom, "Liquid Plasmonics: Manipulating Surface Plasmon Polaritons via Phase Transitions" *Nano Lett.* **12**, 4324–4328 (2012).

88 C. W. Yi, T. H. Kim, W. Y. Jiao, Y. Yang, A. Lazarides, K. Hingerl, G. Bruno, A. Brown, and M. Losurdo, "Evidence of Plasmonic Coupling in Gallium Nanoparticles/Graphene/SiC" *Small* **8**, 2721–2730 (2012).

89 Y. Yang, J. M. Callahan, T. -H. Kim, A. S. Brown, and H. O. Everitt, "Ultraviolet nanoplasmonics: A demonstration of surface-enhanced Raman spectroscopy, fluorescence, and photodegradation using gallium nanoparticles" *Nano Lett.* **13**, 2837–2841 (2013).

90 I. Bergmair, G. Bruno, and A. S. Brown, "Demonstrating the Capability of the High-Performance Plasmonic Gallium–Graphene Couple" *ACS Nano* **8**, 3031–3041 (2014).

91 M. W. Knight, T. Coenen, Y. Yang, B. J. M. Brenny, M. Losurdo, A. S. Brown, H. O. Everitt, and A. Polman, "Gallium Plasmonics: Deep Subwavelength Spectroscopic Imaging of Single and Interacting Gallium Nanoparticles" *ACS Nano* **9**, 2049–2060 (2015).

92 W. Liang, L. Hong, H. Yang, F. Fan, Y. Liu, H. Li, J. Li, J. Y. Huang, L. -Q. Chen, T. Zhu, and S. Zhang, "Nanovoid Formation and Annihilation in Gallium Nanodroplets under Lithiation–Delithiation Cycling" *Nano Lett.* **13**, 5212–5217 (2013).

93 D. Deshpande, J. C. Li, Y. T. Cheng, and M. W. Verbrugge, "Liquid Metal Alloys as Self-Healing Negative Electrodes for Lithium Ion Batteries" *J. Electrochem. Soc.* **158**, A845–A849 (2011).

94 M. Yarema, M. Wörle, M. D. Rossell, R. Erni, R. Caputo, L. Protesescu, K. V. Kravchyk, D. N. Dirin, K. Lienau, F. von Rohr, A. Schilling, M. Nachtegaal, and M. V. Kovalenko, "Monodisperse Colloidal Gallium Nanoparticles: Synthesis, Low Temperature Crystallization, Surface Plasmon Resonance and Li-Ion Storage" *J. Am. Chem. Soc.* **136**, 12422–12430 (2014).

95 K. T. Lee, Y. S. Jung, T. Kim, C. H. Kim, J. H. Kim, J. Y. Kwon, and S. M. Oh, "Liquid gallium electrode confined in porous carbon matrix as anode for lithium secondary batteries" *Electrochem. Solid-State Lett.* **11**, A21–A24. (2008).

96 Z. W. Pan, Z. R. Dai, C. Ma, and Z. L. Wang, "Molten Gallium as a Catalyst for the Large-Scale Growth of Highly Aligned Silica Nanowires" *J. Am. Chem. Soc.* **124**, 1817–1822 (2002).

97 J. Fujita, R. Ueki, Y. Miyazawa, and T. Ichihashi, "Graphitization at interface between amorphous carbon and liquid gallium for fabricating large area graphene sheets" *J. Vac. Sci. Technol. B* **27**, 3063–3066 (2009).

98 I. Zardo, L. Yu, S. Conesa-Boj, S. Estradé, P. J. Alet, J. Rössler, M. Frimmer, P. R. I Cabarrocas, F. Peiró, J. Arbiol, J. R. Morante, and A. F. I Morral, "Gallium assisted plasma enhanced chemical vapor deposition of silicon nanowires" *Nanotech.* **20**, 155602 (2009).

99 J.-I Fujita, Y. Miyazawa, R. Ueki, M. Sasaki, and T. Saito, "Fabrication of Large-Area Graphene Using Liquid Gallium and Its Electrical Properties" *Jap. J. App. Phys.* **49**, 06GC01 (2010).

100 T. Hatakeyama, R. Kometani, S. Warisawa, and S. Ishihara, "Selective graphene growth from DLC thin film patterned by focused-ion-beam chemical vapor deposition" *J. Vac. Sci. Tech. B* **29**, 06FG04 (2011).

101 H. Hiura, M. V. Lee, A. V. Tyurnina, and K. Tsukagoshi, "Liquid phase growth of graphene on silicon carbide" *Carbon* **50**, 5076–5084 (2012).

102 G. Ding, Y. Zhu, S. Wang, Q. Gong, L. Sun, T. Wu, X. Xie, and M. Jiang, "Chemical vapor deposition of graphene on liquid metal catalysts" *Carbon* **53**, 321–326 (2013).

CHAPTER 2 EFFECT OF PRECURSOR FLUX ON COMPOSITIONAL EVOLUTION IN $INP_{1-X}SB_X$ NANOWIRES GROWN via SELF-CATALYZED VAPOR-LIQUID-SOLID PROCESS

A paper published in Journal of Crystal Growth, reproduced by license agreement 3622680804757 with Elsevier. DOI: 10.1016/j.jcrysgro.2011.09.043 (article) *J. Cryst. Growth* **2011**, *336*, 14–19

Chilan Ngo, Hailong Zhou, Matthew Mecklenburg, Marta Pozuelo, B. C. Regan, Q. F. Xiao, V. B. Shenoy, R. F. Hicks, S. Kodambaka

2.1 Abstract

We investigated the effect of high flow rates (> 10^{-5} mol/min) of metalorganic precursors on compositional evolution in indium phosphide antimonide ($InP_{1-x}Sb_x$) nanowires grown via chemical vapor deposition in the presence of indium droplets as catalysts on InP(111)B substrates maintained at ~ 360 °C. The as-grown nanowire morphology, composition, and crystallinity are determined using scanning and transmission electron microscopies, selected-area electron diffraction, and x-ray energy-dispersive spectroscopy. Irrespective of the precursor flow rates, we obtain zinc blende structured $InP_{1-x}Sb_x$ wires that are tapered with wider tops, narrower bases, and In-rich In-Sb alloy tips, as is characteristic of the vapor-liquid-solid process. The Sb content within the $InP_{1-x}Sb_x$ wires is found to increase non-linearly with increasing Sb precursor flow rate. At the interfaces between the In-Sb alloy tips and the $InP_{1-x}Sb_x$ nanowires, we observe single-crystalline wurtzite-structured InSb segments whose volumes depend on the Sb precursor flow rate. We attribute this phenomenon to the rapid crystallization of InSb during cooling of the Sb-rich In-Sb alloy droplets.

2.2 Introduction

Multi-component alloys of group III-V semiconducting compounds with tunable optoelectronic properties[1] are attractive for applications in high-performance photodetectors, light emitting diodes, solar cells, and other devices.[2–6] Design and synthesis of these materials at the nanoscale, for example as nanowires, can, in principle, offer advantages over their bulk counterparts in improving their properties and hence the device efficiencies. Nanowires are commonly grown using an external metal catalyst such as gold via the vapor-liquid-solid (VLS) process[7] and/or its variants. For more details on growth-related aspects specific to group III-V nanowires, please see Ref. [8]. Over the past decade, single as well as multi-component alloy nanowires[9–11] and radial/axial nanowire heterostructures[12] of group III-V materials have been synthesized and characterized.[13–19] Among the group III-V semiconductors, growth and characterization of nanowires of Sb-based compounds have received little attention until recently despite their potential for applications in infra-red optics, magneto sensors, and thermophotovoltaics.[20] For example, nanowires of InSb, InAs/GaSb and InP/InSb heterostructures, and ternary alloys (InAsSb and InPSb) have been grown via VLS process.[10,18,21–26] In the InP-InSb system, where the miscibility gap is large,[27,28] Zhou *et al.*[25] demonstrated that self-catalyzed VLS process[29] can be used to controllably vary the morphology, crystallinity, and composition of $InP_{1-x}Sb_x$ alloy nanostructures. Here, we focus on the influence of precursor flux on the crystallinity and compositional uniformity along the $InP_{1-x}Sb_x$ alloy nanowires.

In this paper, we present results from a detailed electron microscopic characterization of $InP_{1-x}Sb_x$ alloy nanowires grown as a function of Sb precursor flow rate on InP(111)B substrates in presence of liquid indium droplets with all the group III and V precursors introduced at high

flow rates (> 10–^{5} mol/min). All of the as-grown nanowires are tapered with wider tops and narrower bases, exhibit zinc blende (ZB) structure, and are composed of $InP_{1-x}Sb_x$ alloys. At the nanowire tips, we observe In-rich In-Sb alloys. And, at the wire-tip interfaces, we find InSb single-crystalline segments with wurtzite (WZ) structure. With increasing Sb precursor flow rate, we observe an increase in the Sb content within the wires as well as the InSb segment volume. Based upon our results, we suggest that the $InP_{1-x}Sb_x$ alloy nanowires grow via VLS process in presence of Sb-rich In-Sb alloy droplets which upon cooling yield WZ-InSb segments.

2.3 Materials and Methods

All of our growth experiments are carried out in a Veeco D125 MOVPE reactor using trimethylindium (TMIn), tertiarybutylphosphine (TBP), and trimethylantimonide (TMSb) as precursors, and InP(111)B as substrates. The details of the experimental procedure are presented in Ref. [29]. The substrates (~ 15 mm × 30 mm × 0.35 mm) are first loaded into the reactor and annealed at 550 °C in 1.34×10^{-3} mol/min of TBP for 5 min. Then, the substrate temperature is lowered to ~ 360 °C. (The absolute temperatures in our MOCVD reactor are accurate to within 25 K and the temperature is found to vary monotonically from the center to the edge of the substrate by about 60 K.) Indium droplets are deposited at ~ 360 °C by feeding 5.06×10^{-5} mol/min of TMIn for 12 s. Then, TMIn, TBP, and TMSb are introduced to initiate the growth of $InP_{1-x}Sb_x$ alloys. All the results reported in the following sections are obtained from three samples grown with TMIn and TBP flow rates held constant at 1.89×10^{-5} and 6.74×10^{-4} mol/min, respectively, and TMSb flow rates of Q = 4.9×10^{-5} mol/min, $2Q$ (= 9.8×10^{-5} mol/min), and $4Q$ (= 1.96×10^{-4} mol/min). These flow rates correspond to (P+Sb)/In molar ratios of 60, 62, and 69, respectively. The growth is terminated after 18 minutes by switching off the

precursors and cooling the sample to room temperature at ~ 40 K/min in an H_2 ambient maintained at 60 Torr.

The as-grown $InP_{1-x}Sb_x$ samples are examined first using scanning electron microscopy (SEM) in an FEI Nova NanoSEM 230 operated at an accelerating voltage of 10 keV. Individual nanostructures mechanically exfoliated from the growth wafer are further characterized using transmission electron microscopy (TEM), scanning TEM (STEM), selected area electron diffraction (SAED), and x-ray energy-dispersive spectroscopy (EDS) in an FEI Titan S/TEM operated at 300 keV. The SEM and TEM images are processed using ImageJ,[30] TEM Imaging & Analysis (TIA), and Digital Micrograph, as a means to determine the sizes, shapes, and crystal structures of the nanowires.

2.4 Results and Discussion

Based upon our previous studies, we know that the temperature can sensitively influence the growth morphology, composition, and crystal structure.[25,31] For the self-catalyzed growth of both InP and $InP_{1-x}Sb_x$, we found that the spatial variations in the observed morphologies as well as crystal structures arising due to differences in temperature across the substrate are qualitatively similar. In the present study we utilize one of the growth characteristics – specifically the morphology – to compare the nanowires grown at similar temperatures on different substrates. For each of the samples grown as a function of precursor flow rate, we chose nanowires grown near the center of the substrate and determined their tapering ratios, a measure of shape, as defined in the following section. Here, we limit our results and discussion to only those nanowires with similar tapering ratios, i.e. at similar temperatures.

Figures 2.1a-c are representative SEM images acquired from the three different InP(111)B samples grown using TMSb flow rates of Q, $2Q$, and $4Q$, respectively. We obtain nanowires, the majority of which are vertically oriented with respect to the substrate. Note the variation in wire densities across different samples, which is likely due to an uncontrolled coarsening of liquid indium droplets on unpatterned substrates with spatially varying step densities. All the nanowires grown at the centers of the samples are tapered with narrower bases and wider tops. In the VLS process, since the deposition flux is proportional to the surface area of the catalyst droplet, the observed tapering implies an increase in the size of the catalyst with time, which can occur if the rate of deposition into the catalyst exceeds the rate of precipitation out of the catalyst. From SEM images of 40–100 nanowires and TEM images of over 20 nanowires grown as a function of Q, we determined the average lengths L, base diameters D_{base}, top diameters D_{top}, and tapering ratios (defined as $[D_{top} - D_{base}/L]$) of the nanowires. We obtain (L, D_{base}, D_{top}) values of (464 ± 40 nm, 59 ± 12 nm, 122 ± 12 nm), (671 ± 69 nm, 89 ± 33 nm, 211 ± 20 nm), and (630 ± 128 nm, 91 ± 21 nm, 187 ± 16 nm), respectively for samples grown using Q, $2Q$, and $4Q$. The corresponding tapering ratios are 0.14 ± 0.01, 0.18 ± 0.02, 0.15 ± 0.03, respectively. The observed changes in the wire lengths and tapering ratios indicate that the volume growth rates increase with increasing TMSb flow rate from Q to $2Q$ but decrease upon increasing further from $2Q$ to $4Q$. All the nanowires regardless of the growth fluxes exhibit smoothly curved tips, characteristic of VLS growth. As we show below, these tips are composed of In-Sb alloys that presumably existed as liquid droplets during wire growth, consistent with previous studies.[25]

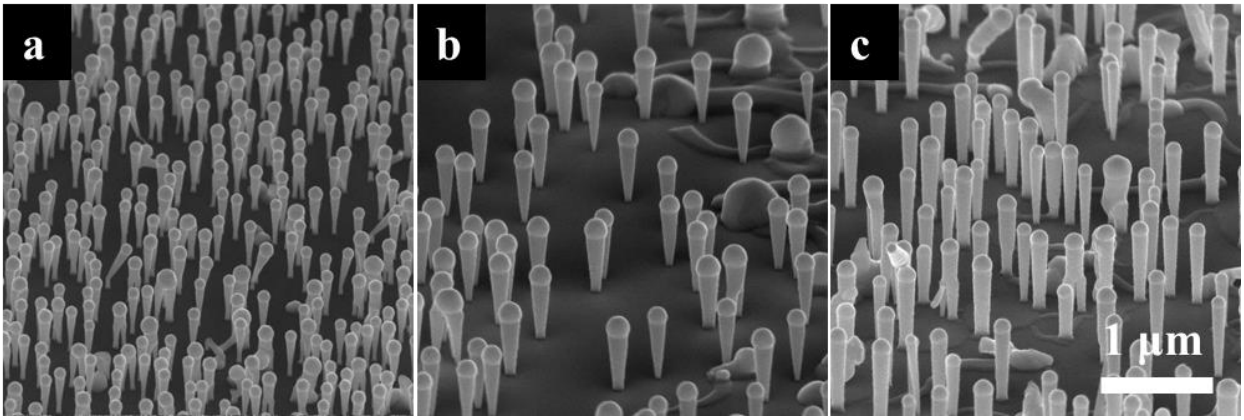

Figure 2.1 Representative scanning electron micrographs acquired at ~ 60° tilt from three InP(111)B substrates showing $InP_{1-x}Sb_x$ nanowires grown at ~ 360 °C using Sb precursor flow rates of (a) $Q = 4.9 \times 10^{-5}$, (b) 2*Q*, and (c) 4*Q* moles/min with P and In precursor flow rates held constant at 1.89×10^{-5} and 6.74×10^{-4} mol/min, respectively.

Figure 2.2a is a typical bright-field TEM image of an $InP_{1-x}Sb_x$ alloy nanowire grown using TMSb flow rate 4*Q*. The contrast variations within the wire are due to structural defects such as stacking faults and rotational twins, which are commonly observed in VLS-grown group III-V nanowires. The density of these defects, clearly visible in the higher resolution TEM image (Fig. 2.2b), varies from wire to wire and appear to be distributed randomly along the lengths of the wires. We have also observed defect-free regions within a few of the wires. We find alternating segments of rotational twins with varying widths along the wire length. While we did not observe twinning superlattices, the structures are qualitatively similar to those observed in other group III-V wires.[32,33]

Fig. 2.2c is a SAED pattern acquired along the zone axis [011] from a portion of the wire in Fig. 2.2a. From the diffraction data, we determine the crystal structure of the wire to be ZB. Fig. 2.2d shows EDS intensities of In-L, Sb-L, and P-K lines along the length of the wire (shown as an inset). EDS data reveals that the tip of the wire, i.e. the facetted catalyst particle, is composed primarily of In with ~ 4.0 at.% Sb. (A relatively high Sb concentration is also present at the catalyst/wire interface, which as shown later is due to the presence of InSb.) From similar

EDS data acquired from five nanowires grown using *Q*, 2*Q*, and 4*Q*, we estimate Sb contents of ~ 0, 3, and 4 at.%, respectively within the catalyst particles. The P content within the catalysts is negligible, consistent with previous reports.[25,26] These results indicate that the droplet composition varies with precursor flow rates with potentially important implications (discussed below) on the composition of the nanowires.

The Sb content in the nanowires is estimated using SAED data and Fourier transforms (FTs) of lattice-resolved TEM images.[34] We obtain lattice parameters of 5.93 ± 0.03 Å, 5.97 ± 0.04 Å, and 6.02 ± 0.14 Å for the wires grown using TMSb flow rates *Q*, 2*Q*, and 4*Q*, respectively. The data is obtained from 9 SAED patterns and 6 FTs. Assuming that the Vegard's law[35] is valid for InP-InSb system,[36–39] using the lattice constants of ZB-structured InP (5.87 Å) and InSb (6.48 Å),[40,41] the corresponding Sb concentrations (*x*) in the $InP_{1-x}Sb_x$ alloy wires are 10 ± 5 at.%, 16 ± 6 at.%, and 27 ± 22 at.%, respectively.[42] (The larger uncertainties associated with the Sb content in the 4*Q* wires are not an experimental error but are due to compositional oscillations along the nanowire growth direction.[43]) Fig. 2.3 shows Sb concentration *x* plotted as a function of *Q*. The data suggests that the Sb content in the wires increases with increasing TMSb flow rate from *Q* to 2*Q*. However, the effect of further increasing the flow rate on alloy composition is not clear.

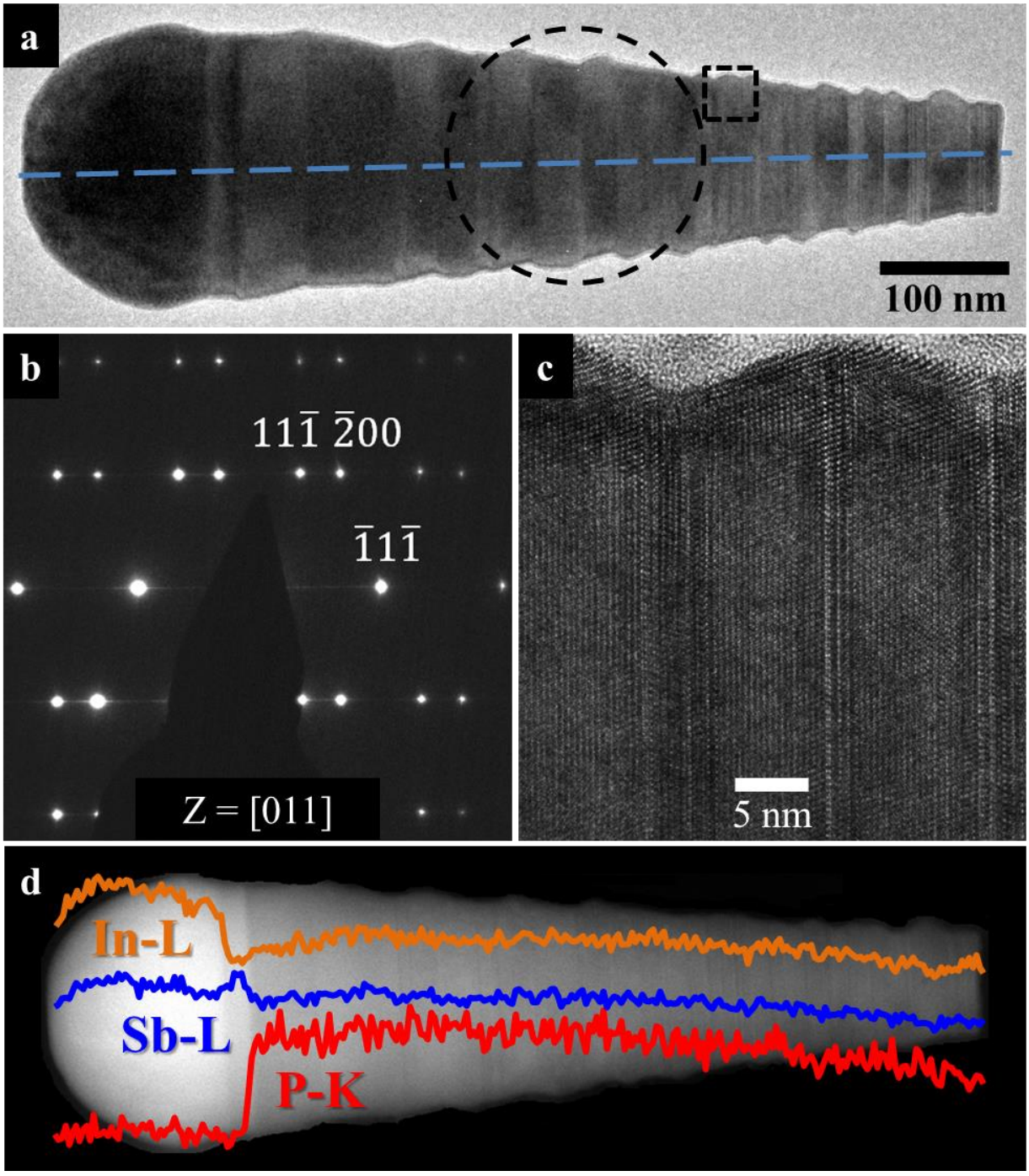

Figure 2.2 (a) Representative bright-field transmission electron micrograph (TEM) of an $InP_{1-x}Sb_x$ nanowire grown using 4*Q*. (b) Selected area electron diffraction (SAED) pattern from the region highlighted by a dotted circle (a), indexed as zinc blende in [011] zone axis. (c) Higher resolution TEM image of the rectangular region in (a). (d) X-ray energy-dispersive spectroscopy (EDS) data acquired along the dotted line on the nanowire in (a), superposed on scanning TEM (STEM) image of the wire. The orange, blue, and red curves are In-L, Sb-L, and P-K line intensities, respectively. Note the relatively higher concentration of Sb compared to P both in the droplet and at the droplet-wire interface.

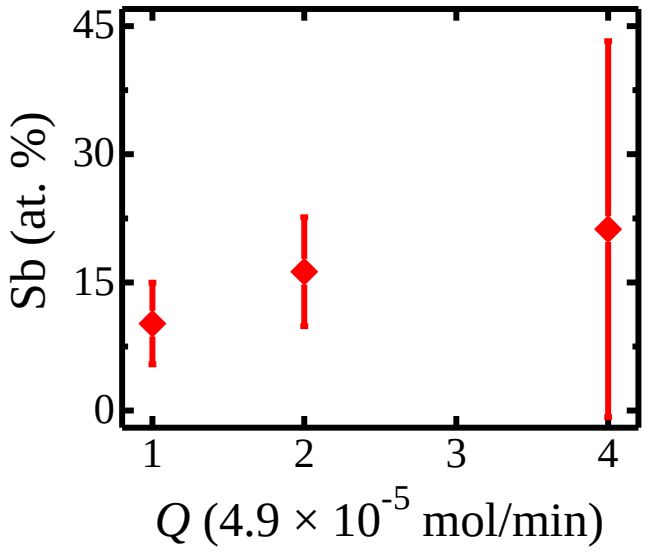

Figure 2.3 Plot of Sb content within the $InP_{1-x}Sb_x$ nanowires as a function of Sb precursor flow rate Q.

We now focus on the composition and structure of the nanowire/catalyst interface. Fig. 2.4a is a high-resolution TEM (HRTEM) image acquired at the interface of a nanowire grown at $Q = 4.9 \times 10^{-5}$ mol/min. We observe three structurally distinct regions, highlighted by dotted lines in Fig. 2.4a. A high-angle annular dark field (HAADF) STEM image (Fig. 2.4b) acquired from the same nanowire interface shows contrast changes in these three regions, indicating that the composition within these segments is also different. From selected area FTs of the image (Fig. 2.5), we identify the three regions as tetragonal-structured In-rich tip, WZ-structured InSb at the interface between the catalyst tip and the nanowire, and ZB-structured $InP_{1-x}Sb_x$ nanowire. For this particular nanowire, the width w of the WZ-InSb segment is 7.3 ± 0.3 nm. These results, i.e. the observation of WZ-InSb at the catalyst-wire interface, are typical of all wires grown at the three different Q values.

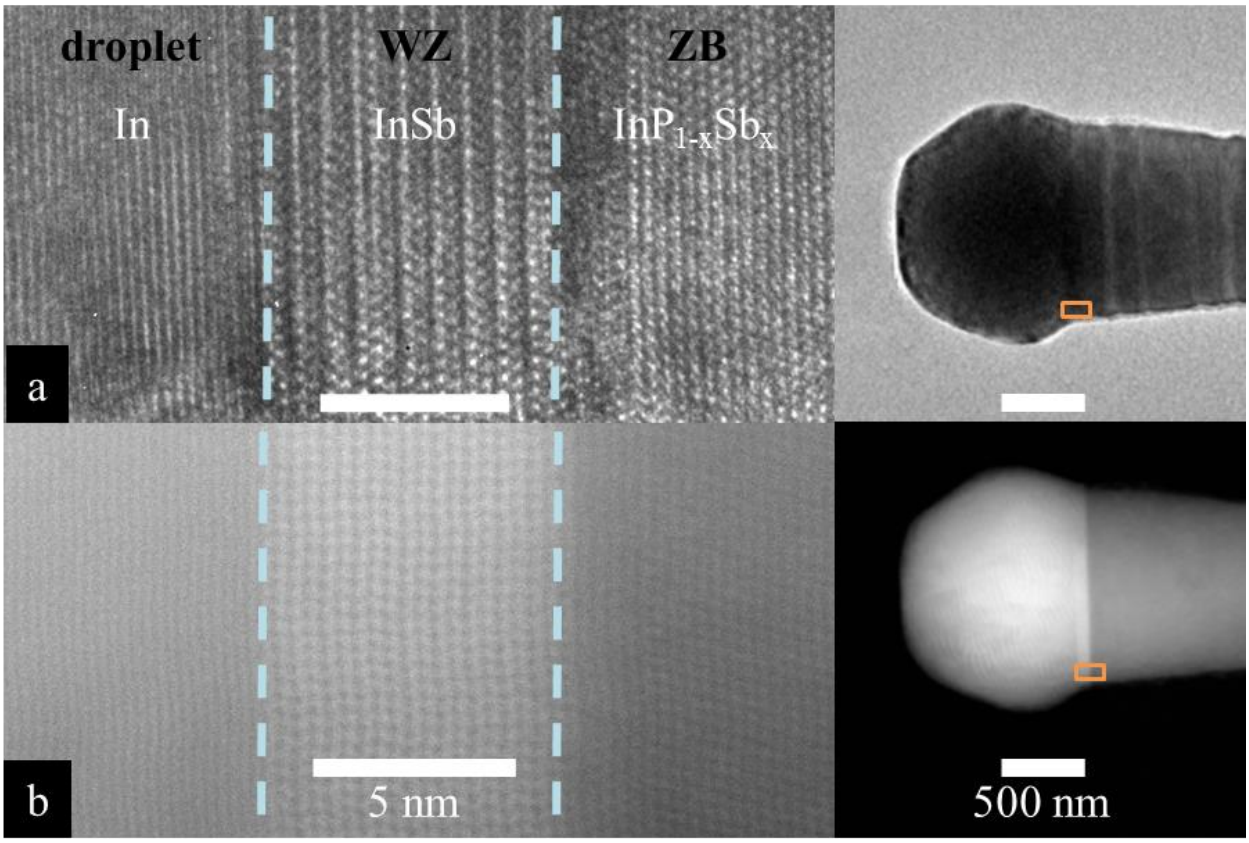

Figure 2.4 (a) Typical high resolution TEM and (b) high-angle annular dark field scanning TEM (HAADF-STEM) images of wire-tip interfaces in an $InP_{1-x}Sb_x$ nanowire grown using *Q*. The images are acquired from regions highlighted in the corresponding lower magnification TEM and STEM images shown as insets in (a) and (b), respectively. Dotted lines in both the images outline wurtzite-structured InSb present between the $InP_{1-x}Sb_x$ wire and the catalyst tip.

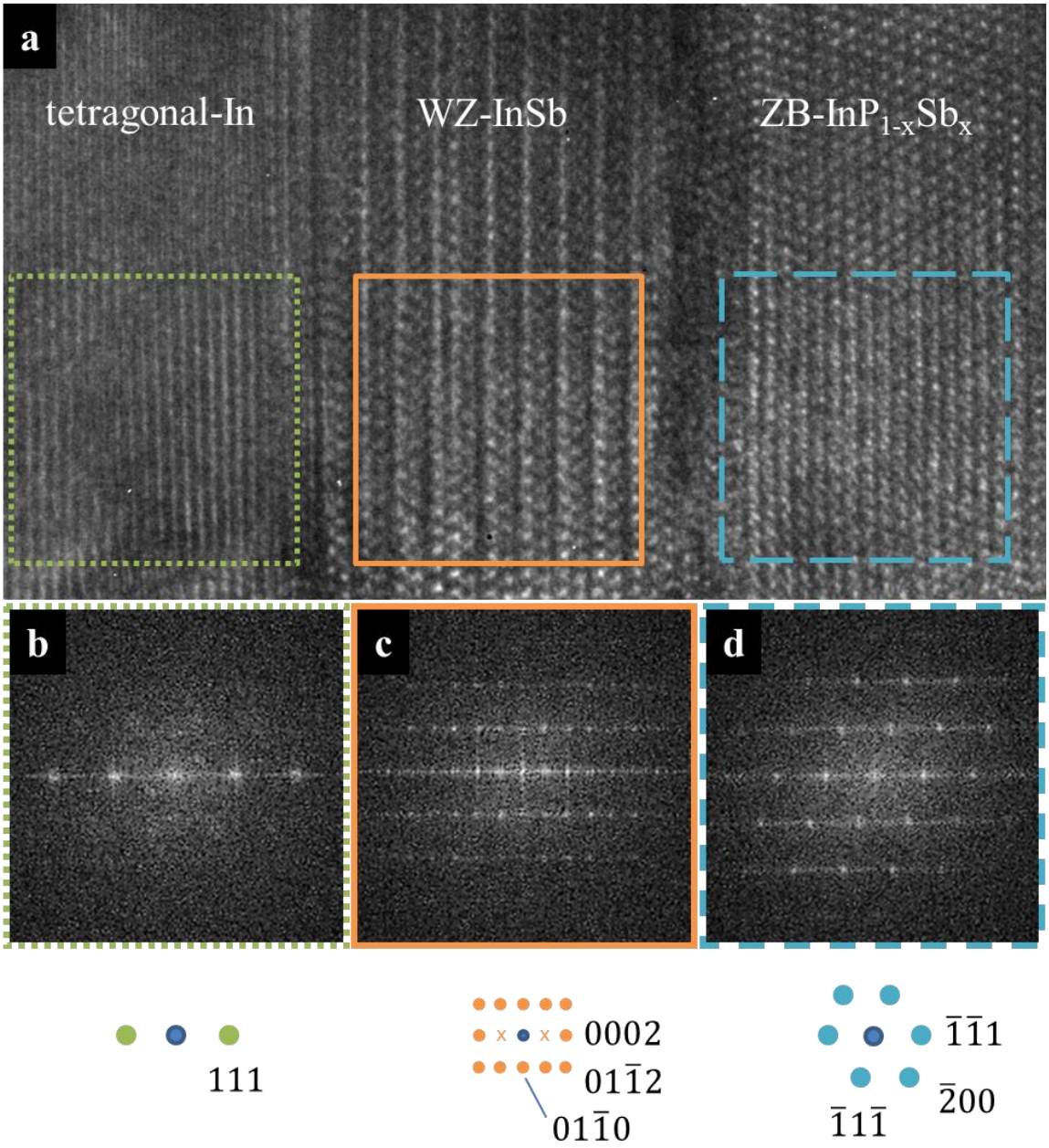

Figure 2.5 (a) A portion of the high resolution TEM image shown in Fig. 2.4a. (b) Fourier transforms of the three regions color coded for clarity in (a). The schematics at the bottom of the panel show the reciprocal lattices of the three structures.

The presence of WZ-phase InSb at the catalyst/$InP_{1-x}Sb_x$ nanowire interfaces is surprising since the growth experiments were carried out while flowing simultaneously all the three (In, P, and Sb) precursors. Moreover, these InSb segments were not observed in $InP_{1-x}Sb_x$ nanostructures grown using lower precursor flow rates in the *same* deposition system at similar

temperatures.[25] This result implies that the formation of InSb at the catalyst/wire interfaces is a direct consequence of increased flow rates of the precursors.

So, why does InSb form at the catalyst/wire interface? We suggest (and justify below) that the excess Sb present in the liquid In-Sb alloy droplets during $InP_{1-x}Sb_x$ nanowire growth precipitates out as InSb at the end of the deposition. In all of our experiments and previous studies,[25] EDS data revealed the presence of Sb and the absence of P in the wire tips. This is plausible since self-catalyzed growth of $InP_{1-x}Sb_x$ nanowires is likely to occur via VLS in presence of liquid droplets at the top of the nanowires. At thermodynamic equilibrium, liquid indium can dissolve ~ 13 at.% Sb and negligible amounts of P at the growth temperature of ~ 360 °C.[44] Such an In-Sb alloy liquid, when cooled to room temperature, is expected to yield two solid phases: In (74%) and InSb (26%). However, the VLS growth of nanowires is a dynamic process involving dissociative chemisorption of the precursors at the droplet surfaces and diffusional transport through the bulk of the droplets. Hence, the growth kinetics rather than thermodynamics is likely to control the droplet composition at the growth temperature as well as the relative phase fractions of the solids formed upon cooling. Under our growth conditions involving high flow rates of precursors, it is possible that the rate of deposition of Sb into the droplets exceeds the rate of incorporation into the wire resulting in high concentrations of Sb within the droplets. This is plausible because the relative rates of dissociative chemisorption of metalorganic precursors can vary with total pressure[45] and incorporation of Sb into the $InP_{1-x}Sb_x$ nanowires can be inhibited by the miscibility gap in the InP-InSb system.[27,28] When the growth is terminated by switching off the precursors and cooling the sample, this excess Sb precipitates out of the droplet as InSb at the droplet-wire interface. The amount of InSb deposited is a measure of the Sb present in the droplet during growth. Therefore, we measured the volumes of InSb

segments (calculated as $\pi w D_{top}^2/4$) present in the nanowires grown using different Qs. Fig. 2.6 shows the volume vs. Q data obtained from HRTEM measurements of 16 different wires. Clearly, the volumes of InSb formed at 2Q and 4Q are higher than that obtained in the nanowires grown with Q, consistent with the expectation that the Sb content in the droplets increases with increasing flow rate. These results provide further evidence to our hypothesis that higher precursor flow rates lead to the formation of InSb at the catalyst/wire interface.

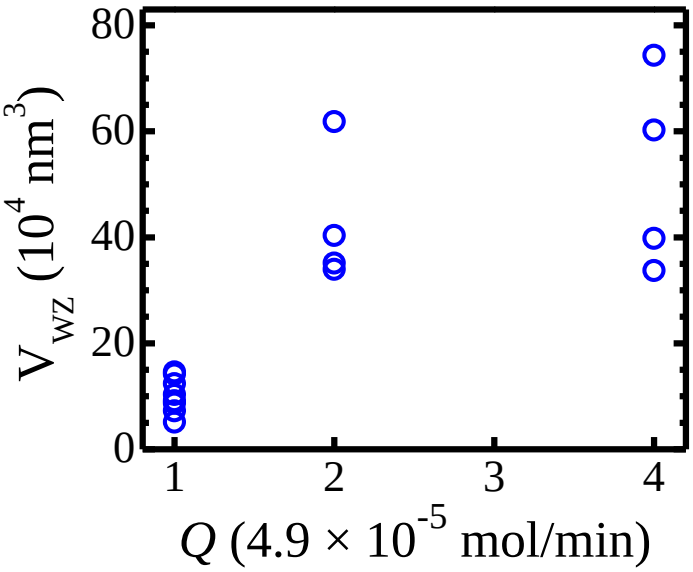

Figure 2.6 Plot of volume VWZ of the InSb segments as a function of Q. VWZ values are calculated from HRTEM measurements of the widths of InSb segment widths and assuming that they are cylindrical in shape.

Finally, we focus on the origin of WZ structure in these InSb segments given that ZB is the thermodynamically stable structure of bulk InSb. WZ structure has also been observed previously in InSb nanowires[22,24,26] and in other group III-V compounds (for example, InP), where its formation is attributed to the growth kinetics (supersaturation in the catalyst and/or the temperature).[46–48] In case of Au-catalyzed growth of InP nanowires, recent surface X-ray diffraction studies suggest that the WZ phase may form as a result of an ordered In-rich liquid alloy layer present at the wire/catalyst interface.[49] In case of InSb nanowires, previous studies

indicate that the crystallinity depended on the growth temperature;[23] Mandl *et al.*[22] found that during the self-catalyzed growth of InSb nanowires, the crystal structure (ZB, WZ, and 4H) of varied with the Sb/In ratio at the catalyst-wire interface with higher Sb/In ratios resulting in pure WZ structure. Our results, the observation of WZ-phase InSb and the presence of Sb in the droplets, are consistent with those reported in Ref. [22].

2.5 Conclusion

In summary, we report the influence of precursor flow rates on the compositional evolution of $InP_{1-x}Sb_x$ alloy nanowires grown via self-catalyzed VLS process. We obtain zinc blende structured nanowires for all of the precursor flow rates studied. Interestingly, we observe wurtzite-structured InSb crystalline segments at the catalyst-wire interface. The Sb content in the catalyst droplets and the nanowires, as well as the amount of InSb deposited, increased with increasing Sb precursor flow rate. We attribute this phenomenon to the precipitation of excess Sb from the In-rich In-Sb alloy droplets during rapid cooling. These results suggest that the absolute flow rates of precursors are an important factor, in addition to the growth flux and substrate temperature, controlling the fabrication of multi-component alloy nanowires and related heterostructures with desired composition and crystal structure.

2.6 Acknowledgments

This work was supported by funds from Intel Corporation, Northrop Grumman Space Technology, UCLA COR-FRG, and the NSF through the grant CMMI-0926412. The authors acknowledge the use of instruments at the Electron Imaging Center for NanoMachines supported by NIH (1S10RR23057 to ZHZ) and CNSI at UCLA.

2.7 References

1 E. H. Reihlen, M. J. Jou, Z. M. Fang, and G. B. Stringfellow, *J. Appl. Phys.* **68**, 4604 (1990).

2 G. Nataf and C. Verie, *J. Cryst. Growth.* **55**, 87 (1981).

3 K. S. Boutros, F. G. McIntosh, J.C. Roberts, and S. M. Bedair, *Appl. Phys. Lett.* **67**, 1856 (1995).

4 H. Naoi, Y. Naoi, and S. Sakai, *Solid-State Elec.* **41**, 319 (1997).

5 N. H. Karam, et al. *IEEE Trans. Electron Devices* **46**, 2116 (1999).

6 R. R. King, D. C. Law, K. M. Edmondson, C. M. Fetzer, G. S. Kinsey, H. Yoon, R. A. Sherif, and N. H. Karam, *Appl. Phys. Lett.* **90**, 183516 (2007).

7 R. S. Wagner and W. C. Ellis, *Appl. Phys. Lett.* **4**, 189 (1964).

8 K. A. Dick, *Prog. Cryst. Growth Char. Mater.* **54**, 138 (2008) and references therein.

9 M. E. Reimer, M. P. van Kouwen, M. Barkelid, M. Hocevar, M. H. M. van Weert, R. E. Algra, E. Bakkers, M. T. Bjork, H. Schmid, H. Riel, L. P. Kouwenhoven, and V. Zwiller, *J. Nanophotonics* **5**, 053502 (2011).

10 B. M. Borg, K. A. Dick, J. Eymery, and L. E. Wernersson, *Appl. Phys. Lett.* **98**, 113104 (2011).

11 M. Wolz, V. M. Kaganer, O. Brandt, L. Geelhaar, and H. Riechert, *Appl. Phys. Lett.* **98**, 261907 (2011).

12 R. Agarwal, *Small* **4**, 1872 (2008).

13 C. M. Lieber, *Nano Lett.* **2**, 81 (2002).

14 L. J. Lauhon, M. S. Gudiksen, D. Wang, and C. M. Lieber, *Nature* **420**, 57 (2002).

15 L. Samuelson, C. Thelander, M. T. Björk, M. Borgström, K. Deppert, K. A. Dick, A. E. Hansen, T. Mårtensson, N. Panev, A.I. Persson, W. Seifert, N. Sköld, M. W. Larsson, and L. R. Wallenberg, *Physica E* **25**, 313 (2004).

16 E. D. Minot, F. Kelkensberg, M. van Kouwen, J. A. van Dam, L. P. Kouwenhoven, V. Zwiller, M. T. Borgstrom, O. Wunnicke, M. A. Verheijen, and E. Bakkers, *Nano Lett.* **7**, 367 (2007).

17 S. K. Lim, M. J. Tambe, M. M. Brewster, and S. Gradecak, *Nano Lett.* **8**, 1386 (2008).

18 B. M. Borg, K. A. Dick, B. Ganjipour, M. E. Pistol, L. E. Wernersson, and C. Thelander, *Nano Lett.* **10**, 4080 (2010).

19 M. Heurlin, P. Wickert, S. Fält, M. T. Borgström, K. Deppert, L. Samuelson, and M. H. Magnusson, *Nano Lett.* **11**, 2028 (2011).

20 A. Aardvark, N. J. Mason, and P. J. Walker, *Progress in Crystal Growth and Characterization of Materials* **35**, 207 (1997).

21 A. T. Vogel, J. de Boor, M. Becker, J. V. Wittemann, S. L. Mensah, P. Werner, and V. Schmidt, *Nanotechnology* **22**, 015605 (2011).

22 B. Mandl, K. A. Dick, D. Kriegner, M. Keplinger, G. Bauer, J. Stangl, and K. Deppert, *Nanotechnology* **22**, 145603 (2011).

23 A. T. Vogel, J. de Boor, J. V. Wittemann, S. L. Mensah, P. Werner, and V. Schmidt, *Cryst. Growth Des.* **11**, 1896 (2011).

24 D. Kriegner, C. Panse, B. Mandl, K. A. Dick, M. Keplinger, J. M. Persson, P. Caroff, D. Ercolani, L. Sorba, F. Bechstedt, J. Stangl, and G. Bauer, *Nano Lett.* **11**, 1483 (2011).

25 H. Zhou, M. Pozuelo, R. F. Hicks, and S. Kodambaka, *J. Crystal Growth* **319**, 25 (2011).

26 M. Pozuelo, H. Zhou, S. Lin, S. A. Lipman, M. S. Goorsky, R. F. Hicks, and S. Kodambaka, *J. Crystal Growth* **329**, 6 (2011).

27 M. J. Jou and G. B. Stringfellow, *J. Crystal Growth* **98**, 679 (1989).

28 R. M. Biefeld, K. C. Baucom, S. R. Kurtz, and D. M. Follstaedt, *J. Crystal Growth* **133**, 38 (1993).

29 R. Woo, L. Gao, N. Goel, M. Hudait, K. L. Wang, S. Kodambaka, and R. F. Hicks, *Nano Lett.* **9**, 2207 (2009).

30 W. S. Rasband, ImageJ, U. S. National Institutes of Health, Bethesda, Maryland, USA, http://rsb.info.nih.gov/ij/ (1997–2009).

31 M. Pozuelo, S. V. Prikhodko, R. Grantab, H. Zhou, L. Gao, S. D. Sitzman, V. Gambin, V. B. Shenoy, R. F. Hicks, and S. Kodambaka, *J. Crystal Growth* **312**, 2305 (2010).

32 R. E. Algra, M. A. Verheijen, L. F. Feiner, G. G. W. Immink, R. Theissmann, W. J. P. van Enckevort, E. Vlieg, and E. Bakkers, *Nano Lett.* **10**, 2349 (2010).

33 R. E. Algra, M. A. Verheijen, M. T. Borgstrom, L. F. Feiner, G. Immink, W. J. P. van Enckevort, E. Vlieg, and E. Bakkers, *Nature* **456**, 369 (2008).

34 We have also used EDS to determine the nanowire compositions. However, given that the X-ray energies of In-L and Sb-L lines are nearly the same, accurate determination of Sb content within the wires is difficult.

35 L. Vegard, *Z. Phys.* **5**, 17 (1921).

36 M. J. Jou, Y. T. Cherng, H. R. Jen, and G. B. Stringfellow, *J. Crystal Growth* **93**, 62 (1988).

37 N. Bouarissa, S. Bougouffa, and A. Kamli, *Semicond. Sci. Technol.* **20**, 256 (2005).

38 M. Behet, B. Stoll, and K. Heime, *J. Crystal Growth* **124**, 389 (1992).

39 W. J. Duncan, A. S. M. Ali, E. M. Marsh, and P.C. Spurdens, *J. Crystal Growth* **143**, 155 (1994).

40 P. Gong, ICDD Grant-in-Aid, Polytechnic Institute of New York, Brooklyn, New York, USA (1981).

41 H. E. Swanson, R. K. Fuyat, and G. M. Ugrinic, Standard X-ray Diffraction Powder Patterns, *Natl. Bur. Stand. Circ.* **4**, 539 (1955).

42 These values should be considered as upper estimates since we cannot rule out the influence of elastic strain on the lattice parameters extracted from SAED measurements.

43 C. Ngo et al., unpublished.

44 C. E. T. White and H. Okamoto, "Phase diagrams of indium alloys and their engineering applications" *Indium Corp. of America* Utica, NY (1992).

45 G. B. Stringfellow, Organometallic Vapor-Phase Epitaxy: Theory and Practice, *Academic Press* Ed. 2 (1999).

46 J. Johansson, L. S. Karlsson, C. P. T. Svensson, T. Martensson, B. A. Wacaser, K. Deppert, L. Samuelson, and W. Seifert, *Nature Mater.* **5**, 574 (2006).

47 F. Glas, J. -C. Harmand, and G. Patriarche, *Phys. Rev. Lett.* **99**, 135501 (2007).

48 J. Johansson, L. S. Karlsson, K. A. Dick, J. Bolinsson, B. A. Wacaser, K. Deppert, and L. Samuelson, *Cryst. Growth Design* **9**, 766 (2009).

49 R. E. Algra, V. Vonk, D. Wermeille, W. J. Szweryn, M. A. Verheijen, W. J. P. van Enckevort, A. A. C. Bode, W. L. Noorduin, E. Tancini, A. E. F. de Jong, E. Bakkers, and E. Vlieg, *Nano Lett.* **11**, 44 (2011).

CHAPTER 3 *IN SITU* MICROSCOPY STUDIES OF GALLIUM DROPLET EVAPORATION AND INFLUENCE OF ATMOSPHERIC OXIDATION

3.1 Abstract

Using *in situ* transmission electron microscopy, we investigated the kinetics of liquid Ga droplet decay on thin amorphous silica films during annealing at temperatures up to 750 °C. The microscopy images reveal that the Ga droplets undergo gradual evaporation above ~ 500 °C, with faster overall decay from droplets annealed at higher temperatures. We find that the droplet volumes decrease non-linearly with time and are heavily influenced by the existence of a native solid oxide shell that is formed after the as-deposited droplets are exposed to air. Droplet decay behavior is analyzed relative to the diameter-squared law from traditional droplet evaporation kinetics, and deviations from the expected linear decay are proposed.

3.2 Introduction

One of the most useful applications of gallium is as a catalyst for nanowire growth via the vapor-liquid-solid (VLS) mechanism. Since its conception by Wagner and Ellis using gold "impurities",[1] VLS growth has evolved to utilize other metal catalysts such as gallium and indium. A key component of this system is the liquid droplet catalyst, which directly controls nanowire size, location, structure, morphology, and growth direction.[2,3] Herein, we demonstrate the use of *in situ* transmission electron microscopy (TEM) to provide unique insight into gallium droplet behavior at high temperature, particularly evaporation. Studying the physical properties of gallium droplets by observing the effects of increased temperatures enables one to elucidate the evaporation kinetics, and determine potential parameters for size-controlled materials synthesized using seed-mediated growth techniques.

Liquid metals such as gallium and related alloys have received significant attention due to their unique physical and chemical properties that drive several emerging technologies. For example, several attractive properties include low vapor pressure (7.32×10^{-39} Torr)[4], low melting temperature (T_m = 29.8 °C)[5], and large thermal conductivity (40.6 W/mK)[5], which can be employed in a variety of applications such as hydrogen- and energy-storage materials, coolants in microelectronics[4,7–10] and nuclear reactors,[11,12] and alloying additives, notably for energy applications.[13–20] More recently, nanoscale gallium particles have been shown to have promising material characteristics for the use in mercury-free nanoscale thermometers and electrical switches,[21–24] Li-battery electrodes,[26–28] plasmonics,[28–37] and catalysts for the growth of nanowires[38,39] and graphene.[40–44] Thermochemical stability of liquid-metal/solid interfaces is an important consideration for both nanoscale and bulk applications as it affects properties such as wettability, adhesion, chemical reactivity, and droplet sizes.

One challenge in applying and observing liquid metals is the propensity for a thermally-stable oxide surface layer to form at room temperature upon exposure to oxygen. Atmospheric oxidation is an important factor to consider for the processing of devices, given that a native oxide effects intrinsic material behavior such as surface ordering[45–47] and oxidation,[48–50] ultimately affecting growth. Here, we discuss the effects of gallium's native oxide formation by performing *in situ* annealing of Ga droplets grown via molecular beam epitaxy (MBE). Understanding the change in kinetics between pure gallium and gallium with native oxide shells, in turn, provides a fundamental understanding of gallium properties towards growth mechanisms.

3.3 Materials and Methods

In all of our experiments, ultrapure gallium (7N) droplets were deposited in a GEN 930 MBE chamber (pressure ~ 3×10^{-10} Torr) directly onto 2.3 mm diameter molybdenum TEM grids with an amorphous SiO2 support film. A custom-machined holder was used to secure the grids into the traditional MBE wafer holder without adhesive. The sample holder and the TEM grids were baked at 175 °C inside the MBE buffer chamber. Then, the sample holder with TEM grids were transferred into the primary MBE chamber with the sample holder temperature fixed at 150 °C. The formation of Ga droplets was conducted by opening the Ga-effusion cell shutter. The deposition amount of Ga was equivalent to several tens or hundreds of nanometers of GaAs, depending on the duration of Ga-effusion cell shutter opening; typical deposition rate of Ga was equivalent to 1 ML/s GaAs calibrated on GaAs(001) surface at 580 °C. Following Ga deposition and droplet formation, samples were removed from MBE chamber and stored at room temperature in air.

A Humming Scientific holder was used to heat individual grids *in situ* in either an FEI 300 kV Titan S/TEM or FEI 120 kV Tecnai 12 TEM. Each sample was heated in 50 – 100 K increments to stabilize thermal drift before reaching the targeted temperature, typically holding for 10 min each at 100 °C and 200° C, and 30 min from 300 °C to 600 °C and above. (Figure 3.1 shows a plot of the typical heating profile.) Scanning electron microscopy (SEM) imaging was done via FEI Nova Nano 230. Energy-dispersive spectroscopy (EDS) data was obtained using an FEI Titan3 S/TEM at Linköping University. Images were processed manually via ImageJ. Drift-compensated videos and automated droplet measurements were compiled via Image-Pro Premier,[51] using images taken via Digital Micrograph during *in situ* heating. Numerous videos (and associated diameter or area vs. time plots) of annealing experiments at T = 650 °C – 750 °C are available from the author, several of which are available as supplementary material.

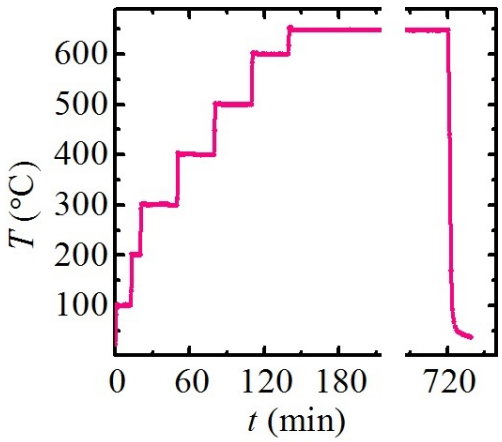

Figure 3.1 Plot of temperature *T* vs. time *t* for the sample annealed at 650 °C, as typical for the heating experiments presented in the paper and described in the Materials and Methods section.

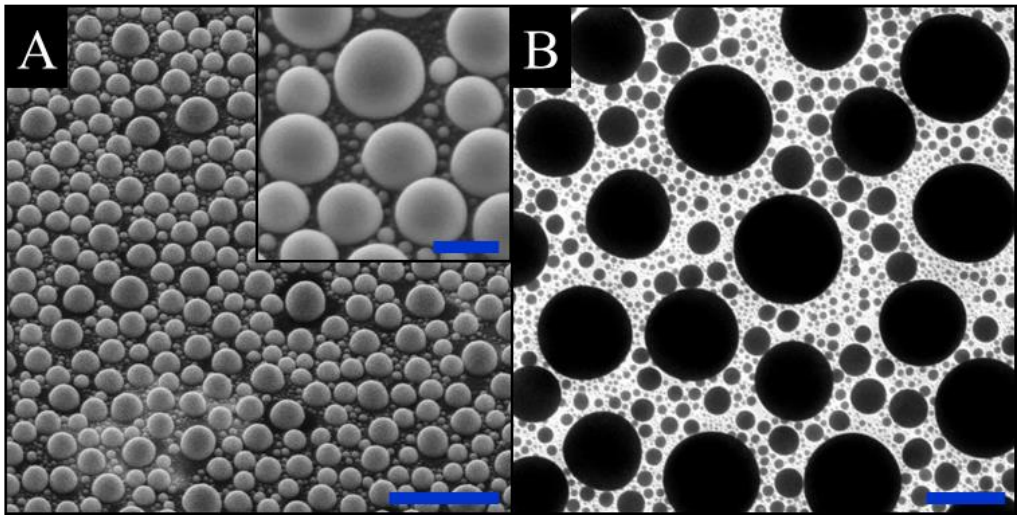

Figure 3.2 (a) SEM images at ~ 40° tilt, and (b) plan-view TEM image of gallium droplets as-deposited by MBE onto the SiO_2 support film of TEM grids. The droplets have approximately hemispherical morphology due to the high surface tension of gallium (708 mJ/m2 at T_m = 29.8 °C[52]). Scale bars = (a) 3 µm with 1 µm inset, (b) 500 nm.

3.4 Results and Discussion

Deposition of Ga from the MBE results in droplets that have approximately hemispherical morphology, as seen from an angle via SEM (~ 40 °); from top view in the TEM they appear as dark circles. (Figure 3.2) The droplets have this hemispherical morphology due to

the high surface tension of gallium (708 mJ/m^2 at T_m = 29.8 °C).[52] We find that annealing Ga droplets at temperatures above ~ 500 °C causes slow disappearance of the material over time, while there is no visible change during annealing at lower temperatures (holding for 10 min – 30 min at each temperature). Figure 3.3A includes a series of plan-view TEM images taken at hourly intervals at T = 650 °C, showing Ga droplets gradually decreasing in size before eventually disappearing. In this and similar experiments while annealing at temperatures up to 800 °C, the Ga droplets evaporate without any translational motion, coalescence, or ripening.

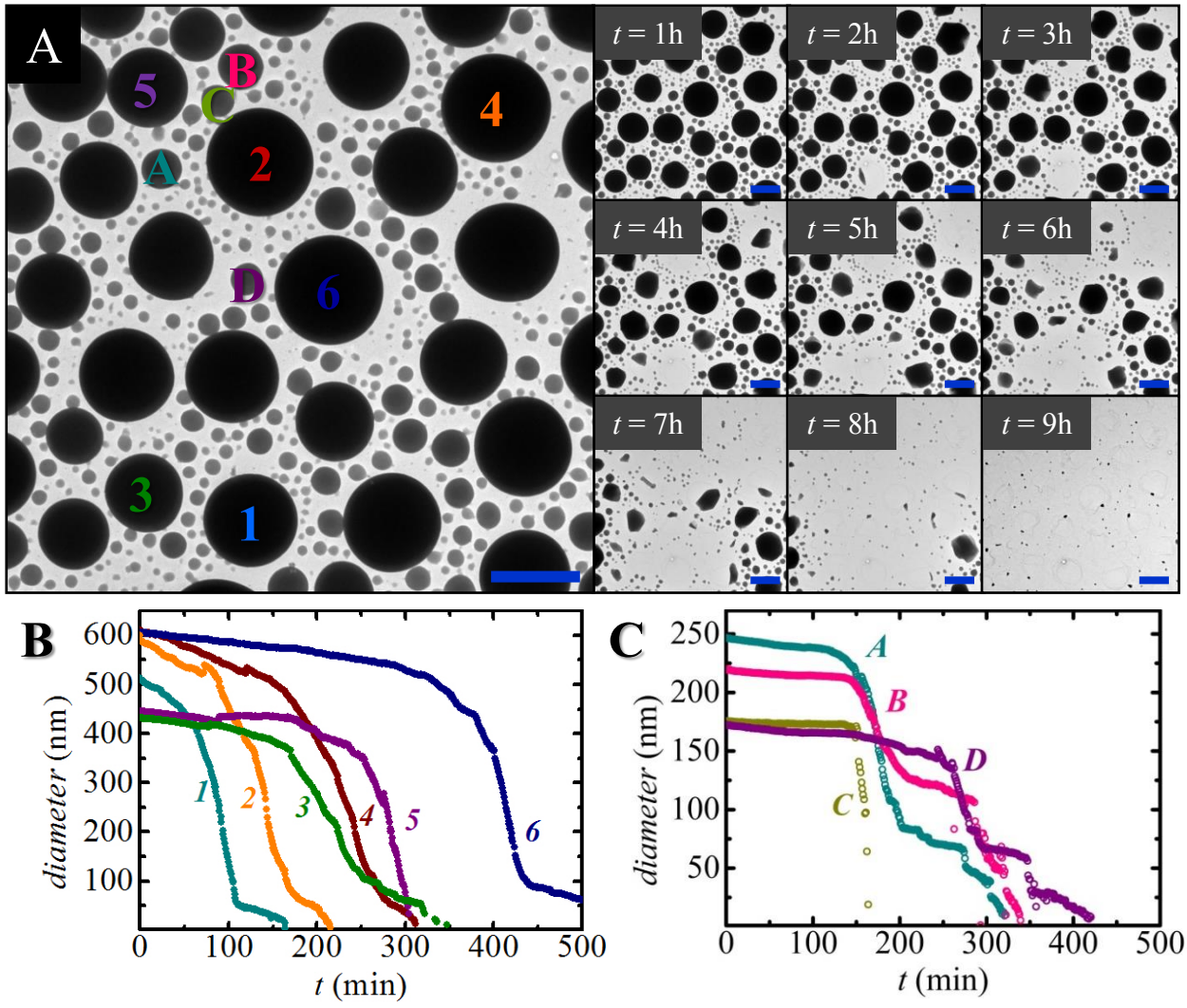

Figure 3.3 Evaporation of Ga droplets annealed at T = 650 °C. (A) On the left, TEM image of a Ga droplet ensemble at t = 0. On the right, TEM images of the same droplets as a function of increasing time during annealing over a period of 9 hours. (B-C) Plots of individual droplet

decay for diameter as a function of time *t*, corresponding to the labeled droplets in (A). Each point is an individual droplet measurement from a TEM image, and TEM images were obtained once a minute. Larger droplets (labeled 1 – 6) with diameters > 400 nm tend towards slow evaporation beginning immediately, followed by an abrupt decrease in size. Smaller droplets (labeled A – D) with diameters < 250 nm remain stable for a much longer time before exhibiting an abrupt decrease and disappearance. Scale bars = 500 nm.

We quantify the evaporation behavior of the droplets by measuring their projected area and average diameter from the top-down TEM images collected over time. Here, strictly speaking, we are measuring the observed or projected area of each droplet and considering it as an estimate of the surface area. Since most droplets are close to hemispherical ($A_{surface} = \pi d^2/2$), as seen in Figure 3.2A, the projected area ($A = \pi d^2/4$) is expected to be a reasonable measurement of the surface area. Plotting the time-dependent behavior of several droplets annealed at 650 °C (Figures 3.3B and C) shows that the decay rates and droplet lifetimes vary with droplet sizes. Contrary to intuition, smaller droplets exhibit negligible changes in size for ~150 minutes (Figures 3.3C and A), whereas the large ones have significant initial decay rates from the very beginning. Occasionally, we observe droplets of very similar diameters that have different evaporation decay, e.g., #2, #4 and #6 in Figure 2.

In these experiments, droplet evolution is studied at three different annealing temperatures: 650 °C, 700 °C and 750 °C. We note that these *T* values represent the temperature regime where droplet behavior is observable over an experimentally controllable time frame. Below *T* = 650 °C droplet decay is extremely slow, potentially days. Above *T* = 750 °C, droplet decay is too rapid to capture with the TEM camera, due to both rapid devolution of the droplets and drift of the sample holder. In Figure 3.4, we observe that at the two higher temperatures, the potential dependence of the decay rate on diameter is less pronounced – to the point that the most particles have roughly the same lifetime. The initial decay rates, strictly speaking, still depend on the diameter but to a much smaller extent than in the 650 °C case; for example, there is no

horizontal plateau for the smaller drops, and all the drops start decaying immediately. For all other annealing experiments of similar droplet ensembles, typically at the beginning of heating there is immediate and gradual decay, followed by precipitous decay near the end of each droplet's lifetime, e.g., behavior in Figures 3.4B and C.

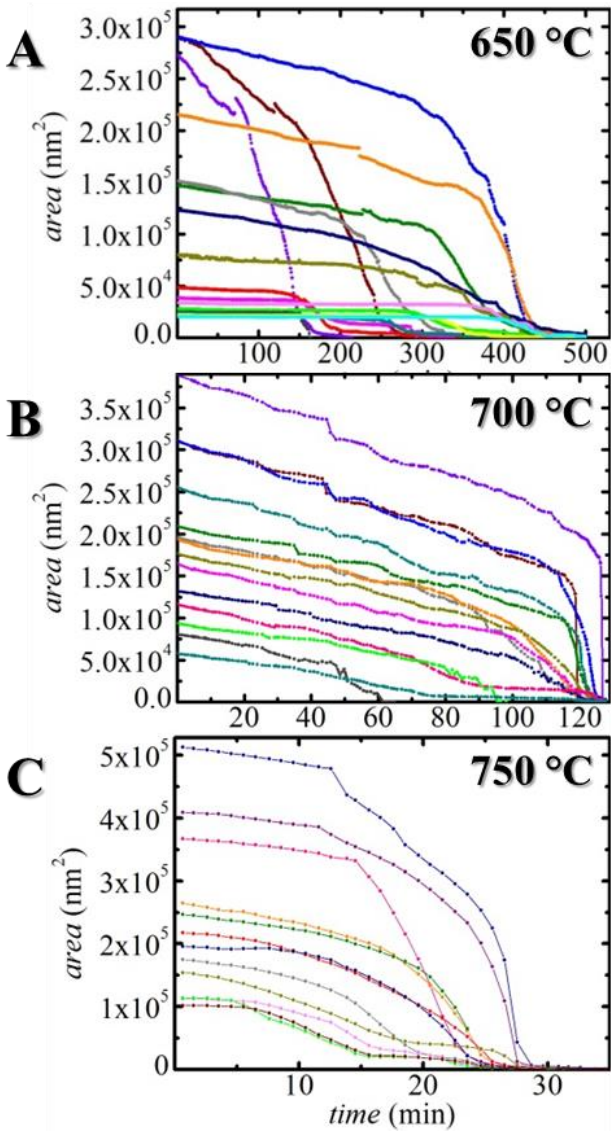

Figure 3.4 Plots of area vs. time for three separate Ga droplet ensembles annealed at T = 650 °C – 750 °C. There is decrease of all droplet size over time for all temperatures, as well as total evaporation time decreasing with increasing temperature. For (A) at T = 650 °C, maximum droplet lifetime is ~ 500 min, (B) at T = 700 °C, maximum droplet lifetime is ~ 120 min, and (C) at T = 750 °C, maximum droplet lifetime is ~ 30 min. Individual droplet areas are obtained by measurements of TEM images taken every minute.

If we consider the simple case of a spherical droplet with constant flux of evaporating atoms from the entire surface, it would be expected that a steady decrease in radius occurs. In this scenario, droplet size would decay linearly with time under the scaling relationship:

$$d = a(t_f - t)^n,$$

where d is droplet diameter, a is a constant based on material parameters, t_f is the droplet lifetime (i.e., time period over which a droplet decays away), and n is a scaling exponent that ~ 1 (for linear decay). Extrapolated scaling values from our data, however, are closer to $n = ½$ – noting that the standard deviation is large and quantified conclusions should be made cautiously. The case of $n = ½$ implies that droplet diameter is decreasing as a constant function of area or d^2, as opposed to constant volume ($n = 1$). While this is surprising for our simple model, results from experimentally determined and computational modeling of droplet decay show that radius or diameter decrease linearly with time. Other factors must therefore be considered for our gallium droplet evaporation.

In the tradition of droplet evaporation literature, analysis is most commonly carried out in what is commonly referred to as the diameter-square law (d^2-law). Under a number of simplifying assumptions (e.g. spherical symmetry, stationary evaporation), the d^2-law description of evaporation predicts an exact linear decay of droplet area with time.[53-55] Interestingly, the mass balance equations at the surface of the droplet and the heat balance equations both yield, separately, a linear decrease of the droplet area under stationary conditions.[53] However, the equations derived from mass balance rely on the diffusion of vapor atoms (Ga atoms reaching the gas phase due to evaporation) though a *host* gaseous phase – typically air, but it is absent in our high vacuum conditions.[53] The heat balance equations, under conditions of stationarity

(partial derivatives with respect to time are zero) lead to the following solution for the time-derivative of the diameter d of the droplet:[53]

$$\dot{d} = \frac{2\lambda\Delta T}{dq_{eff}\rho_L}, \qquad (1)$$

where λ is the coefficient of thermal conductivity of the vapor, ΔT is the temperature difference between the liquid droplet and the vapor far from the interface, q_{eff} is the effective evaporation enthalpy per unit mass, and ρ_L is the density of liquid Ga in the droplet. The reason for labeling the enthalpy per unit mass "effective" is that the enthalpy of evaporation is defined correctly only for thermodynamic equilibrium conditions, which are much stricter than the stationarity imposed here. The temperature of the liquid is assumed to be the annealing temperature, which is reasonable because the liquid drops are good heat conductors. Observed/projected area of a near-spherical droplet is $A = \pi d^2/4$; therefore Equation (1) gives a constant decay rate for the area:

$$\dot{A} = \frac{\pi\lambda\Delta T}{q_{eff}\rho_L}. \qquad (2)$$

Equations (1) and (2) are essentially the statement of the d^2-law, in which the square of the radius decreases linearly with time (dd^2/dt = constant). To correlate this simple analysis with the experiments, we first turn again to Figure 3.4, in which the imaged/projected area is shown as a function of time for different temperatures and different drops at each temperature. With the exception of the smallest diameter plots at T = 650 °C, all other $A = A(t)$ plots in Figure 3.4 show an approximately linear decay for at least 50 minutes in Figures 3.4A and B, and for at least 15 min in Figure 3.4C. The calculated slopes of some of these decays are listed in Table 3.1, along with their standard deviations; the relatively small standard deviations indicate that the linear approximation (the d^2-law) is obeyed reasonably well for the initial portions of the decay. The values of the slopes are equal to the right-hand side of Equation (2).

Table 3.1 Initial slopes associated with decay of selected *A(t)* plots. Droplets are labeled as the corresponding color in Figure 3.4.

T	**Droplet initial diameter and slope**				
650 °C	***Blue***	***Orange***	***Olive***	***Navy***	***Dark yellow***
	605.8 nm	522.0 nm	431.0 nm	394.7 nm	317.2 nm
	-189.24 ± 0.93	-160.95 ± 1.15	-116.99 ± 0.55	-126.58 ± 1.25	-48.01 ± 1.71
700 °C	***Violet***	***Wine***	***Dark cyan***	***Magenta***	***Dark gray***
	701.9 nm	628.5 nm	567.1 nm	454.2 nm	317.4 nm
	-1679.15 ± 38.85	-1284.86 ± 51.73	-1226.2 ± 38.44	-871.2 ± 49.07	-603.75 ± 25.7
750 °C	***Royal***	***Purple***	***Pink***	***Red***	***Gray***
	797.3 nm	717.5 nm	677.9 nm	524.3 nm	470.0 nm
	-2841.81 ± 52.23	-2170.71 ± 109.7	-2028.65 ± 97.5	-3589.4 ± 304.1	-3498.52 ± 210.6

Two main observations emerge from Table 3.1 and Figures 3.4. The first is that at the same temperature, the initial slopes decrease in absolute value with droplet area. There are some deviations from this trend, and those could be due to the fewer data points present at high temperatures (hence the quality of the fits is affected), as well as inhomogeneity of the substrate temperature resulting in some of the droplets being evaporated at different temperatures than the nominal annealing temperature. For example, this is the case with the uppermost two curves in Figure 3.4A: They are both linear (at the beginning of the evaporation) and correspond to the same initial diameter (606.9 and 605.8 nm), but decrease at visibly different rates. We attribute this to slightly different temperatures between droplets that are far from each other, given the relatively poor thermal conductivity of the SiO_2 support film. Also, droplets on the film closer to the metal TEM grid are hotter than those closer to the center of each grid quadrant (Figure 3.5).

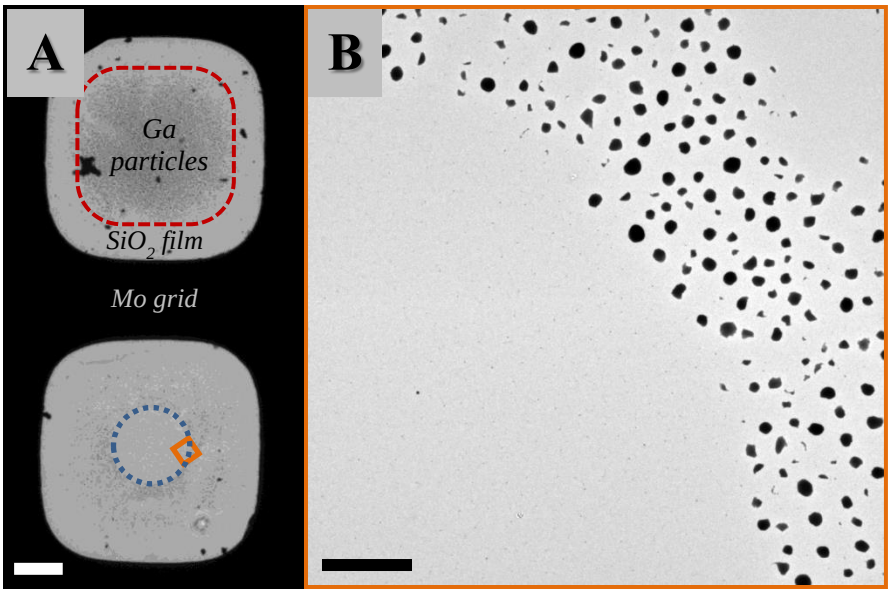

Figure 3.5 (A) Low-magnification TEM image of two quadrants of a grid after heating at 700 °C for 2 hours, where the circular area marked in the lower quadrant (dotted blue circle) shows where the electron beam was held to observe droplet evaporation (specifically Figure 3.4B. In the upper quadrant, the dashed red line marks the approximate boundary to where the sample was at a higher temperature during annealing (aka: where more droplets evaporated) due to proximity to the metal Mo grid. Scale bar = 20 μm. (B) Higher magnification TEM image of the area marked by the orange box in (A), showing the circular area where droplets are gone versus the remaining particles outside the e-beam field of view. Scale bar = 3 μm.

The second observation is that for similar initial diameters, higher temperatures lead to faster decays. While the latter is an intuitive observation (higher temperatures produce faster evaporation rates), the dependence of the evaporation rate dA/dt on the diameter requires further analysis. Turning to the deviations from the d^2-law in the literature, one ubiquitous factor that triggers deviations from Equation (2) is the discontinuity in temperature at the surface of the droplet – discontinuity that occurs and is maintained during steady state evaporation.[56] Other kinetic effects deal with the presence of high gradients at the surface. Almost irrespective of their origin and mechanism by which they affect the evaporation, the deviations from the d^2-law are described by:[53,54]

$$\dot{d} = \frac{P_1}{d + P_2}, \qquad (3)$$

where P_1 takes the form on the right hand side of Equation (1) (without d in the denominator), and P_2 is a coefficient to be fit to experimental data and which ideally embeds all the deviations from the Eq(1). At this stage, we notice for example that the decrease of the initial absolute value of the slope with initial diameter decrease is consistent (at least qualitatively) with Equation (3). Indeed, rewriting (3) in terms of projected area, we have

$$\dot{A}(t) = \frac{2\pi a P_1}{d + P_2} = \frac{2\pi P_1}{1+\frac{P_2}{d}}, \qquad (4)$$

where smaller initial diameter means higher P_2/d, and leads to smaller initial slope of the decay – consistent with the trends identified in Figure 3.4. Equation (3) can be integrated to give the time dependence of the radius d:

$$d = d(t) = -P_2 + \sqrt{(P_2 + d_0)^2 + 2P_1 t}, \qquad (5)$$

where d_0 is the diameter at $t = 0$. Through use of $A = \pi d^2/4$, Equation (5) would be expected to describe the observed area during the evaporative decay of nanoparticles in a unified way for all diameters at a given temperature. However, for 650 °C, variations of the slope with the diameter cannot be quantitatively captured by Equation (5), which gives a very weak diameter dependence of the slope of initial decay. The $A = A(t)$ plots at higher temperatures fare a bit better in relation to Equation (5), but are still not satisfactory. Impurities may qualitatively explain the behavior observed in Figure 3.4, and in particular the deviations from Equation (2). The most likely impurity formed is a Ga oxide layer, as suggested by inspecting the Ga-O phase diagram at low pressures:[57] for low concentrations of oxygen and temperatures below ~ 780 °C, thermodynamics favor a segregated system consisting of liquid Ga and solid β-Ga_2O_3. Indeed, our ultrapure Ga samples were exposed to atmospheric oxygen during inevitable transfer from the MBE system to storage under ambient conditions and then heating in high vacuum

(10^{-7} ~ 10^{-8} Torr). EDS compositional maps of remaining particles after annealing[58] reveal the presence of oxygen around the particles (Figures 3.6B-E). Also, droplets with over a year of exposure to atmosphere change from having smooth, spherical surfaces to angular, edged shells (Figure 3.6A), which indicates a solid phase. During *in situ* annealing, the Ga droplets show random faceting of the edges (Figures 3.6F-K), which only are likely to occur with a solid (oxide) phase.

It has been shown that liquid Ga readily forms a surface oxide ranging from 0.5 – 3 nm in thickness and covering up to ~ 85% of the surface.[28,46,49,59–61] Here, annealing the core-shell-like droplets likely reinforced the thin shell of crystalline gallium oxide around the liquid gallium core. At temperatures above ~ 500 °C, the only stable phase of the oxide, β-Ga_2O_3 ($T_{melting}$ = 1795 °C), can be formed by decomposition of the meta-stable α, γ, δ, and ε oxide phases.[57] Stability of the oxide is consistent with the faceting observed during droplet evaporation (Figures 3.6F-K), which is indicative of a solid phase at high temperature (T > 650 °C in our experiments).

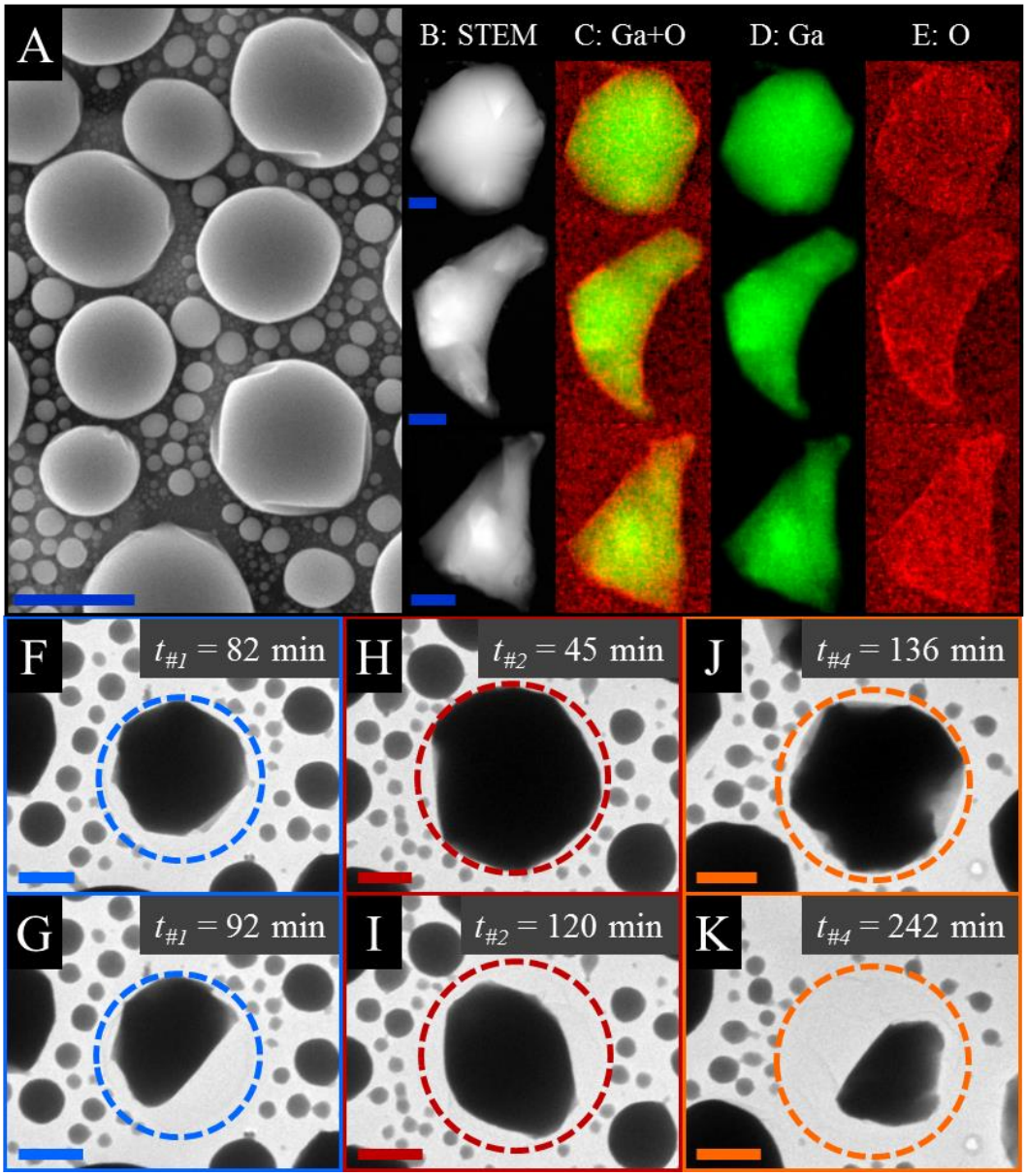

Figure 3.6 (A) SEM image of an oxidized Ga sample after storage under ambient conditions for 14 months, clearly showing surface faceting and ledges on the edges of the larger droplets. The droplets here are from the same ensemble shown in Figure 3.2. Scale bar = 1 µm. (B) Scanning TEM images and (C-E) EDS compositional maps of three partially-evaporated gallium particles remaining after heating and outside the field of view of the previous images, where there was no additional heating from exposure to the electron beam (seen in Figures 3.5B and C). Red and green colors correspond to oxygen and gallium, respectively, and no other elements were detected throughout the sample. The O signal aside from the droplets is attributed to the SiO_2 support film. The particles exhibit faceted morphology and an oxide shell regardless of shape. Scale bars = 100 nm. (F-K) *In situ* TEM images of droplets #1, #2, and #4 from Figure 3.2 during annealing at T = 650 °C for the times indicated, showing random faceting of the edges indicative of a solid oxide phase enclosing the liquid metal. Dotted lines indicate the original droplet size and position. Scale bars = 200 nm.

Annealing of less-oxidized droplets, which are exposed to air for shorter amounts of time, shows individual droplets disappearing within a matter of minutes instead of hours. The sequence of *in situ* images in Figure 3.7 shows evaporation of a "fresh" ensemble of droplets that was heated *in situ* at T = 700 °C within 2 days of deposition, versus the ensembles in Figure 3.4 aged (A) 47 days, (B) 13 days, and (C) 29 days. When all of the available images are viewed in sequence, we observe that individual droplets decay very abruptly, within several minutes, even though the entire ensemble takes approximately 2 hours to fully disappear. The evaporation of these droplets appears to occurs in rapid bursts, instead of the steady, gradual decay observed in the annealing experiments of older droplets. Qualitatively, this shows that less amount of oxide shell – as estimated by time exposed to atmospheric oxygen – results in droplets decaying at a faster rate. For many of the faceted droplets, concurrent dark and light grey contrast (notably after t = 18 min in Figure 3.7) suggests that there is phase separation between liquid Ga (dark) and solid oxide (light) materials. We thus note that although short exposures to atmosphere result in significantly more rapid evaporation, there is nonetheless formation of Ga oxide that exerts strong influence on the droplet/particle decay behavior.

In contrast to the air-exposed MBE-deposted droplets, "oxide-free" Ga droplets can be generated by focused-ion beam (FIB) implantation of Ga^+ during cross-section TEM sample preparation. *In situ* annealing of these samples shows that the relatively pure Ga droplets evaporate rapidly (within minutes for most droplets) at temperatures above 500 °C, as opposed to the slowly evaporating Ga droplets with oxide shell. Discussion of FIB-generated Ga droplets and their dynamics during annealing is the focus Chapter 5 of this dissertation.

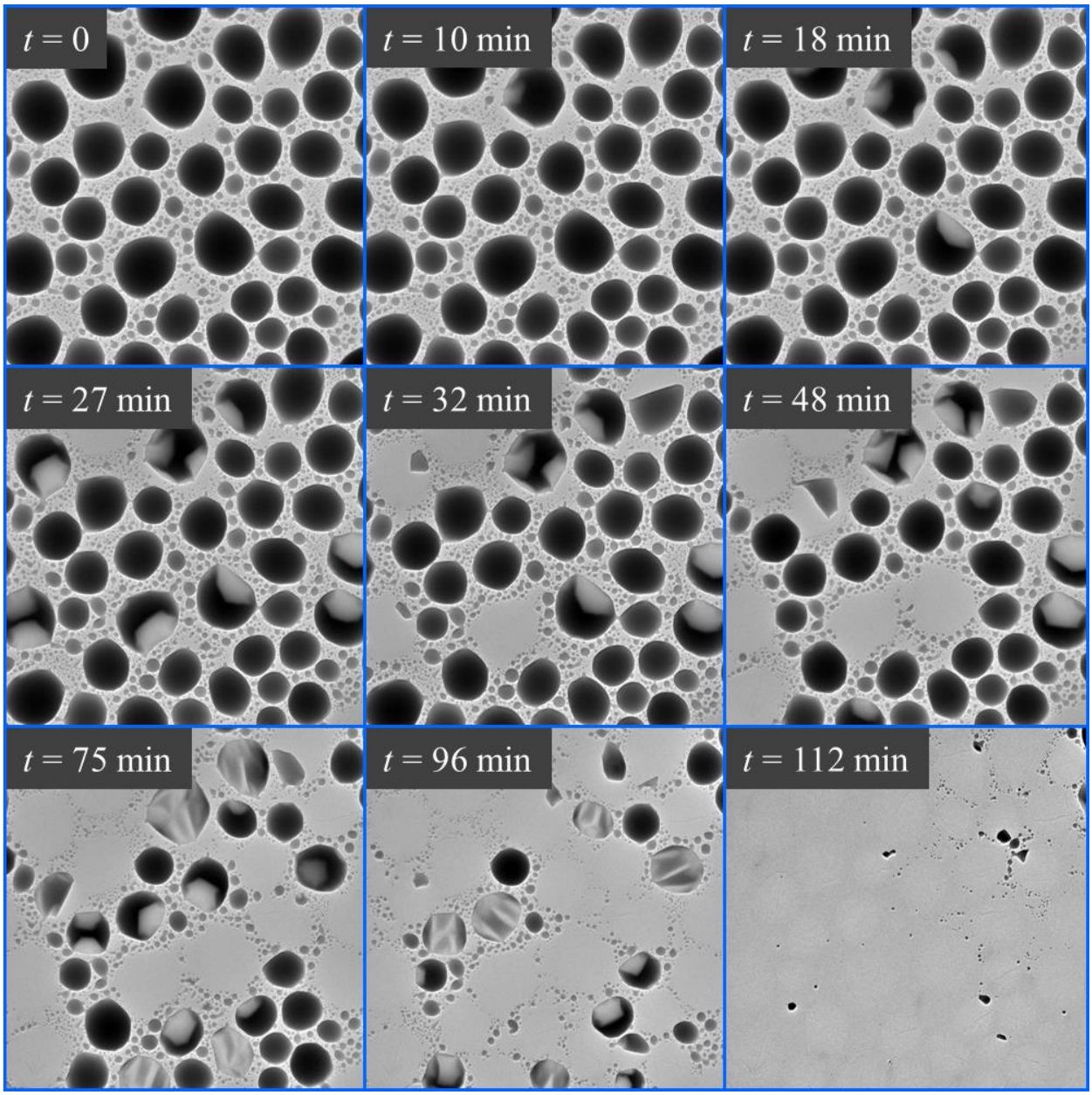

Figure 3.7 *In situ* TEM images of a Ga droplet sample that was stored for approximately one day before heating at T = 700 °C. The full data set for this annealing experiment includes images taken once a minute. Images here were chosen to highlight the different rates of decay exhibited by the droplets, as well as the distinct faceting and potential phase separation of many decaying droplets/particles. Unlike the more oxidized samples that decay gradually at various rates, larger individual droplets here evaporate very rapidly, in minutes instead of hours.

3.5 Conclusion

In summary, we use *in situ* TEM to investigate the evaporation of gallium droplets deposited via MBE onto thin support films. We analyze the droplet behavior by the d^2 law of evaporation and discuss deviations due to the formation of native oxide shell on the surface of the liquid metal, and find that at higher temperatures the decay is both faster and potentially less influenced by oxide shell. Our results give insight into the thermal stability and dynamics of liquid metals with native oxide shell, and show how a small amount of oxide may drastically change the behavior of an otherwise pure material.

3.6 Acknowledgments

This work was supported by funds from the Air Force Office of Scientific Research (FA9550-10-1-0496) and the National Science Foundation (CMMI-1200547). CN thanks Professor Cristian Ciobanu for invaluable discussions on droplet evaporation, Dr. Baolai Liang for providing MBE samples and discussion of droplet growth, and Dr. Justinas Palisaitas for EDS mapping at Linköping University under Professors Lars Hultman and Per Persson. The authors acknowledge the use of instruments at the Electron Imaging Center for NanoMachines supported by NIH (1S10RR23057) and CNSI at UCLA.

3.7 References

1 R.S. Wagner and W.C. Ellis, "Vapor-liquid-solid mechanism of single crystal growth" *Appl. Phys. Lett.* **4**, 89 (1964).

2 M. S. Song, J. H. Jung, Y. Kim, Y. Wang, J. Zou, H. J. Joyce, Q. Gao, H. H. Tan and C. Jagadish, "Vertically standing Ge nanowires on GaAs(1 1 0) substrates" *Nanotechnology* **19**, 125602 (2008).

3 K. A. Dick, K. Deppert, L. Samuelson, L. R. Wallenberg, and F. M. Ross, “Control of GaP and GaAs nanowire morphology through particle and substrate chemical modification” *Nano Lett.* **8**, 4087–91 (2008).

4 V. Y. Prokhorenko, V. V. Roshchupkin, M. A. Pokrasin, S. V. Prokhorenko, and V. V. Kotov, "Liquid Gallium: Potential Uses as a Heat-Transfer Agent" *High Temp.* **38**, 954–968 (2000).

5 W. M. Haynes, ed., CRC handbook of chemistry and physics, CRC press (2013).

6 B. Sakintuna, F. Lamari-Darkrim, and M. Hirscher, "Metal hydride materials for solid hydrogen storage: A review" *Int. J. Hydrogen Energy* **32**, 1121–1140 (2007).

7 H. Ge and J. Liu, "Keeping smartphones cool with gallium phase change material" *J. Heat Transfer* **135**, 054503 (2013).

8 Y. -G. Deng, and J. Liu, "Corrosion development between liquid gallium and four typical metal substrates used in chip cooling device" *Appl. Phys. A* **95**, 907–915 (2009).

9 K. -Q. Ma and J. Liu, "Heat-driven liquid metal cooling device for the thermal management of a computer chip" *J. Phys. D: Appl. Phys.* **40**, 4722 (2007).

10 K. -Q. Ma and J. Liu, "Nano liquid-metal fluid as ultimate coolant" *Phys. Lett. A* **361**, 252–256 (2007).

11 S. D. Park and I. C. Bang, "Feasibility of flooding the reactor cavity with liquid gallium coolant for IVR-ERVC strategy" *Nucl. Engi. Desi.* **258**, 13–18 (2013).

12 T. Sawada, A. Netchaev, H. Ninokata, and H. Endo, "Gallium-cooled liquid metallic-fueled fast reactor" *Prog. Nucl. Energy* **37**, 313–319 (2000).

13 T. Ueno and S. Yamada, "Performance of energy harvester using iron–gallium alloy in free vibration" *Magnetics, IEEE Transactions on* **47**, 2407–2409 (2011).

14 S. Ahmed, K. B. Reuter, Q. Huang, H. Deligianni, L. T. Romankiw, S. Jaime, and P. P. Grand, "Electrodeposited Gallium Alloy Thin Films Synthesized by Solid State Reactions for CIGS Solar Cell" *J. Electrochem. Soc.* **159**, D129–D134 (2011).

15 X. -D. Niu, H. Yamaguchi, X. -J. Ye, and Y. Iwamoto, "Characteristics of a MHD power generator using a low-melting-point Gallium alloy" *Elect. Eng.* **96**, 37–43 (2014).

16 E. Altamirano, J. A. de los Reyes, F. Murrieta, and M. Vrinat, "Hydrodesulfurization of 4, 6–dimethyldibenzothiophene over Co (Ni) MoS 2 catalysts supported on alumina: Effect of gallium as an additive" *Cat. Today* **133**, 292–298 (2008).

17 J. N. D. de León, M. Picquart, M. Villarroel, M. Vrinat, F. J. Gil Llambias, F. Murrieta, and J. A. De Los Reyes. "Effect of gallium as an additive in hydrodesulfurization WS 2/γ-Al 2 O 3 catalysts." *J. Mol. Ca. A: Chemical* **323**, 1–6 (2010).

18 Q. Li and N. J. Bjerrum, "Aluminum as anode for energy storage and conversion: a review" *J. Power Sources* **110**, 1–10 (2002).

19 M. Paramasivam, M. Jayachandran, and S. V. Iyer, "Influence of alloying additives on the performance of commercial grade aluminium as galvanic anode in alkaline zincate solution for use in primary alkaline batteries" *J. App. Electrochem.* **33**, 303–309 (2003).

20 J. V. Naidich and J. N. Chuvashov, "Wettability and contact interaction of gallium-containing melts with non-metallic solids" *J. Mat. Sci.* **18**, 2071–2080 (1983).

21 Y. Gao and Y. Bando, "*Nanotechnology*: Carbon nanothermometer containing gallium" *Nature*, **415** (2002) 599.

22 Z. Liu, Y. Bando, J. Hu, K. Ratinac, and S. P. Ringer, "A novel method for practical temperature measurement with carbon nanotube nanothermometers" *Nanotechnology* **17**, 3681 (2006).

23 Y. B. Li, Y. Bando, D. Golberg, and Z. W. Liu, "Ga-filled single-crystalline MgO nanotube: Wide-temperature range nanothermometer" *App. Phys. Lett.* **83**, 999–1001 (2003).

24 P. S. Dorozhkin, S. V. Tovstonog, D. Golberg, J. Zhan, Y. Ishikawa, M. Shiozawa, H. Nakanishi, K. Nakata, and Y. Bando, "A Liquid-Ga-Filled Carbon Nanotube: A Miniaturized Temperature Sensor and Electrical Switch" *Small* **1**, 1088–1093 (2005).

25 W. Liang, L. Hong, H. Yang, F. Fan, Y. Liu, H. Li, J. Li , J. Y. Huang, L. -Q. Chen, T. Zhu, and S. Zhang, "Nanovoid Formation and Annihilation in Gallium Nanodroplets under Lithiation–Delithiation Cycling" *Nano Lett.* **13**, 5212–5217 (2013).

26 D. Deshpande, J. C. Li, Y. T. Cheng, and M. W. Verbrugge, "Liquid Metal Alloys as Self-Healing Negative Electrodes for Lithium Ion Batteries" *J. Electrochem. Soc.* **158**, A845–A849 (2011).

27 K. T. Lee, Y. S. Jung, T. Kim, C. H. Kim, J. H. Kim, J. Y. Kwon, and S. M. Oh, "Liquid gallium electrode confined in porous carbon matrix as anode for lithium secondary batteries" *Electrochem. Solid-State Lett.* **11**, A21–A24. (2008).

28 M. Yarema, M. Wörle, M. D. Rossell, R. Erni, R. Caputo, L. Protesescu, K. V. Kravchyk, D. N. Dirin, K. Lienau, F. von Rohr, A. Schilling, M. Nachtegaal, and M. V. Kovalenko, "Monodisperse Colloidal Gallium Nanoparticles: Synthesis, Low Temperature Crystallization, Surface Plasmon Resonance and Li-Ion Storage" *J. Am. Chem. Soc.* **136**, 12422–12430 (2014).

29 S. R. C. Vivekchand, C. J. Engel, S. M. Lubin, M. G. Blaber, W. Zhou, J.Y. Suh, G. C. Schatz, and T. W. Odom, "Liquid Plasmonics: Manipulating Surface Plasmon Polaritons via Phase Transitions" *Nano Lett.* **12**, 4324–4328 (2012).

30 C. W. Yi, T. H. Kim, W. Y. Jiao, Y. Yang, A. Lazarides, K. Hingerl, G. Bruno, A. Brown, and M. Losurdo, "Evidence of Plasmonic Coupling in Gallium Nanoparticles/Graphene/SiC" *Small* **8**, 2721–2730 (2012).

31 P. C. Wu, T. -H. Kim, A. S. Brown, M. Losurdo, G. Bruno, and H. O. Everitt, "Real-time plasmon resonance tuning of liquid Ga nanoparticles by *in situ* spectroscopic ellipsometry" *App. Phys. Lett.* **90**, 103119 (2007).

32 P. C. Wu, C. G. Khoury, T. -H. Kim, Y. Yang, M. Losurdo, G. V. Bianco, T. Vo-Dinh, A. S. Brown, and H. O. Everitt, "Demonstration of surface-enhanced Raman scattering by tunable, plasmonic gallium nanoparticles" *J. Am. Chem. Soc.* **131**, 12032–12033 (2009).

33 P. C. Wu, M. Losurdo, T. -H. Kim, M. Giangregorio, G. Bruno, H. O. Everitt, and A. S. Brown, "Plasmonic gallium nanoparticles on polar semiconductors: interplay between nanoparticle wetting, localized surface plasmon dynamics, and interface charge" *Langmuir* **25**, 924–930 (2008).

34 Y. Yang, J. M. Callahan, T. -H. Kim, A. S. Brown, and H. O. Everitt, "Ultraviolet nanoplasmonics: A demonstration of surface-enhanced Raman spectroscopy, fluorescence, and photodegradation using gallium nanoparticles" *Nano Lett.* **13**, 2837–2841 (2013).

35 M. W. Knight, T. Coenen, Y. Yang, B. J. M. Brenny, M. Losurdo, A. S. Brown, H. O. Everitt, and A. Polman, "Gallium Plasmonics: Deep Subwavelength Spectroscopic Imaging of Single and Interacting Gallium Nanoparticles" *ACS Nano* **9**, 2049–2060 (2015).

36 M. Losurdo, C. Yi, A. Suvorova, S. Rubanov, T.-H. Kim, M. M. Giangregorio, W. Jiao, I. Bergmair, G. Bruno, and A. S. Brown, "Demonstrating the Capability of the High-Performance Plasmonic Gallium–Graphene Couple" *ACS Nano* **8**, 3031–3041 (2014).

37 P. Albella, B. Garcia-Cueto, F. González, F. Moreno, P. C. Wu, T.-H. Kim, A. Brown, Y. Yang, H. O. Everitt, and G. Videen, "Shape matters: plasmonic nanoparticle shape enhances interaction with dielectric substrate" *Nano Lett.* **11**, 3531–3537 (2011).

38 I. Zardo, L. Yu, S. Conesa-Boj, S. Estradé, P. J. Alet, J. Rössler, M. Frimmer, P. R. I Cabarrocas, F. Peiró, J. Arbiol, J. R. Morante, and A. F. I Morral, "Gallium assisted plasma enhanced chemical vapor deposition of silicon nanowires" *Nanotech.* **20**, 155602 (2009).

39 Z. W. Pan, Z. R. Dai, C. Ma, and Z. L. Wang, "Molten Gallium as a Catalyst for the Large-Scale Growth of Highly Aligned Silica Nanowires" *J. Am. Chem. Soc.* **124**, 1817–1822 (2002).

40 G. Ding, Y. Zhu, S. Wang, Q. Gong, L. Sun, T. Wu, X. Xie, and M. Jiang, "Chemical vapor deposition of graphene on liquid metal catalysts" *Carbon* **53**, 321–326 (2013).

41 J. Fujita, R. Ueki, Y. Miyazawa, and T. Ichihashi, "Graphitization at interface between amorphous carbon and liquid gallium for fabricating large area graphene sheets" *J. Vac. Sci. Technol. B* **27**, 3063–3066 (2009).

42 H. Hiura, M. V. Lee, A. V. Tyurnina, and K. Tsukagoshi, "Liquid phase growth of graphene on silicon carbide" *Carbon* **50**, 5076–5084 (2012).

43 J. -I Fujita, Y. Miyazawa, R. Ueki, M. Sasaki, and T. Saito, "Fabrication of Large-Area Graphene Using Liquid Gallium and Its Electrical Properties" *Jap. J. App. Phys.* **49**, 06GC01 (2010).

44 T. Hatakeyama, R. Kometani, S. Warisawa, and S. Ishihara, "Selective graphene growth from DLC thin film patterned by focused-ion-beam chemical vapor deposition" *J. Vac. Sci. Tech. B* **29**, 06FG04 (2011).

45 M. J. Regan, E. H. Kawamoto, S. Lee, P. S. Pershan, N. Maskil, M. Deutsch, and L. E. Berman, "Surface layering in liquid gallium: An X-ray reflectivity study" *Phys. Rev. Lett.* **75**, 2498–2501 (1995).

46 H. Tostmann, E. DiMasi, B.M. Ocko, M. Deutsch, and P.S. Pershan, "X-ray studies of liquid metal surfaces" *J. Non-Cryst. Sol.* **250**, 182–190 (1999).

47 J. Penfold, "The structure of the surface of pure liquids" *Rep. Prof. Phys.* **64**, 777–814 (2001).

48 M. R. Khan, C. B. Eaker, E. F. Bowden, and M. D. Dickey, "Giant and switchable surface activity of liquid metal via surface oxidation" *Proc. Nat. Ac. Sci.* **111**, 14047–14051 (2014).

49 M. J. Regan, H. Tostmann, P. S. Pershan, O. M. Magnussen, E. DiMasi, B. M. Ocko, and M. Deutsch, "X-ray study of the oxidation of liquid-gallium surfaces" *Phys. Rev. B* **55**, 10786 (1997).

50 A. Grigoriev, O. Shpyrko, C. Steimer, P. S. Pershan, B. M. Ocko, M. Deutsch, B. Lin, M. Meron, T. Graber, and J. Gebhardt, "Surface oxidation of liquid Sn" *Surf. Sci.* **575**, 223–232 (2005).

51 Image-Pro Premier 9.1 is a product of Media Cybernetics, Inc.

52 S.C. Hardy, "The surface tension of liquid gallium" *J. Cryst. Growth* **71**, 602–606 (1985).

53 C. K. Law, "Recent advances in droplet vaporization and combustion" *Progress in Energy and Combustion Science* **8**, 171–201 10 (1982).

54 D. Jakubczyk, M. Kolwas, G. Derkachov, K. Kolwas and M. Zientara, "Evaporation of Micro-Droplets: the "Radius-Square-Law" Revisited" *Acta Physica Polonica A* **122**, 709–716 (2012).

55 R. Holyst, M. Litniewski, D. Jakubczyk, K. Kolwas, M. Kolwas, K. Kowalski, S. Migacz, S. Palesa, and M. Zientara, "Evaporation of freely suspended single droplets: experimental, theoretical and computational simulations" *Rep. Prog. Phys.* **76**, 034601 (2013).

56 G. Fang and C. A. Ward, "Temperature measured close to the interface of an evaporating liquid" *Phys. Rev. E* **59**, 417–428 (1999).

57 M. Zinkevich and F. Aldinger, "Thermodynamic Assessment of the Gallium-Oxygen System" *J. Am. Cer. Soc.* **87**, 683–691 (2004).

58 Droplets observed in the TEM are expected to be at a higher temperature than the surrounding area due to heating effect of the electron beam, particularly after hours of continuous exposure. Also, droplets near the edge of each quadrant of the TEM grid are also at a higher temperature due to the Mo metal being hotter than the thin support film. Figure 3.4 shows a low magnification area of the grid after heating, with partially evaporated particles remaining between the TEM field of view (the circular area near the center) and the hotter edges near the grid. Thus, while the observed droplets evaporate away as shown in the plots, gallium particles outside the field of view remain for *ex situ* analysis.

59 G. Schön, "Auger and direct electron spectra in X-ray photoelectron studies of zinc, zinc oxide, gallium and gallium oxide" *J. Electron Spectroscopy and Related Phenomena* **2**, 75–86 (1973).

60 A. Plech, U. Klemradt, H. Metzger, and J. Peisl, "*In situ* x-ray reflectivity study of the oxidation kinetics of liquid gallium and the liquid alloy" *J. Physics: Condensed Matter* **10**, 971 (1998).

61 H. Men and Z. Fan, "Transition of amorphous to crystalline oxide film in initial oxide overgrowth on liquid metals" *Mat. Sci. Tech.* **27**, 1033 (2011).

CHAPTER 4 KINETICS OF GA DROPLET DECAY ON THIN CARBON FILMS

A paper published in Applied Physics Letters, reproduced by license agreement 3623100232837 with the American Institute of Physics Publishing. DOI: 10.1063/1.4802758 (article) *Appl. Physics Lett.* **2012**, *28*, 161601–16160

S. Kodambaka, C. Ngo, J. Palisaitis, P.H. Mayrhofer, L. Hultman and P.O.Å. Persson

4.1 Abstract

Using *in situ* transmission electron microscopy (TEM), we investigated the kinetics of liquid Ga droplet decay on thin amorphous carbon films during annealing at 773 K. The TEM images reveal that liquid Ga forms spherical droplets that undergo coarsening/decay with increasing time. We find that the droplet volumes change non-linearly with time and the volume decay rates depend on their local environment. By comparing the late-stage decay behavior of the droplets with the classical mean-field theory model for Ostwald ripening, we determine that the decay of Ga droplets occurs in the surface-diffusion-limited regime.

4.2 Introduction

The phenomenon of Ostwald ripening refers to coarsening of large clusters at the expense of decaying smaller clusters as a means to minimize the total surface free energy. The cluster coarsening and decay process is governed by the Gibbs-Thomson relation, according to which the equilibrium vapor pressure associated with a cluster increases exponentially with its curvature. The essential steps involved during coarsening and decay of clusters are: 1) attachment/detachment (also referred to as evaporation/condensation) of atoms at the cluster edges and 2) diffusion of atoms between the clusters. Classical mean-field theory models of

Ostwald ripening, first developed by Lifshitz and Slyozov and later extended by others,[1,2] have been useful in the identification of the mass-transport mechanisms controlling the experimentally observed ripening of liquid droplets, as well as solid clusters on surfaces.[3,4] For example, time-dependent changes in the radius *r(t)* of a three-dimensional (3D) cluster are predicted to follow simple relationships of the form $r \propto t^n$, with the scaling exponents $n = 1/3$ and 1/4 corresponding to attachment/detachment- and diffusion- limited kinetics, respectively. A similar approach was later extended to analyze decay rates of individual 2D islands on surfaces, from which rate-limiting steps and associated energetics controlling Ostwald ripening have been determined.[5–8] While there is considerable literature on the kinetics of Ostwald ripening of a variety of solids (elemental metals,[7] semiconductors,[6] and refractory compounds[9,10]), relatively fewer studies exist on the kinetics of coarsening and decay of liquid metals.[3]

Liquid metals such as gallium and related alloys are attractive for applications in high-temperature thermometry, in mirrors, as dental fillings, as coolants in microelectronics and nuclear reactors and as alloying additives in metallurgy owing to a low vapor pressure, excellent wettability as well as good thermal and electrical conductivities.[11] More recently, liquid metals have been found to be promising for applications in plasmonics,[12,13] as electrodes in batteries,[14] as ultra-stretchable conductive wires,[15] and as catalysts for the growth of nanowires[16,17] and graphene.[18,19] For any of these applications, thermochemical stability of liquid-metal/solid interfaces is important since it affects properties such as wettability, adhesion, chemical reactivity, reflectivity, thermal and electrical conductivities, optoelectronic properties, and the size of the liquid droplets. Here, we focus on understanding the thermal stability of liquid-gallium/amorphous-carbon interfaces. While carbon is expected to be insoluble in liquid gallium,

previous studies have suggested otherwise and due to the large difference in the surface energies, liquid gallium does not wet amorphous carbon and forms droplets exceeding 120 °.[18, 20–22]

In this chapter, we present *in situ* transmission electron microscopy (TEM) studies of the decay behavior of Ga droplets on amorphous carbon thin films during annealing. From the time-lapsed TEM images, we find that smaller droplets shrink and the volume decay rates are found to depend on the local environment, characteristic of surface-diffusion-limited Ostwald ripening. We confirm this behavior by comparing the late-stage decay behavior of the droplets with classical mean-field theory model for Ostwald ripening.

4.3 Materials and Methods

All of our experiments were carried out on amorphous carbon thin films deposited using Ga^+ ions in a FEI Nova 600 Nanolab DualBeam focused-ion-beam (FIB) system equipped with a scanning electron microscope and facilities for electron- and ion- beam induced deposition of Pt, W, and C. Previous studies have shown that FIB deposition of thin films using Ga^+ ions leads to implantation of Ga, which upon heating forms liquid droplets on the surfaces of the deposited layers.[20,23–27] In this report, we employ a similar approach to prepare Ga droplets on amorphous carbon thin films using the procedure described below.

We used ZrB_2/Al_2O_3 (0001) thin film samples as the substrate and prepared electron-transparent cross-sectional TEM (XTEM) samples via FIB milling using 30 kV Ga^+ ions. Prior to milling, the ZrB_2/Al_2O_3 (0001) thin film surface was protected by a 1.5 μm thick layer of carbon, deposited initially using 5 kV and 6.3 nA electron beams and afterwards using 30 kV and 0.3 nA ion beams. The FIB-milled samples were attached to the TEM grid by depositing Pt via FIB. Final thinning to electron transparency was carried out by 10 kV ion beams. Fig. 3.1a is a

representative bright-field TEM image of the as-prepared sample. In the image, the darker contrast layer is the ZrB_2 film supported by Al_2O_3 (0001) at the bottom and covered by an amorphous carbon layer. In this projection view, an ~250 nm thick carbon layer is visible on the top surface of the sample. Upon heating, we observe multiple, nearly spherical liquid droplets along the edges of the carbon film, as shown in Fig. 3.1b. Energy-dispersive spectroscopy (EDS) measurements acquired from the XTEM sample, both before and after annealing, indicate that a significant amount of Ga was present within the carbon film prior to heating and in the droplets observed post-annealing after air-exposure. EDS data also indicated a significant fraction of oxygen but this is likely due to air exposure and not expected in the droplets since gallium oxide does not melt at 773 K. The presence of carbon, if any,[18, 20–22] within the droplets could not be determined accurately from EDS due to the large background signal of carbon from the surrounding carbon film. This procedure of forming Ga droplets is highly reproducible and we have obtained similar results, i.e. Ga droplets on carbon films on XTEM samples of C/Ti/Si, Zr/ Al_2O_3 (0001), and bare Al_2O_3 (0001) substrates. The size and areal coverage of these Ga droplets, however, vary with the heating rate and the substrate temperature.

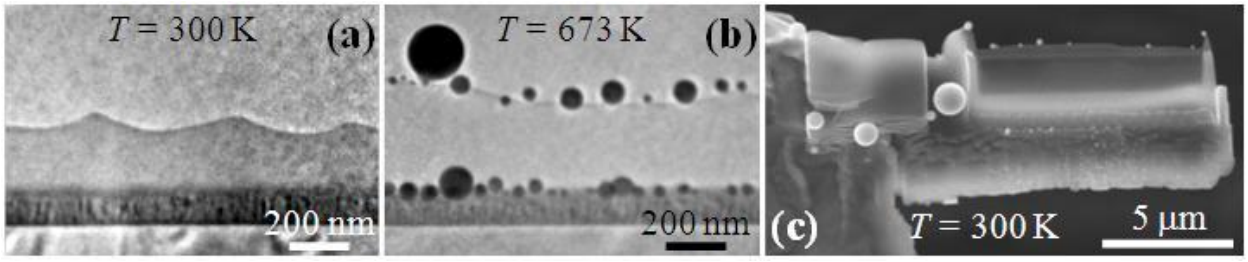

Figure 4.1 (a) Representative bright-field cross-sectional transmission electron microscopy (XTEM) image acquired at room temperature from ZrB_2/Al_2O_3 (0001) interface prepared via focused ion beam milling (FIB). (b) XTEM image of the same sample acquired during annealing at T = 673 K. In the images, the Al_2O_3 (0001) substrate is at the bottom. The upper layers with dark and light grey contrast are ZrB_2 and amorphous carbon, respectively. In Fig. 3.1b, liquid Ga droplets appear as nearly spherical objects on top of the carbon film. (c) Scanning electron microscopy image acquired from another FIB-cut ZrB_2/Al_2O_3 (0001) thin film sample after annealing. In this experiment, the sample was gradually heated to T = 773 K over a period of 23 minutes and held at that T for an additional 15 minutes before cooling to room temperature. The brighter contrast spherical objects are Ga droplets that appear all over the sample with large droplets predominantly located on the sides of the sample and several smaller droplets on the thicker, back end of the sample.

In situ annealing experiments were carried out using a Gatan double-tilt heating holder in a 200 kV, LaB_6, Philips CM20ST TEM (base pressure ~ 10^{-7} Torr). The sample was air-transferred into the TEM and held at ambient temperature until the base pressure recovered. Then, the sample was heated to 773 K in intervals of 100 K and holding at each temperature for approximately 20 min. TEM images were acquired in bright-field mode at regular intervals (~ 20–60 s). Image magnification and acquisition times were varied to check for the influence of electron beam irradiation on the droplet dynamics. We do not observe any such effects on the results presented here. The droplet radii were determined from the TEM images using the ImageJ image processing software.

4.4 Results and Discussion

Figure 4.2 shows a series of TEM images acquired as a function of time t during annealing the sample at 773 K. The near-spherical morphology of the droplets and the minimal

contact with the surface (see Figs. 3.1b and 3.2) suggest that Ga does not wet C. This is plausible since molten Ga has significantly higher surface energy ($\gamma \approx 4$ eV/nm^2 at 773 K)[28,29] than that for amorphous carbon ($\gamma \approx 0.25$ eV/nm^2).[30] We find that, as time progresses, most of the droplets decrease in size and eventually disappear. In contrast, the large droplet labeled *A* and several other large droplets outside of the field of view, which are typically found at the ends of the sample (see Fig. 3.1c), coarsen and remain on the surface. In contrast with previous *in situ* TEM observations, we do not observe graphitic shell formation around the droplets.[18,20,21,23] We do, however, observe small remnants that do not change in size after the bulk of the droplets dissolve. While the images lack sufficient resolution to identify these features, presumably they are graphitic shells as has been reported in the literature.

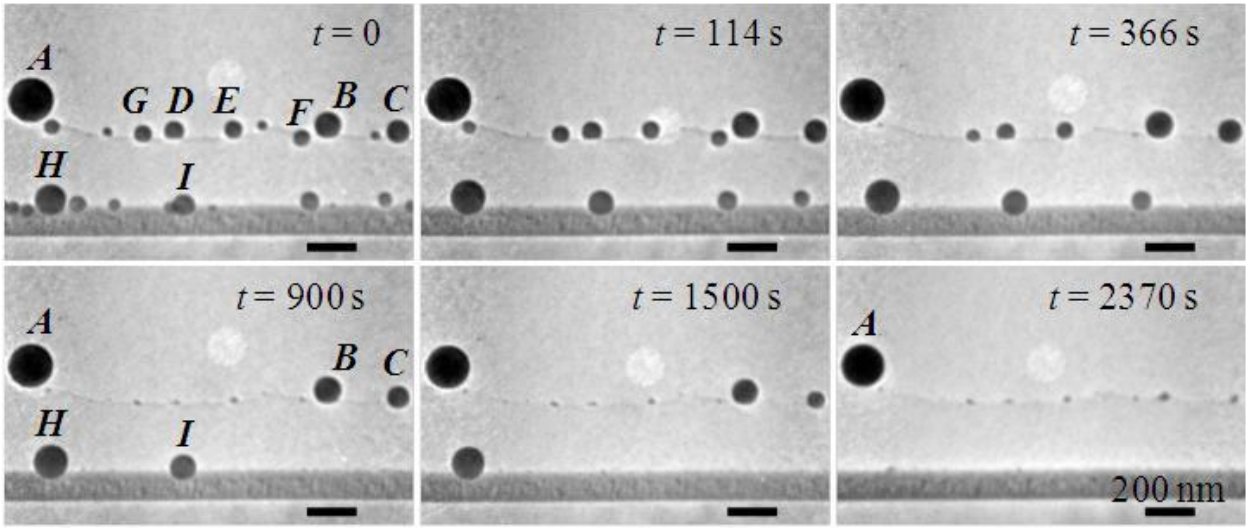

Figure 4.2 Typical bright-field XTEM images acquired from the sample shown in Fig. 3.1 as a function of time *t* during annealing at T = 773 K. The lighter grey contrast circular feature visible near the center of all the images is an artefact of the camera

We now focus on the droplet decay behavior. In the case of material evaporation from the surface into vacuum and/or diffusion into the carbon layer, sizes of all of the droplets should decrease with time. Clearly, not all droplets decay in our experiments. Moreover, the vapor pressure of Ga at 773 K is $< 10^{-9}$ Torr,[31] and the solubility of Ga in carbon is negligible. Hence,

we rule out both of these processes (evaporation and bulk diffusion) as contributing factors to the observed droplet decay. Instead, we suggest (and justify below) that the observed disappearance of droplets is a consequence of Ostwald ripening.[1,3]

In order to validate our hypothesis, we measured time-dependent changes in droplet sizes. Figure 4.3a shows plots of *r* vs. *t* data for the 9 droplets labeled *A*-*I* in Fig. 3.2. We find that, droplets *B*-*I* exhibit decay while the size of droplet *A* remains nearly constant at all *t*. In case the observed decay of Ga droplets is due to diffusion of Ga into the bulk of the sample or evaporation into vacuum, all of the droplets would decrease in size.[32–35] Moreover, the rates of changes in droplet size are not the same for all the droplets. For example, the sizes of smaller droplets *F* and *G* decrease continuously, while the sizes of larger droplets *B* and *C* change little initially and decrease at later times. The observed variations in decay rates are similar to those reported for Ostwald ripening of 2D islands on surfaces and are attributed to local variations in adatom concentrations (equivalent to 2D vapor pressure) around the islands.[6,7,10]

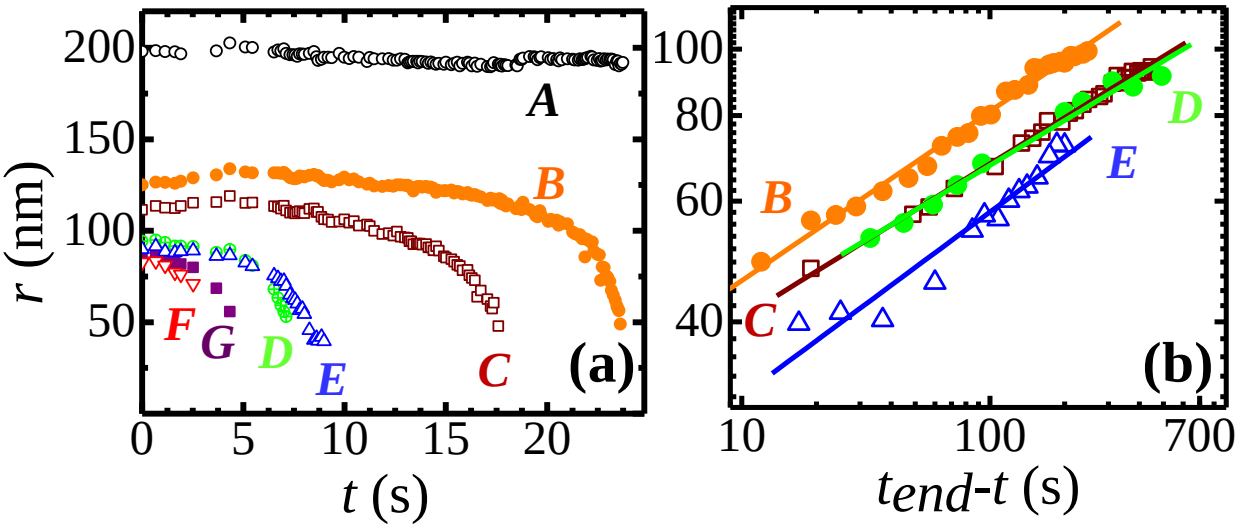

Figure 4.3 (a) Droplet radii (*r*) plotted as a function of annealing time *t*. The labels *A*-*I* correspond to the droplets in Fig. 3.2. (b) Log-log plots of *r* vs. (t_{end}-*t*) for droplets *B*-*E*. t_{end} is defined as the time at which the droplet has completely disappeared. The solid lines are linear least-squares fits to the data whose slopes yield the scaling exponents *n* (see text for details).

In order to compare our experimental observations with the scaling relations of the form $r \propto t^n$ predicted by classical mean-field theory models, we focus on the late-stage decay behavior of the droplets. This is because the scaling relations are derived under two key assumptions: (i) the surface adatom concentration C_s is uniform and equal to C_∞, the equilibrium concentration associated with a planar surface ($r = \infty$) and (ii) the adatom concentration C_r associated with a droplet of radius r is given by the linear expansion of the Gibbs-Thomson relation as $C_r \approx C_\infty(1+2\gamma\Omega/r\mathrm{k_B}T)$, where Ω is the atomic volume of Ga in liquid phase. While C_s will always be higher than C_∞ for non-zero coverage of droplets on the surface, the droplet decay rate, which is proportional to (C_r-C_s), ≈ (C_r-C_∞) for low coverages and small droplets. Fig. 3.3b shows representative log-log plots of r vs. (t_{end}-t) data of droplets *B*-*E*. In the plots, only the late stages of decay are shown and t_{end} is the time determined from the TEM images, accurate to within 5 s, at which the droplet has completely disappeared. From the linear least-squares fits to the data, we obtain n values of 0.25 ± 0.01, 0.22 ± 0.01, 0.22 ± 0.01, and 0.27 ± 0.02 for *B*, *C*, *D*, and *E*, respectively. This value is closer to the mean-field theory predicted value of n = 1/4 for coarsening/decay in the diffusion-limited regime rather than the value of n = 1/3 expected for attachment-limited decay kinetics. We note that exponents smaller than the predicted values can be observed because the scaling relations are derived based upon mean-field theory approximations.[5,7,10] Most significant deviations from the predicted values arise when the condition $C_r \approx C_\infty(1+2\gamma\Omega/r\mathrm{k_B}T)$ is not satisfied, i.e. when the droplets are small such that $2\gamma\Omega/r\mathrm{k_B}T \gg 0$. Using $\Omega \approx 0.02$ nm^3 and $\gamma \approx 4$ eV/nm^2 for molten Ga at T = 773 K,[28,29] we find that the linear expansion is accurate to within 1% for droplet sizes $r \geq 20$ nm. In our experiments, all of the droplets are larger than 20 nm (see Fig. 3.3b) and hence the mean-field theory

predictions apply. Therefore, we suggest that the observed decay of Ga droplets occurs in the surface diffusion limited regime.

4.5 Conclusion

In summary, we investigated the decay behavior of liquid gallium droplets on top of amorphous carbon layers using *in situ* transmission electron microscopy. We find that the droplets undergo Ostwald ripening via diffusion of adatoms along the carbon thin film surface. Our results, which help understand the factors controlling the thermal stability of Ga droplets on carbon surfaces, may be useful in the fabrication of size-controlled Ga droplets for plasmonics and other applications.

4.6 Acknowledgments

We gratefully acknowledge support from the AFOSR (Dr. Ali Sayir) FA9550–10–1–0496 and STINT, the Swedish Foundation for International Cooperation in Research and Higher Education. P.O.Å. Persson gratefully acknowledges support from The Swedish Research Council. P.H. Mayrhofer gratefully acknowledges support from the Austrian Science Fund FWF, START project Y371. We thank Mr. Noah Bodzin and the Nanoelectronics Research Facility in the UCLA Henry Samueli School of Engineering for assistance with focused ion beam milling

4.7 References

1 I. M. Lifshitz and V. V. Slyozov, *J. Phys. Chem. Solids* **19**, 35–50 (1961).

2 P. Wynblatt and N. Gjostein, *Acta Metallurgica* **24**, 1165–1174 (1976).

3 M. Zinke-Allmang, L. C. Feldman, and M. H. Grabow, *Surf. Sci. Rep.* **16**, 377–463 (1992).

4 J. Viñals and W. Mullins, *J. Appl. Phys.* **83**, 621–628 (1998).

5 K. Morgenstern, G. Rosenfeld, and G. Comsa, *Phys. Rev. Lett.* **76**, 2113–2116 (1996).

6 N. Bartelt, W. Theis, and R. Tromp, *Phy. Rev. B* **54**, 11741 (1996).

7 M. Giesen, *Prog. Surf. Sci.* **68**, 1–154 (2001).

8 S. Kodambaka, S. V. Khare, I. Petrov, and J. E. Greene, *Surf. Sci. Rep.* **60**, 55–77 (2006).

9 S. Kodambaka, V. Petrova, S. V. Khare, D. Gall, A. Rockett, I. Petrov, and J. E. Greene, *Phys. Rev. Lett.* **89**, 176102 (2002).

10 S. Kodambaka, V. Petrova, A. Vailionis, I. Petrov, and J. E. Greene, *Surf. Sci.* **526**, 85–96 (2003).

11 V. Y. Prokhorenko, V. V. Roshchupkin, M. A. Pokrasin, S. V. Prokhorenko, and V. V. Kotov, *High temp.* **38**, 954–968 (2000).

12 S. R. C. Vivekchand, C. J. Engel, S. M. Lubin, M. G. Blaber, W. Zhou, J. Y. Suh, G. C. Schatz, and T. W. Odom, *Nano Lett.* **12**, 4324–4328 (2012).

13 C. W. Yi, T. H. Kim, W. Y. Jiao, Y. Yang, A. Lazarides, K. Hingerl, G. Bruno, A. Brown, and M. Losurdo, *Small* **8**, 2721–2730 (2012).

14 R. D. Deshpande, J. C. Li, Y. T. Cheng, and M. W. Verbrugge, *J. Electrochem. Soc.* **158**, A845–A849 (2011).

15 S. Zhu, J.-H. So, R. Mays, S. Desai, W. R. Barnes, B. Pourdeyhimi, and M. D. Dickey, *Adv. Funct. Mater.*, n/a-n/a (2012).

16 K. A. Dick, *Prog. Cryst. Growth Char. Mater.* **54**, 138–173 (2008).

17 H. L. Zhou, M. Pozuelo, R. F. Hicks, and S. Kodambaka, *J. Cryst. Growth* **319**, 25–30 (2011).

18 J. Fujita, R. Ueki, Y. Miyazawa, and T. Ichihashi, *J. Vac. Sci. Technol. B* **27**, 3063–3066 (2009).

19 H. Hiura, M. V. Lee, A. V. Tyurnina, and K. Tsukagoshi, *Carbon* **50**, 5076–5084 (2012).

20 R. Kometani, T. Ichihashi, S. Warisawa, and S. Ishihara, *Jpn. J. Appl. Phys.* **48**, 06FE01 (2009).

21 R. Ueki, T. Nishijima, T. Hikata, S. Ookubo, R. Utsunomiya, T. Matsuba, and J. Fujita, *Jpn. J. Appl. Phys.* **51**, 06FD28 (2012).

22 C. Y. Wang, Y. C. Chen, W. H. Chu, C. P. Liu, and C. B. Boothroyd, *J. Mater. Res.* **24**, 1388–1394 (2009).

23 J. Fujita, T. Ichihashi, S. Nakazawa, S. Okada, M. Ishida, Y. Ochiai, T. Kaito, and S. Matsui, *Appl. Phys. Lett.* **88**, 083109 (2006).

24 W. J. MoberlyChan, D. P. Adams, M. J. Aziz, G. Hobler, and T. Schenkel, *MRS Bull.* **32**, 424–432 (2007).

25 Q. Hu and W. O'Neill, *Appl. Surf. Sci.* **256**, 5952–5956 (2010).

26 C. C. Lee, G. Proust, G. Alici, G. M. Spinks, and J. M. Cairney, *J. Microsc.* **248**, 129–139 (2012).

27 P. Peter, B. Lothar, and S. Bernd, *Nanotechnology* **23**, 475304 (2012).

28 B. Keene, *Internat. Mater. Rev.* **38**, 157–192 (1993).

29 B. Alchagirov, and A. Mozgovoi, *High temp.* **43**, 791–792 (2005).

30 J. S. Chen, S. P. Lau, B. K. Tay, G. Y. Chen, Z. Sun, Y. Y. Tan, G. Tan, and J. W. Chai, *J. Appl. Phys.* **89**, 7814–7819 (2001).

31 D. R. Lide, CRC handbook of chemistry and physics, CRC press (2012).

32 K. F. McCarty, J. A. Nobel, and N. C. Bartelt, *Nature* **412**, 622–625 (2001).

33 S. Kodambaka, S. V. Khare, W. Swiech, K. Ohmori, I. Petrov, and J. E. Greene, *Nature* **429**, 49–52 (2004).

34 S. Kodambaka, N. Israeli, J. Bareno, W. Swiech, K. Ohmori, I. Petrov, and J. E. Greene, *Surf. Sci.* **560**, 53–62 (2004).

35 S. J. Tang, S. Kodambaka, W. Swiech, I. Petrov, C. P. Flynn, and T. C. Chiang, *Phys. Rev. Lett.* **96**, 126106 (2006).

CHAPTER 5 *IN SITU* TRANSMISSION ELECTRON MICROSCOPY OBSERVATIONS OF GA DYNAMICS ON FOCUSED ION BEAM MILLED SURFACES

5.1 Abstract

Over the last 35 years, focused-ion beam systems have become well-established as versatile tools for analyzing and fabricating nanostructures. One of the consequences of Ga-based ion milling is the implantation of Ga^+ ions into milled and deposited materials. Using *in situ* transmission electron microscopy (TEM) on cross-sectional samples, we investigated the kinetics of liquid Ga droplet decay on FIB-deposited, amorphous thin carbon films during annealing at temperatures up to 800 °C. The TEM images reveal that liquid Ga nucleates and grows as spherical droplets above ~ 175 °C, then with increasing time at higher temperatures undergoes coarsening/decay, evaporation, or a novel phenomenon called regeneration.

5.2 Introduction

Gallium is commonly used as a liquid metal ion source (LMIS) in focused-ion beam (FIB) systems due to its low melting point (T_m = 29.8 °C)[1], low reactivity towards substrates (notably W emitter), and low vapor pressure (7.32×10^{-39} Torr at 298 K).[1,2] Since the first development of an LMIS-based scanning ion microscope in 1979,[3] the FIB has been improved over time into a common tool for milling materials.[4] Although the semiconductor industry dominates use of FIB systems for device fabrication, analysis, and transmission electron microscopy (TEM) sample preparation, other applications range from metallurgy, ceramics, and polymers, to biology, geology, medicine, and even art.[2] Applications typically require the FIB for preparation of samples; FIB milling is now routinely used to prepare high-quality cross-sectional or plan-view samples for TEM characterization.

Advantages of TEM samples via FIB-milling include site specificity of the milled area, preservation of the bulk material, reproducibility, high throughout relative to traditional polishing methods, and capacity for preparing samples from materials that are complex, delicate, or previously difficult to work with.[5,6] Despite the advances in ion-beam engineering, FIB-induced damage in TEM samples remains a problem – notably amorphization of layers in the milled material, redeposition of the sputtered material, and implantation of Ga^+ ions in the sample.[2,4,7–12] Studies have shown that the distribution of gallium in samples ranges widely and depends on parameters such as beam current, accelerating voltage, milling angle, and composition of the sample being milled.[2,11] Ga^+ introduced by FIB implantation can be difficult to detect and requires additional processing to avoid.[7–12]

The phenomenon of Ga^+ implantation can also be beneficial. Controlled FIB-implantation of Ga^+ has been used as a lithography etch stop, as the FIB can both etch desired structures as well as deposit a chemical mask that impedes etching.[13–18] FIB implantation-based techniques have been utilized to fabricate structures such as nanopillar arrays, quantum wells, heterostructure quantum wires, and field effect transistors.[15–21] In addition, Ga droplets prepared by FIB implantation have been used to control seeding and self-assembly of nanostructures.[22–24] The FIB is a versatile tool for nanoscale patterning, deposition, and sample preparation. However, the dynamics of Ga metal from Ga^+ implantation are not well-studied. Droplet kinetics and positioning at high temperatures are of interest to the controlled growth of nanostructures, such as group-III-catalyzed III-V nanowires (e.g., GaAs, InP).[25-27] Here, we investigate the dynamics of Ga droplets resulting from heating of FIB-prepared cross-section TEM samples at temperatures up to 800 °C, showing droplet generation (nucleation and growth), coalescence, Ostwald ripening, evaporation, and a phenomenon that we refer to as “regeneration”.

5.3 Materials and Methods

All of our experiments were carried out using an Al_2O_3(0001) substrate (10 mm × 10 mm × 1 mm) from MTI Co. The substrate was cleaned by sonication (10 min) and rinsing first in acetone, and then in isopropanol. A 15 ± 5 nm layer of ~80:20 Au:Pd was sputter-deposited onto the polished surface to facilitate higher-resolution imaging and precision milling with electron and ion beams. Cross-sectional TEM (XTEM) samples were prepared by typical lift-out methods (described below and in Figure 5.1) in an FEI Nova 600 Nanolab DualBeam FIB system equipped with a scanning electron microscope (SEM) and facilities for electron- and ion-beam assisted deposition of Pt, W, and C.

Prior to milling, the Al_2O_3(0001) surface was protected with a 1.5 ± 0.5 μm thick layer of amorphous carbon, deposited first using 5 kV and 6.3 nA electron beams (~ 0.5 μm), followed by 30 kV and 0.3 nA ion beams (~ 1 μm). Trenches were cut out of the bulk substrate using 30 kV and 20 nA ion beams, creating a ~ 20 μm × 2 μm thin section. The XTEM sample was then attached to a nanomanipulator needle, milled out of the substrate, and glued with ion-beam-deposited Pt to a commercial Mo lift-out grid (Figures 5.2A and B). The needle tip and excess Pt were cut from the sample and the sample was further thinned to electron transparency by 10 kV and 0.12 nA ion beams (Figure 5.2C). This final step involved making a 2° wedge-shaped sample with thinner top and thicker bottom for structural integrity. Samples were then removed from the SEM/FIB vacuum chamber and stored in air at room temperature. Each sample was prepared using the same FIB parameters on the same Al_2O_3(0001) substrate.

Each of the carbon-coated Al_2O_3 (C/Al_2O_3) XTEM samples was mounted in a single-tilt Hummingbird Scientific holder, and heated *in situ* in an FEI 120kV Tecnai 12 TEM or FEI 300 kV Titan scanning TEM (S/TEM). Typical annealing of the XTEMs involved heating the

samples at temperatures T between 100 °C and 500 °C. The temperature was raised in 50 K or 100 K increments and held at each T for times t = 10 or 15 minutes to minimize thermal drift. *Ex situ* SEM and energy-dispersive x-ray spectroscopy (EDS) measurements were performed in an FEI Nova NanoSEM 230, operated at an accelerating voltage of 10 kV. Droplet diameters d and heights h were measured using ImageJ, either manually for fewer droplets or through thresholding and automatic particle counting for large ensembles of droplets with high contrast.

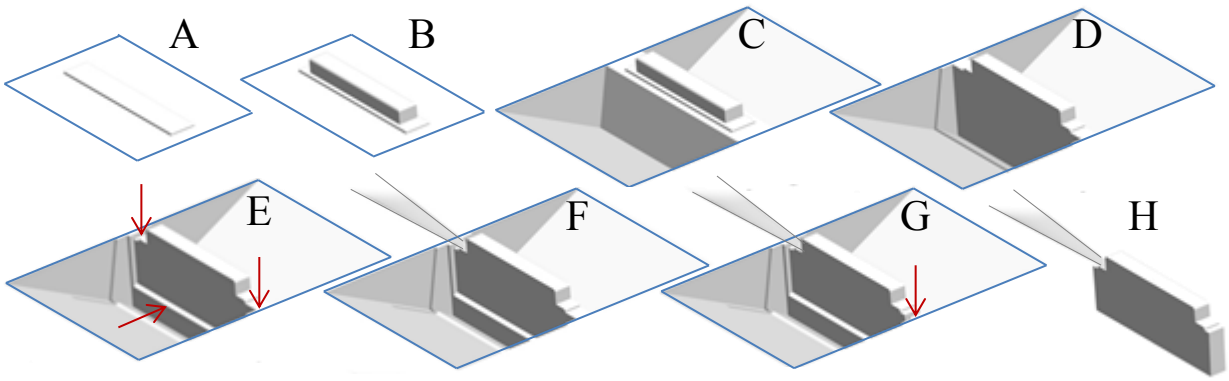

Figure 5.1 Schematic of XTEM lift-out sample preparation: (A) C deposition with e-beam onto the substrate surface, (B) Second, thicker layer of C deposition with ion-beam, (C) Initial cross-sectioning (angled) of trenches on two sides of the sample, (D) Cleaning to make the two sample sides parallel, (E) Partial cutting (U-cut, indicated by arrows) of sample to prepare for complete detachment from bulk, (F) Needle insertion and attachment via Pt deposition to the XTEM piece, (G) Final milling to remove XTEM material, and (H) XTEM sample removed from bulk and adhered to the needle, to be attached by C deposition to a lift-out TEM grid and thinned to final electron transparency. Adapted from personal correspondence and from original figure by Noah Bodzin, UCLA Nanoelectronics Research Facility.

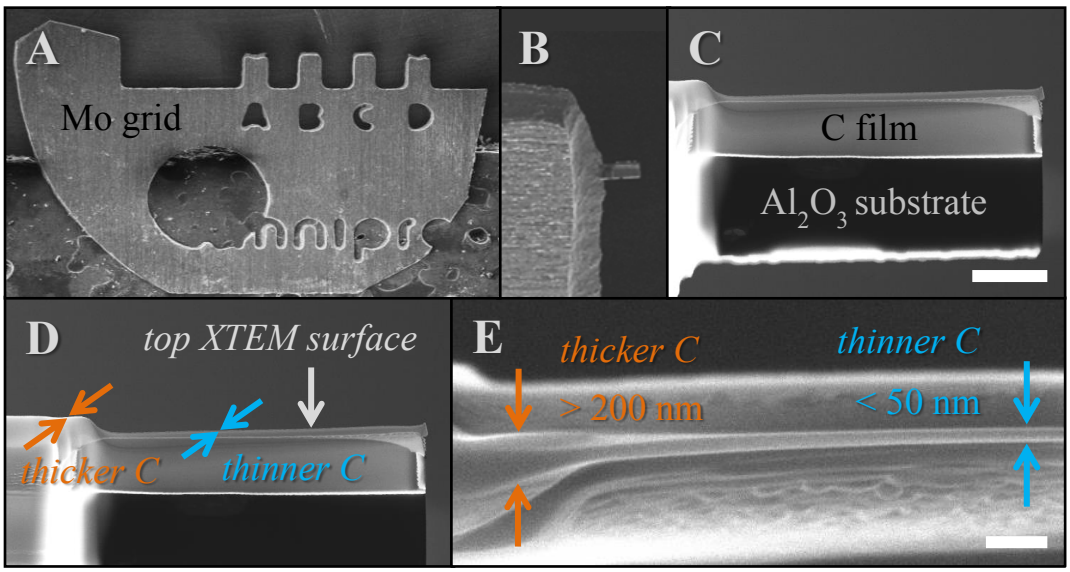

Figure 5.2 SEM images of a typical XTEM sample used in our experiments. (A) Commercial molybdenum lift-out grid from Omniprobe, with four sample posts labeled A – D. The right is side manually cut to fit into a 2.3 mm diameter heating holder. (B) Magnified area of post B, showing a TEM cross-section attached to the side. (C) Cross-sectional view of C/Al_2O_3(0001) interface after final FIB thinning to TEM transparency and attachment to the post with ion-deposited carbon. Scale bar = 2 µm. (D) Cross-sectional view of the XTEM sample, with arrows indicating areas of the C film with different thicknesses. (E) Top view with arrows indicating thicker and thinner areas of the C film, corresponding approximately to the areas indicated in (D). Scale bar = 200 nm.

5.4 Results and Discussion

5.4.1 Nucleation and Growth of Ga Droplets

Previous studies by our group and others have demonstrated that FIB milling and FIB-induced deposition of thin films lead to implantation of Ga^+ ions.[28,29] Although Ga^+ is typically not visible in the SEM or TEM after implantation, heating FIB-milled structures can induce the formation of large liquid Ga droplets on the surfaces of milled or deposited layers.[30,31] Due to the large difference in surface energies, liquid gallium does not wet amorphous C and forms droplets with wetting angles exceeding 120°, as seen here.[25,32–34] This correlates with the observation of Ga preferentially forming spherical droplets on C films, as opposed to wetting the substrate.

In all of our *in situ* experiments, heating samples to T = 175 ~ 200 °C results in the formation of nearly spherical droplets within a few seconds along the edges of the C film. This process of forming Ga droplets is highly reproducible; we have also obtained Ga droplets on carbon films from FIB-prepared XTEM samples of C/Ti/Si, $Zr/Al_2O_3(0001)$, and $ZrB_2/Al_2O_3(0001)$ substrates. The size and coverage of these Ga droplets, however, vary with the heating rate, T, t, and C film thickness. Prior to heating, droplets are not visible on the surface (Figures 5.2, 5.4A, and 5.9B). Selected area electron diffraction (SAED) patterns acquired from the samples indicate that both the droplets and C layers are amorphous and remain so during heating. Before annealing, EDS measurements across the thinned TEM section did not reveal the presence of Ga, presumably due to low concentration and distribution of Ga^+ implantation across the sample; only carbon, oxygen, and aluminum were detected, corresponding to the substrate materials (Figure 5.3). EDS data from droplets remaining on the XTEMs after annealing contained a majority of Ga. Although a fraction of oxygen was also detected, this is likely due to air exposure after removal from the TEM.

In our experiments, Ga droplets form preferentially at C/vacuum interfaces in the XTEM samples, typically along the top edge of the C film (labeled in Figure 5.2). Thicker (> 100 nm) C layers deposited using the FIB (Figures 5.2D and 5.1E) generally produce both larger and more numerous Ga droplets (Figure 5.4); this is due greater amounts of deposited C containing more implanted ions, and thus a higher amount of Ga^+ source. Initial formation of droplets is observed between $T \approx$ 175 °C and 200 °C and occurs rapidly – within 0.2 s, the standard TEM exposure time in live view. Typical droplet diameters in our experiments vary from ~ 10 nm at initial times, to ~ 2 μm after annealing for 95 min at temperatures from 100 °C to 450 °C (Figure 5.9C).

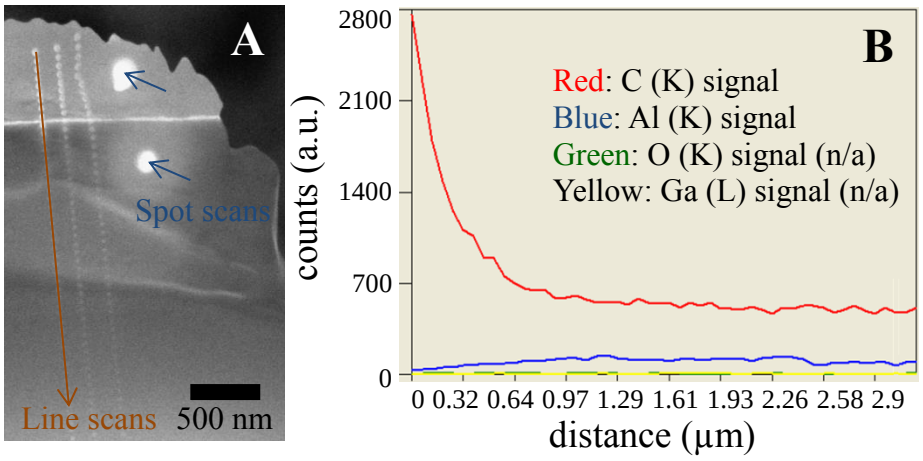

Figure 5.3 Energy-dispersive x-ray spectroscopy (EDS) analysis of a typical XTEM sample prior to heating: (A) Scanning electron micrograph of sample after EDS scans, showing contamination of the sample where the e-beam was held to measure data (two extended spot scans and three line scans). (B) Plot of counts vs. distance for the rightmost line scan in (A), with distance measured from top to bottom of the indicated line. Carbon and aluminum have the strongest signal, with trace amounts of oxygen and no gallium; the Ga signal is listed due to setting its detection in the EDS software, however quantification of the data shows 0% Ga in the sample prior to annealing. After annealing below the evaporation temperature, EDS analysis of large remaining droplets (similar to those in Figure 5.9C) shows that the droplets are primarily composed of Ga (~ 95 wt %, with the remaining signal from surface oxidation). After annealing droplets to the point of evaporation, no more than 2 or 3 small droplets are visible outside the field of view of the TEM images. EDS analysis of these leftover particles shows that they are primarily composed of C, O, and Al, with little to no Ga signal. We note that the Al signal is from a combination of the Al_2O_3 substrate and the Al holder.

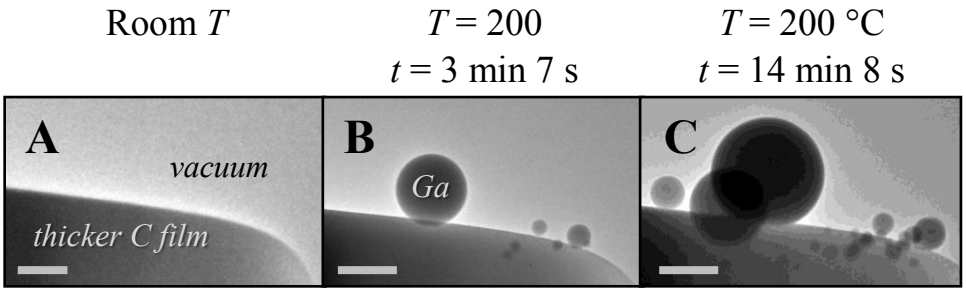

Figure 5.4 Sequence of *in situ* TEM images showing nucleation and growth of Ga droplets at T = 200 °C, on the thicker area of amorphous C film. This XTEM sample is typical of all heating experiments, where liquid Ga droplets appear ~ 175 °C.

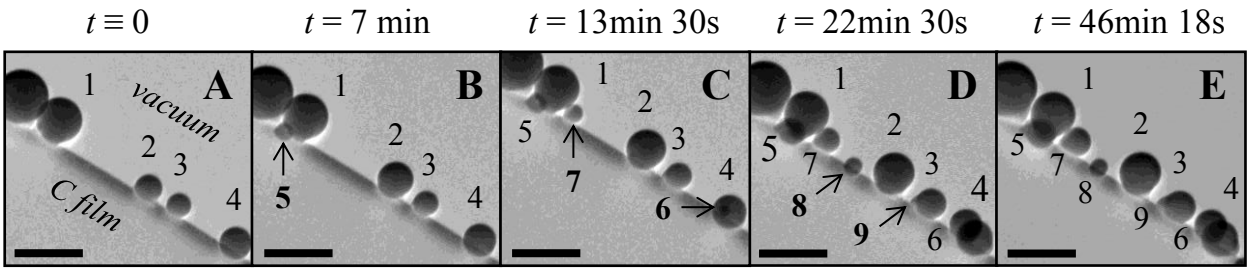

Figure 5.5 *In situ* TEM images of typical Ga droplets formed at the C/vacuum interface of XTEMs during annealing at 300 °C. Here, the label t = 0 min in the first image corresponds to 34 min after the temperature was raised from room temperature to 300 °C. Droplet nucleation and growth events are observed at different times across the C substrate. Droplet #6 forms behind #4 in (C) and is better seen in (D) when it is larger. As time progresses, all droplets increase in size. Scale bars = 200 nm.

At T < 400 °C, regardless of the number density or size all droplets primarily nucleate and grow, with no observation of ripening and few coalescence events. At T > 400 °C, nucleation and growth may compete with other phenomena, as discussed in the next sections. Figure 5.5 shows typical bright-field TEM images obtained from an XTEM sample during annealing at T = 300 °C. The droplets are situation at the top C/vacuum interface, across the thinner area of C film. In this experiment the sample T was increased from room temperature to 300 °C over 10 minutes, then held at 300 °C for 3 hours. Five droplets are visible in Figure 5.5A, and as time progresses we observe the formation and the growth of new droplets #5 – #9 (Figures 5.5B–E). All the droplets at these annealing temperatures grow larger over time, regardless of the size. This is, decay of droplets via Ostwald ripening is not dominant at this range of T. Outside the field of view presented here, other droplets act similarly: nucleation and growth dominate Ga droplet.

5.4.2 Ostwald Ripening of Ga Droplets

At T > 400 °C, we observe coarsening and decay of Ga droplets. Figures 5.6 and 5.7 show Ostwald ripening of droplets during annealing at T = 400 °C and 450 °C, respectively. This behavior is qualitatively similar to the droplet decay observed previously at 500 °C.[22] Here, for the sample shown in Figure 5.6, annealing at 100 °C (5 min) did not result in droplet formation, and subsequent annealing at 200 °C (10 min) and 300 °C (20 min) produced only three large droplets outside the field of view, on the thicker area of C film. While increasing the sample temperature from 300 °C to 400 °C, several hundred droplets precipitated across the C film (Figure 9A). At T = 400 °C, we begin to observe gradual Ostwald ripening.

Histograms of droplet diameters (Figures 5.6D–F), obtained from the TEM images shown in Figures 5.6A–C, show that the number of smaller droplets decreases while the number of larger droplets increases – indicative of ripening. Droplets with diameter less than 10 nm decay completely and droplets larger than 25 nm increase in diameter by 4 ~ 5 nm within 20 minutes. The average diameter $\langle d \rangle$ increases from ~ 30 nm at t = 0 min, to ~ 44 nm at t = 20 min. Figure 5.7 is a log-log plot of $\langle d \rangle$ vs. t for both annealing temperatures. The solid lines are linear least-squares fit to the data, where slope n of a line is the scaling exponent of the form $d \propto t^n$. For coarsening at T = 400 °C we obtain n = 0.35 ± 0.03, and n = 0.51 ± 0.4 at T = 450 °C. These values are closer to the mean field theory predicted value of n = 1/3 for coarsening/decay in the attachment-limited regime, rather than n = ¼ for diffusion-limited decay kinetics. Thus, we suggest that Ostwald ripening here is controlled by attachment/detachment mechanisms, as opposed to our previous study where ripening occurred in the diffusion-limited regime.[22]

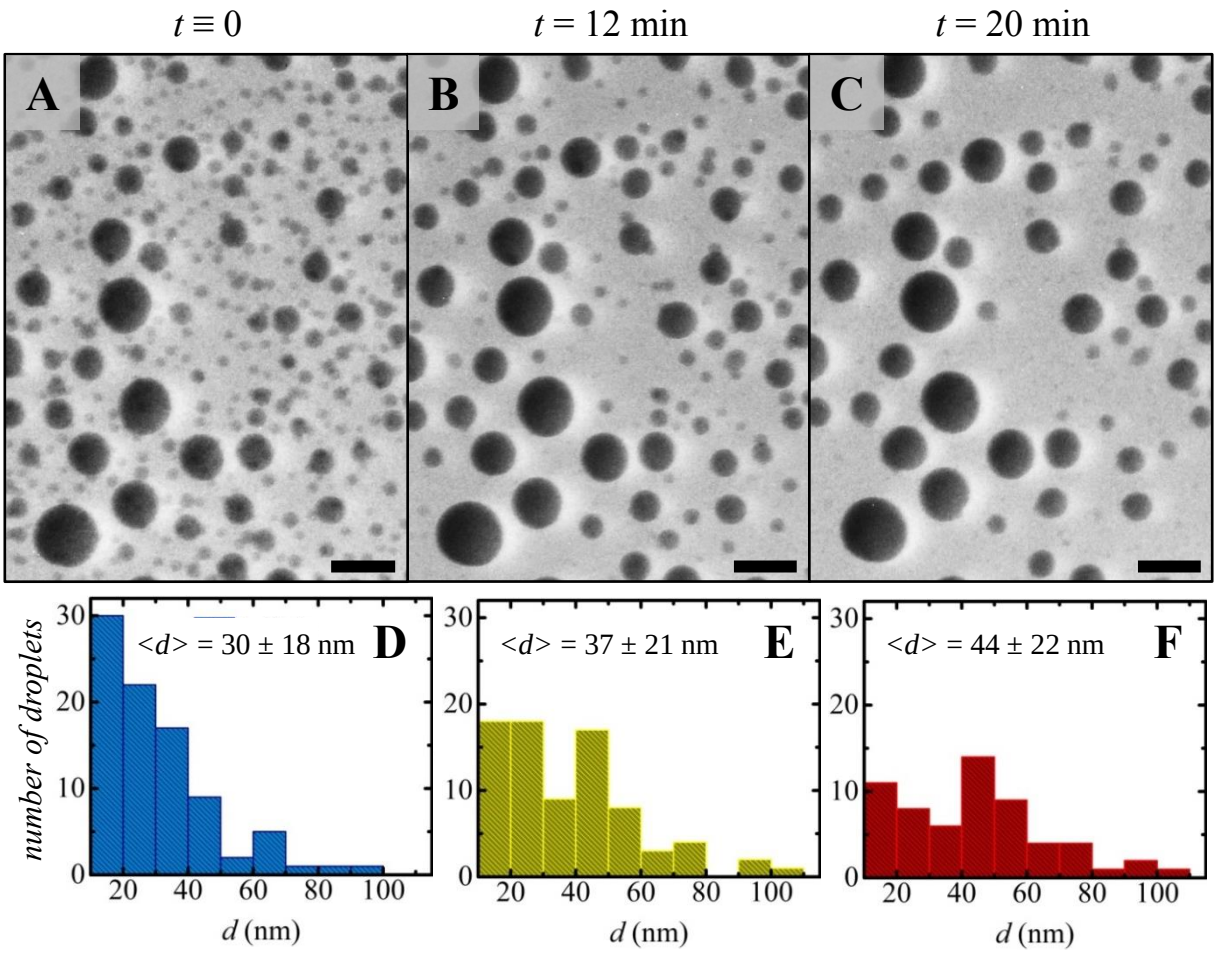

Figure 5.6 (A-C) *In situ* TEM images of Ga droplets observed on the surface of a C/Al_2O_3(0001) XTEM sample during annealing at T = 400 °C. Here, the label t = 0 corresponds to 35 min after the sample temperature was raised from room temperature to 400 °C. The majority of small droplets disappear while the larger droplets increase in diameter by an average ~ 7 nm. Scale bars = 100nm. (D-F) Histograms of droplet sizes in each TEM image show a decrease in the number density and increase in overall size of the droplets. Also, the average droplet diameter <d> increases from 30 ± 18 nm at t = 0 to 44 ± 22 nm at t = 20 min.

At the higher annealing temperature (T = 450 °C) we observe similar Ostwald ripening of droplets, although with an increased rate of decay over shorter times (Figure 5.9). Most of the droplets decrease significantly in size or disappear after 20 min, leaving behind several larger droplets up to ~ 200 nm in diameter (Figure 5.9F). Outside the TEM field of view, much larger Ga droplets (up to ~ 2 μm in diameter) are observed on the sample (Figure 5.8C). The existence of these massive droplets reinforces our hypothesis that mass is conserved and that observed

droplet decay is due to Ostwald ripening: larger droplets presumably grew at the expense of the smaller droplets that disappear.

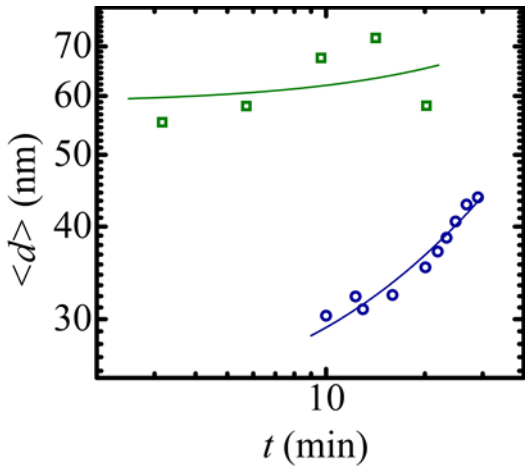

Figure 5.7 Log-log plots of average diameter <*d*> vs. time *t* for the droplet ensembles at *T* = 400 °C (blue circles) and *T* = 450 °C (green squares), resulting in *n* values of 0.35 ± 0.3 nm and 0.51 ± 0.4, respectively.

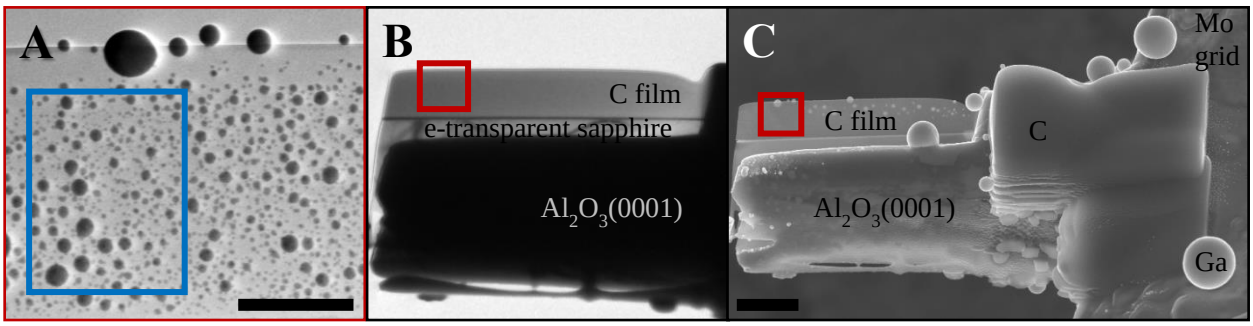

Figure 5.8 Low magnification imaging of the XTEM sample from Figures 5.6 and 5.9. The red boxes in (B) and (C) correspond to the field of view in (A), and the blue box in (A) corresponds to the field of view in Figures 5.6. (A) TEM image of droplets generated after annealing at 400 °C for 6 min, after the sample temperature was raised from room temperature to *T* = 400 °C for 35 min. The largest droplets nucleate at the C/vacuum interface, while the majority of smaller droplets are located across the amorphous film. Scale bar = 500 nm. (B) TEM image of the sample prior to heating, showing no Ga droplets. The dark line at the C-substrate interface is a layer of Ag-Pd sputtered onto the Al_2O_3(0001) before FIB milling; the layer does not change during the subsequent annealing. (C) SEM image of the sample after annealing for a total of 5 min at *T* = 100 °C, 10 min at *T* = 200 °C, 20 min at *T* = 300 °C, 30 min at *T* = 400 °C, and 30 min at *T* = 450 °C. Very large Ga droplets (as confirmed by energy-dispersive spectroscopy) with bright contrast remaining on the surface, outside the field of view of the TEM images. Scale bar = 2 µm.

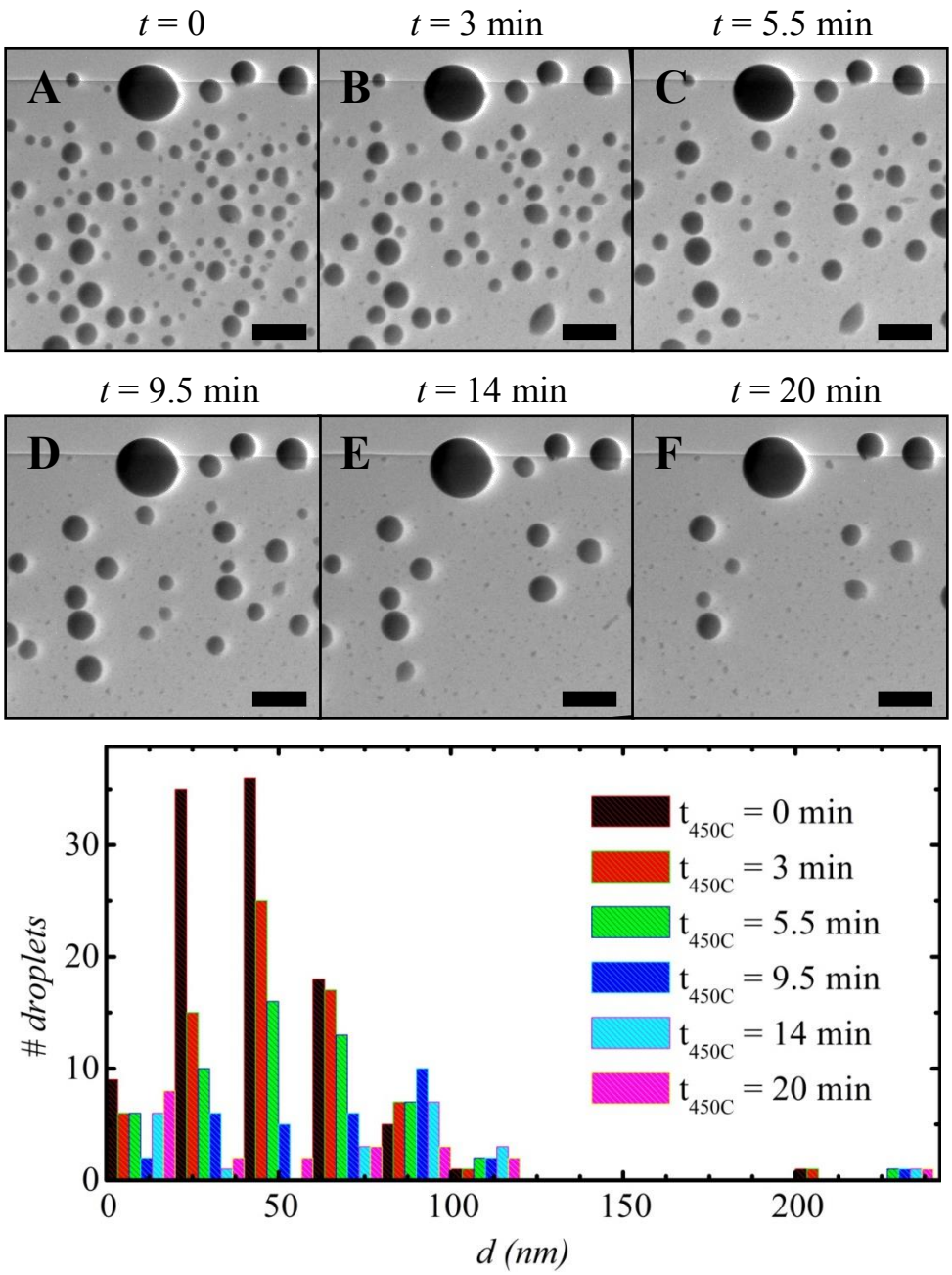

Figure 5.9 Sequence of *in situ* TEM images of the Ga droplets from Figure 6, showing faster Ostwald ripening at a higher temperature. Here, the label t = 0 corresponds to 65 min after the sample temperature was raised from room temperature to 450 °C. Between (A) and (B), two droplets in the lower right corner of the images coalesce together into an elongated droplet before disappearing in (C). Otherwise, only ripening is observed. As time progresses, the majority of droplets shrink to very small size or disappear while larger droplets increase in size minimally. In confirmation of ripening theory, outside the field of view much larger droplets have grown, as seen in Figure 5.8C. The histogram shows that as time progresses, the number density of droplets decreases while the average sizes of droplets increase – indicative of Ostwald ripening. Scale bars = 200 nm.

5.4.3 Regeneration of Ga Droplets

In addition to droplet nucleation, growth, and ripening, we have observed a new phenomenon during the annealing of XTEM samples: droplet "regeneration".[35] In this process, a smaller Ga droplet nucleates and grows at one site, then is consumed by a larger adjacent droplet; subsequently, a similar-sized droplet begins growing at the same location. Cycles of repetitive growth and disappearance of Ga droplets are seen in many of our FIB-prepared TEM samples. Figure 5.10 shows regeneration of one such droplet during annealing of an XTEM sample at 400 °C. Previous studies have demonstrated reversible transport of liquid metal along carbon nanotubes,[36] as well as an oscillator with indium droplets.[37] Here, in contrast to previous experiments where the liquid metal mass is conserved, the droplet volume increases with time.

The regeneration process is irreversible and results from a finite source of implanted Ga^+. Disappearance of the smaller droplet can be attributed to coalescence with the larger droplet, given that it disappears soon after the two appear to come in contact. However, the regeneration of another droplet at the same site is unusual; this behavior is reminiscent of Ga droplets nucleating on GaAs surfaces from the formation of etch pits remaining after droplet coalescence.[38] Previous studies indicate that FIB milling leads not only to Ga^+ implantation, but also the creation of surface defects that act as preferential sites for nucleation.[39] Thus, it is likely that Ga implanted within the substrate diffuses out of these sites and forms Ga droplets at the same locations, instead of occurring at new locations across the substrate surface. The schematic in Figure 12 shows the process of implanted gallium ions clustering below the surface of the substrate. With annealing, the clusters then diffuse “upwards” to the surface (experimentally, the topmost C/vacuum interface), where Ga droplets nucleate at the defect sites. Upon nucleation, the droplets grow as the existing droplets act as sinks for Ga atoms diffusing out of the substrate.

The regeneration process thus continues due to the preferential nucleation at the same defect sites, coalescence, and continued transport of the Ga source to droplets at the surface.

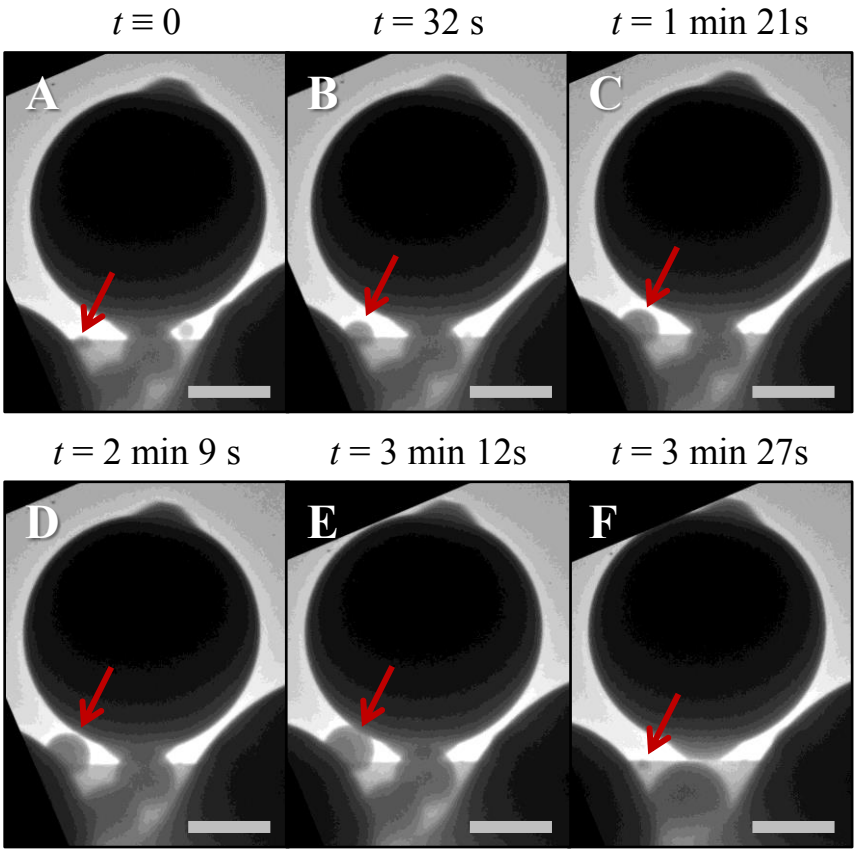

Figure 5.10 *In situ* TEM images of Ga droplets on a C/Al_2O_3(0001) XTEM sample during annealing at T = 400 °C. Here, the label t = 0 corresponds to 47 min after the sample temperature was raised from room temperature to 400 °C. The C film substrate is the medium-contrast grey area near the bottom of the images. In these images, a small droplet (indicated by the red arrow) has started to grow at (A) t = 0 and its size increases until after (E) t = 3 min 12 s. Between images (E) and (F), the droplet disappears and another begins growing at the same site. The process of nucleation-growth-disappearance repeats over a dozen times in this and other samples. Scale bars = 300 nm.

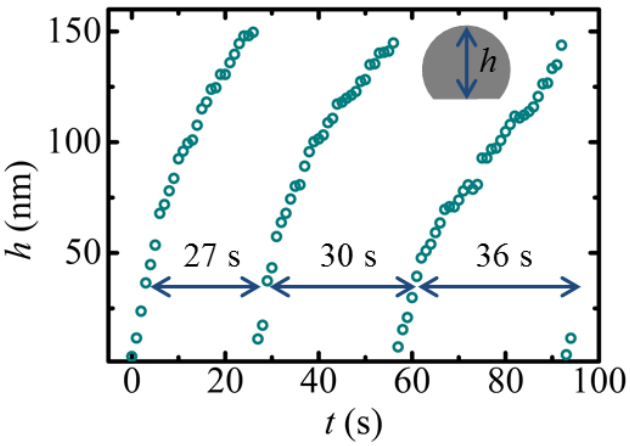

Figure 5.11 Plot of droplet height (h) vs. time (t) for three complete cycles of the regenerating droplet in Figure 10, extracted from individual frames of a video during annealing at T = 400 °C. Here, h is defined as the projected distance measured from the substrate to the top of the droplet, as illustrated in the inset. The time interval for the regeneration process increases with time, from 27 ± 0.3 s, to 30 ± 0.3 s, to 36 ± 0.3 s and the corresponding maximum droplet heights are 149 nm, 145 nm, and 143 nm, respectively. The error for all height measurements is ~ 10 nm.

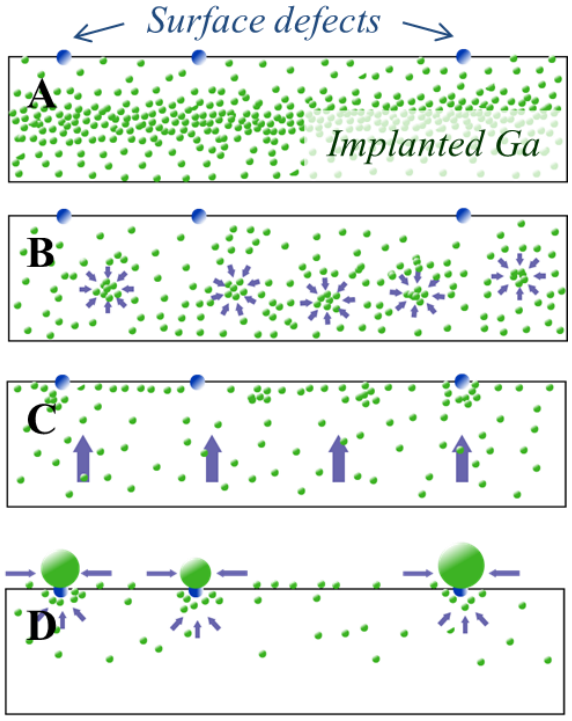

Figure 5.12 Schematic showing: (A) Ga^+ as implanted by FIB milling in a nominal substrate, (B) Clustering of the Ga ions below the surface as the temperature is increased, (C) Diffusion of Ga atoms and liquid metal clusters towards the substrate surface, and (D) Formation of liquid Ga spheres with preferential nucleation and pinning at defects to produce droplet growth at stationary locations. Adapted from Philipp, Bischoff, and Schmidt (2012).[25]

We envision that the out-flux of Ga from the substrate is initially high and constant, giving rise to the observed repetitive regeneration of droplets. This regeneration process is shown by the plot of droplet height as a function of time (Figure 5.11). The set of data for this plot is extracted from a video obtained prior to acquiring the TEM images in Figure 5.10. Comparing the regeneration cycles shown in Figures 5.10 and 5.11, the time interval between each cycle increases from ~ 30 s (Figure 5.11Figure 5.11) to ~ 200 s (Figure 5.10), over the 7 min elapsed between figures. The decrease in regeneration cycle at later times suggests that the out-flux of Ga decreases with time. We suggest that this behavior is due to depletion of Ga from the substrate with continued annealing. Since a finite amount of Ga^+ is implanted in the sample during XTEM preparation, the amount of Ga available for the nucleation and growth of droplets is limited. Initially, there is a larger concentration of implanted ions and thus a higher flux of Ga to the surface upon heating. As time progresses, Ga^+ concentration is the sample is lower and the time taken to form Ga droplets increases. Thus, as the implanted source for forming droplets decreases, so also the rate of regeneration decreases.

Both regeneration and Ostwald ripening are observed in a similar temperature regime, T = 350 °C – 500 °C. However, we note that only one or the other phenomenon is dominant and thus observed in a given sample. We find that the regeneration process is dominant on thicker areas of C film, while ripening occurs between droplets that are spread over the thinner areas of the substrate. The regeneration process is driven by high out-flux of Ga, a criterion best satisfied in regions with thicker C film and higher levels of implanted Ga^+. In contrast, ripening occurs in areas with thinner C and subsequently less Ga^+ source; this implies that most of the Ga has precipitated from the thin film, giving rise to droplet coarsening instead of continued nucleation and growth.

5.4.4 Evaporation of Ga droplets

At higher temperatures ($T \geq 500$ °C) all the droplets disappear within a few minutes and leave behind tiny, stable particles. Figure 5.13 shows time-lapsed TEM images obtained at T = 550 °C. In this field of view, spanning across approximately half of the top thin C film of an XTEM, droplets of sizes between 90 nm and 190 nm disappear within 33 minutes. Plotting diameter d vs. t for these droplets shows that irrespective of the decay behavior at initial times, late-stage decay of all the droplets is similar (Figure 5.14). The smallest droplets in Figure 5.13A (d < 133 nm) are the first to completely decay within 5 min (#5, #6, #16 in Figure 5.13B), while the largest droplets (d > 175 nm) are the last to diminish in size (#1, #4, #9, #7 in Figures 5.13H and I). In the sequence of images we observe that all droplets decay at different rates, regardless of size and location. For example, the first five droplets range in size from ~ 120 nm (droplet #5) to ~ 182 nm (droplet #4), and take completely different times to fully disappear: from less than 5 min (droplet #5) to the full 33 min (droplet #1). Also, droplets #11 through #15 are all ~ 155 nm in diameter and disappear at different times over 25 minutes; droplet # 15 is minimized by t = 13 min, droplets #11, #13, and #14 are minimized by t = 17 min, and droplets #12 is not minimized until t = 25 min.

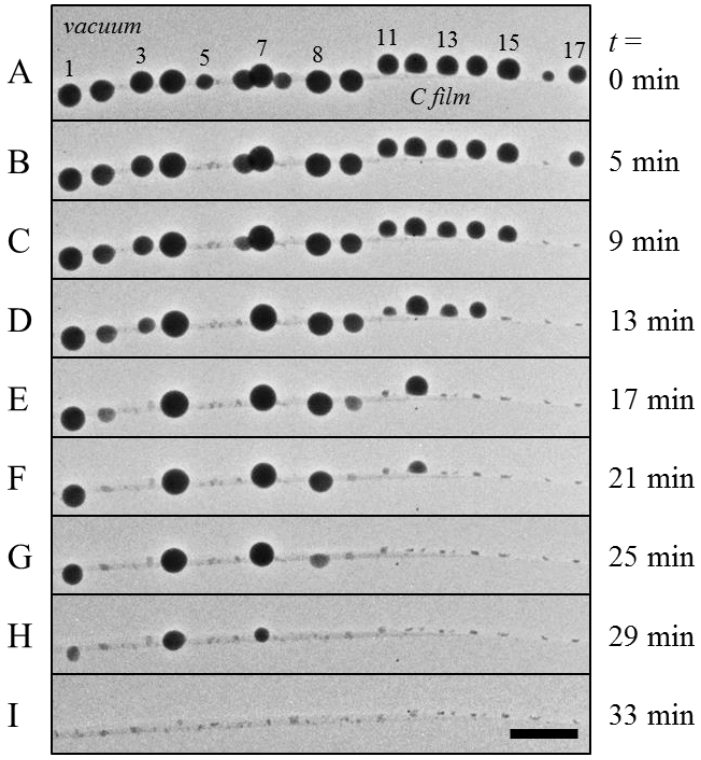

Figure 5.13 *In situ* TEM images showing 17 spherical Ga droplets disappearing during annealing at T = 550 °C. Here, the label t = 0 min corresponds to 90 min after the sample temperature was raised from room temperature to 550 °C. All of the liquid droplets in (A) disappear and leave behind small solid particles in (I), over the course of 33 min. Original droplet diameters range from 90 nm – 190 nm. Scale bar = 500 nm.

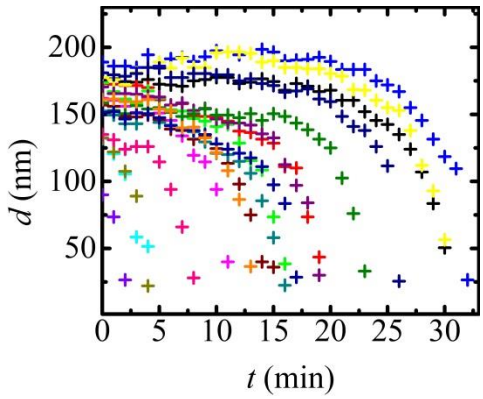

Figure 5.14 Plot of diameter d vs. time for the droplets in Figure 5.13, showing that droplets decay quickly at different times while overall having similar decay slopes. For clarity in the figure, each plot is truncated after the droplet area minimizes; the last value corresponds to the size of the remnant oxide particles visible in Figure 13I, which do not change in size. The point-to-point variation in measurements is due to error from the low magnification TEM images. In the images, one pixel corresponds to ~ 5 nm and error from diameter measurements is up to ~ 30 nm. Hence, the variations in the actual values of the measurements (up to 10 nm) are less than the inherent measurement error.

Initially, the behavior of these droplets suggests Ostwald ripening, given that the smaller droplets decay first and the larger ones decay last. Also, the difference of decay rates in similarly-sized droplets located next to each other may be due to some droplets growing at the expense of others, resulting in the growing droplets appearing to decay more slowly. However, in contrast to the previous instances of ripening at lower temperatures (T < 500 °C), very little droplet material is left on the XTEM after annealing and there is no conservation of Ga mass. We propose that while the droplets annealed at T = 550 °C initially decay by Ostwald ripening, the majority of droplets evaporate away. For a more isolated selection of droplets annealed at T = 500 °C and 550 °C on a thin C post, we observe that two droplets of diameter ~ 600 nm and ~ 200 nm evaporate over a similar period of time (Figure 5.15).

Droplet evaporation occurs well below the boiling temperature of Ga (2229 °C)[1] due to increased vapor pressure at elevated temperatures (3.62×10^{-10} Torr at 500 °C versus 7.31×10^{-39} at 25 °C)[1] and in vacuum. *Ex situ* SEM and EDS characterization of the XTEMs after annealing show that the vast majority of droplets and Ga signal are gone. In contrast, XTEMs heated at lower temperatures ($T \leq$ 450 °C) show large Ga droplets on XTEMs even after annealing for over an hour and observing decay via Ostwald ripening (Figure 5.8C). The majority elements in all EDS measurements are typically C, followed by Al and O from the substrate, and Mo from the TEM grid, depending on what area of the sample was measured.

Interestingly, although the droplets are formed *in situ* from a pure Ga source, there remain small, solid particles after the liquid Ga is evaporated away (Figures 5.13I, 5.15L); these particles are stable at temperatures up to 800 °C and are clearly visible in both SEM and TEM after annealing. The formation of solid material is attributed to air exposure of the samples after FIB milling and prior to TEM annealing in high vacuum. Because gallium metal readily forms a

surface oxide of 0.5 – 3 nm thickness,[40-44] it is reasonable to assume that some amount of gallium oxide forms on Ga droplet surfaces. SAED analysis of the remnant particles produces faint rings that correspond to β-Ga_2O_3 (T_m = 1795 °C), the only stable oxide of Ga.[45,46] (Figure 5.16) The presence of these remnant particles is typical of our experiments where liquid Ga droplets were heated to high temperatures (~ 500 °C – 800 °C).

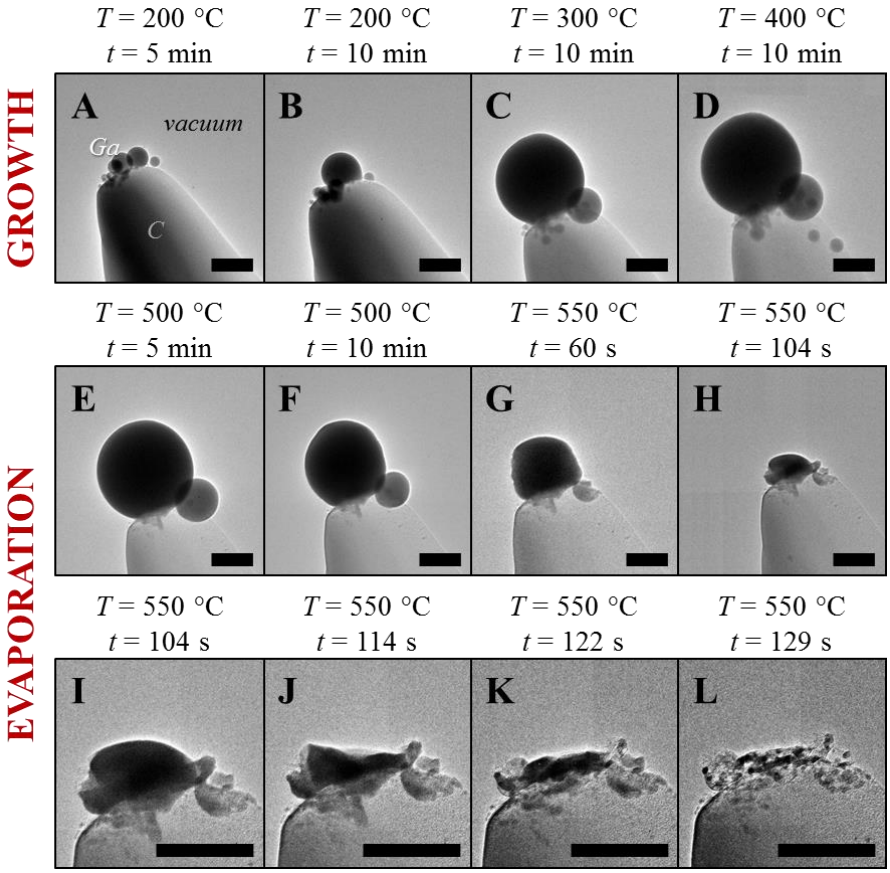

Figure 5.15 *In situ* TEM images showing nucleation, growth, and evaporation of Ga droplets. (A) Generation of Ga droplets from FIB-implanted Ga+ ions at T = 200 °C. (B) Coalescence of at least two droplets to create the largest droplet at T = 200 °C. (C) Growth and ripening of the droplets at T = 300 °C. (D) Growth of the larger droplets and generation of several smaller ones at T = 400 °C. (E-F) Evaporation of the smallest droplets and slight decrease in size as the larger droplets begin evaporating at T = 500 °C. (G-H) Faster evaporation at T = 550 °C. (I-L) Higher magnification view of the droplets rapidly evaporating within 30 s. Small particles of gallium oxide (L) remain after annealing at T = 550 °C. The total annealing times at each temperature were: 15 min (200°C), 30 min (300°C), 15 min (400°C), 15 min (500°C), and 5 min (550°C). Scale bars = 200 nm.

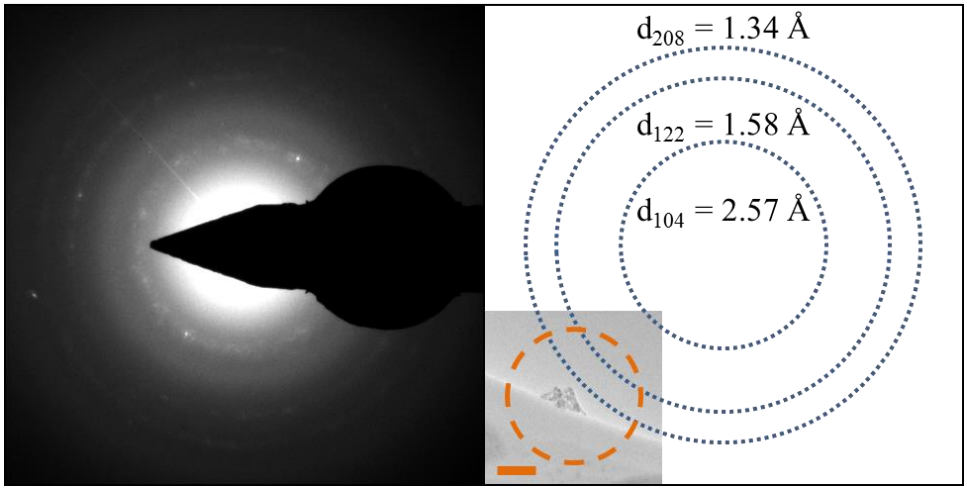

Figure 5.16 Representative selected area diffraction (SAED) at 700 °C of particles remaining after Ga droplets have evaporated away. The diffraction pattern was taken from the area shown in the inset by dashed orange lines. Scale bar = 200 nm. The dotted blue lines indicate the faint polycrystalline rings from the SAED pattern and are indexed to the β-Ga_2O_3 planes listed. Long exposure times (30 s) were necessary to produce visible diffraction from the small oxide particles.

5.5 Conclusions

In summary, we used *in situ* transmission electron microscopy to investigate the growth and decay behavior of liquid gallium droplets, which form on top of amorphous carbon layers prepared by focused-ion beam. For all XTEM samples annealed above T = 175 °C, Ga droplets nucleate and grow, while at temperatures from 350 °C – 450 °C, Ostwald ripening or regeneration may be observed. Regeneration occurs on thicker areas of C film, where there is more implanted Ga^+, while droplets undergo coarsening and decay across the thinner C film. Above 500 °C, the Ga metal decayed with a combination of Ostwald ripening and evaporation, leaving behind remnant particles of thermally stable β-Ga_2O_3. The work presented here provides insight into FIB-implanted gallium of XTEM samples and the surface dynamics of Ga droplets at high temperatures. Also, this work is useful towards *in situ* TEM studies at high temperatures and of low melting materials. Further understanding of this behavior and modification of sample

preparation can help achieve more controlled Ga^+ implantation, which can lead to the formation of Ga droplets with desired size and at select locations for patterned growth of quantum dots, nanowires, and other nanostructures.

5.6 Acknowledgements

This work was supported by funds from the Air Force Office of Scientific Research (FA9550–10–1–0496) and the NSF (CMMI-1200547). We thank Mr. Noah Bodzin and the Nanoelectronics Research Facility in the UCLA Henry Samueli School of Engineering for assistance with FIB milling. The authors acknowledge the use of instruments at the Electron Imaging Center for NanoMachines supported by NIH (1S10RR23057) and CNSI at UCLA.

5.7 References

1 W. M. Haynes, ed., CRC handbook of chemistry and physics, CRC press (2013).

2 L. A. Giannuzzi and F. A. Stevie, eds, "Introduction to focused ion beams: instrumentation, theory, techniques and practice" *Springer Science & Business Medi*a (2005).

3 R. L. Seliger, J. W. Ward, V. Wang, and R. L. Kubena, "A high-intensity scanning ion probe with submicrometer spot size" *App. Phys. Lett.* **34**, 310–312 (1979).

4 C. A. Volkert and A. M. Minor, "Focused Ion Beam Microscopy and Micromachining" *MRS Bull.* **32**, 389–399 (2007).

5 R. Anderson and S. J. Klepeis, "Practical aspects of FIB TEM specimen preparation" in Introduction to Focused Ion Beams, Springer US, 173-200 (2005).

6 M. W. Phaneuf, "FIB for materials science applications-A review" in Introduction to focused ion beams, Springer US, 143-172 (2005).

7 J. Mayer, L. A. Giannuzzi, T. Kamino, and J. Michael, "TEM sample preparation and FIB-induced damage" *MRS Bulletin* **32**, 400-407 (2007).

8 R. M. Langform, "Focused Ion Beams Techniques for Nanomaterials Characterization" *Microscopy Res. Tech.* **69**, 538–549 (2006).

9 N. I. Kato, "Reducing focused ion beam damage to transmission electron microscopy samples" *J. Electron Microscopy* **53**, 451–458 (2004).

10 S. Rubanov and P. R. Munroe, "FIB-induced damage in silicon" *J. Microscopy* **214**, 2130221 (2003).

11 T. Ishitani, K. Umemura, T. Ohnishi, T. Yaguchi, and T. Kamino, "Improvements in performance of focused ion beam cross-sectioning: aspects of ion-sample interaction" *J. Electron Microscopy* **53**, 443–449 (2004).

12 M. Tamura, S. Shukuri, M. Moniwa, and M. Default, "Focused ion beam gallium implantation in silicon" *Appl. Phys. A* **39**, 183–190 (1986).

13 K. D. Choquette and L. R. Harriott, "Dry lithography using focused ion beam implantation and reactive ion etching of SiO2" *Appl. Phys. Lett.* **62**, 3294–3296 (1993).

14 H. -C. Fang, J. -H. Huang, W. -H. Chu, and C. -P. Liu, "Ga^+ focused-ion-beam implantation-induced masking for H2 etching of ZnO films" *Nanotechnology* **21**, 505703 (2010).

15 N. Chekurov, K. Grigoras, A. Peltonen, S. Franssila, and I. Tittonen, "The fabrication of silicon nanostructures by local gallium implantation and cryogenic deep reactive ion tching" *Nanotechnology* **20**, 065307 (2009).

16 M. D. Henry, M. J. Shearn, B. Chhim, and A. Scherer, "Ga^+ beam lithography for nanoscale silicon reactive ion etching" *Nanotechnology* **21**, 245303 (2010).

17 P. Sievilä, N. Chekurov, and I. Tittonen, "The fabrication of Si nanostructures by FIB implantation and TMAH wet etching" *Nanotechnology* **21**, 145301 (2010).

18 Qian, H. X. , W. Zhou, J. Miao, L. E. N. Lim, and X. R. Zeng, "Fabrication of Si microstructures using focused ion beam implantation and reactive ion etching" *J. Micromechanics and Microengineering* **18**, 035003 (2008).

19 Y. Hirayama, S. Tarucha, Y. Suzuki, and H. Okamoto, "Fabrication of a GaAs quantum-well-wire structure by Ga focused-ion-beam implantation and its optical properties" *Phys. Rev. B* **37**, 2774 (1988).

20 M. Itoh, T. Saku, Y. Hirayama, and S. Tarucha, "Ga focused-ion-beam shallow-implanted quantum wires" *J. Vac. Sci. Tech. B: Microelectronics and Nanometer Structures* **15**, 1657–1660 (1997).

21 H. Kim, T. Noda, and H. Sakaki, "Formation of GaAs/AlGaAs constricted-channel field-effect transistor structures by focused Ga implantation and transport of electrons via focused ion beam induced localized states" *J. Vac. Sci. Tech. B* **16**, 2547–2550 (1998).

22 M. Kammler, R. Hull, M. C. Reuter, and F. M. Ross, "Lateral control of self-assembled island nucleation by focused-ion-beam micropatterning" *Appl. Phys. Lett.* **82**, 1093–1095 (2003).

23 Q. Wei, J. Lian, W. Lu, and L. Wang, "Highly ordered Ga nanodroplets on a GaAs surface formed by a focused ion beam" *Phys. Rev. Lett.* **100**, 076103 (2008).

24 A. Lugstein, B. Basnar, and E. Bertagnolli, "Size and site controlled Ga nanodots on GaAs seeded by focused ion beams" *J. Vac. Sci. Tech. B* **22**, 888–892 (2004).

25 S. Plissard, G. Larrieu, X. Wallart, and P. Caroff, "High yield of self-catalyzed GaAs nanowire arrays grown on Si via Ga droplet positioning" *Nanotech.* **22**, 275602 (2011).

26 B. Bauer, A. Rudolph, M. Soda, A. F. i Morral, J. Zweck, D. Schuh, and E. Reiger, "Position controlled self-catalyzed growth of GaAs nanowires by molecular beam epitaxy" *Nanotech* **21**, 435601 (2010).

27 A. F. Morral, "Gold-free GaAs nanowire synthesis and optical properties" *IEEE J. Selected Topics in Quantum Electronics* **17**, 819-828 (2011).

28 S. Kodambaka, C. Ngo, J. Palisaitis, P. H. Mayrhofer, L. Hultman, and P. O. Å. Persson, "Kinetics of Ga droplet decay on thin carbon films" *Appl. Phys. Lett.* **102**, 161601 (2013).

29 W. J. MoberlyChan, D. P. Adams, M. J. Aziz, G. Hobler, and T. Schenkel, "Fundamentals of focused ion beam nanostructural processing: Below, at, and above the surface" *MRS Bull.* **32**, 424–432 (2007).

30 R. Kometani, T. Ichihashi, S. Warisawa, and S. Ishihara, "Graphite Shell Film Formation Induced by Eduction Phenomenon of Ga Implanted by Focused Ion Beam" *Jpn. J. Appl. Phys., Part 1* **48**, 06FE01 (2009).

31 P. Phillipp, L. Bischoff, and B. Schmidt, "Taming of Ga droplets on DLC layers—size tuning and local arrangement with nanometer accuracy" *Nanotechnology* **23**, 475304 (2012).

32 J. Fujita, R. Ueki, Y. Miyazawa, and T. Ichihashi, "Graphitization at interface between amorphous carbon and liquid gallium for fabricating large area graphene sheets" *J. Vac. Sci. Technol. B* **27**, 3063–3066 (2009).

33 R. Ueki, T. Nishijima, T. Hikata, S. Ookubo, R. Utsunomiya, T. Matsuba, and J. Fujita, "In-situ Observation of Surface Graphitization of Gallium Droplet and Concentration of Carbon in Liquid Gallium" *Jpn. J. Appl. Phys., Part 1* **51**, 06FD28 (2012).

34 C. -Y. Wang, Y. -C. Chen, W. -H. Chu, C. -P. Liu, and C. B. Boothroyd, "Formation of carbon capsules from an amorphous carbon film by Ga and Ni/Co catalysts in a transmission electron microscope" *J. Mater. Res.* **24**, 1388–1394 (2009).

35 C.Ngo and S. Kodambaka, "*In situ* microscopy studies of liquid gallium droplet dynamics" *Microsc. Microanal.* **20**, 1634–1635 (2014).

36 B. C. Regan, S. Aloni, R. O. Ritchie, U. Dahmen, and A. Zettl, "Carbon nanotubes as nanoscale mass conveyors" *Nature* **428**, 924–927 (2004).

37 B. C. Regan, S. Aloni, K. Jensen, and A. Zettl, "Surface-tension-driven nanoelectromechanical relaxation oscillator" *Appl. Phys. Lett.* **86**, 123119 (2005).

38 J. Tersoff, D. E. Jesson, and W.-X. Tang, "Decomposition controlled by surface morphology during langmuir evaporation of GaAs" *Phys. Rev. Lett.* **105**, 035702 (2010).

39 P. Philipp, L. Bischoff, and B. Schmidt, "Taming of Ga droplets on DLC layers—size tuning and local arrangement with nanometer accuracy" *Nanotechnology* **23**, 475304 (2012).

40 M. Yarema, M. Wörle, M. D. Rossell, R. Erni, R. Caputo, L. Protesescu, K. V. Kravchyk, D. N. Dirin, K. Lienau, F. von Rohr, A. Schilling, M. Nachtegaal, and M. V. Kovalenko, "Monodisperse Colloidal Gallium Nanoparticles: Synthesis, Low Temperature Crystallization, Surface Plasmon Resonance and Li-Ion Storage" *J. Am. Chem. Soc.* **136**, 12422–12430 (2014).

41 A. Plech, U. Klemradt, H. Metzger, and J. Peisl, "*In situ* x-ray reflectivity study of the oxidation kinetics of liquid gallium and the liquid alloy" *J. Physics: Condensed Matter* **10**, 971 (1998).

42 H. Men and Z. Fan, "Transition of amorphous to crystalline oxide film in initial oxide overgrowth on liquid metals" *Mat. Sci. Tech.* **27**, 1033 (2011).

43 M. J. Regan, H. Tostmann, P. S. Pershan, O. M. Magnussen, E. DiMasi, B. M. Ocko, and M. Deutsch, "X-ray study of the oxidation of liquid-gallium surfaces" *Phys. Rev. B* **55**, 10786 (1997).

44 H. Tostmann, E. DiMasi, B. M. Ocko, M. Deutsch, and Peter S. Pershan, "X-ray studies of liquid metal surfaces" *J. Non-Cryst. Sol.* **250**, 182–190 (1999).

45 S.J. Schneider and J. L. Waring, "Phase equilibrium relations in the Sc2O3–Ga_2O_3 system" *J. Res. Nat. Bur. Stand. A* **67**, 19–25 (1963).

46 JCPDF #431013

CHAPTER 6

SUMMARY AND FUTURE WORK

6.1 Summary

This dissertation summarized research on the elucidation of growth mechanisms and kinetics for III-V/III materials as a function of their experimental conditions, namely InPSb nanowires and liquid Ga catalyst droplets fabricated by metalorganic chemical vapor deposition (MOCVD), molecular beam epitaxy (MBE), and focused ion beam (FIB) milling and implantation. Electron microscopy methods were the primary approach to studying these materials, particularly high-resolution transmission electron microscopy (HRTEM) and *in situ* TEM heating, providing additional fundamental understanding of the evolution and behavior of functional nanomaterials. Ternary, zinc blende alloy nanowires (or "nanocream cones") of $InP_{1-x}Sb_x$ grown at high precursor flux were shown to contain wurtzite phases at the droplet-wire interface, due to supersaturation and subsequent precipitation of hexagonal-structured InSb during cooling of Sb-rich In-Sb alloy droplets. Droplets of Ga with exposure to atmospheric oxygen were found to evaporate nonlinearly and deviate from the diameter-squared-law of evaporation, due to the strong influence of impurities accumulated over time – primarily a native oxide shell formed at the metal surface. Without the influence of surface oxidation, Ga droplets that were formed by FIB implantation and *in situ* annealing evaporated substantially more rapidly and at lower temperatures than the oxide-covered material. Below the evaporation temperature in vacuum, the *in situ* generated Ga droplets were shown to exhibit a variety of phenomena: Nucleation, growth, Ostwald ripening, coalescence, and regeneration; these behaviors were deduced to be a general function of annealing temperature.

6.2 Future Work

Continued mechanistic understanding of III-V nanowire growth and group III liquid catalyst kinetics allows further development of these materials towards practical applications. The ongoing challenge of producing defect-free III-V nanowires and heterostructures of desired crystal structure is contingent on comprehending the mechanisms by which undesired features such as twinning and stacking faults are formed during growth. Detailed control and understanding of required growth conditions are necessary to tune material parameters, thus creating control to allow for novel and functional optoelectronic applications. Additional studies are required to fully delve into the nuances behind InPSb and other ternary – and even binary – nanostructures, both by systematic variation of growth conditions and intuitive design fueled by fundamental knowledge and modeling/computation of growth systems.

At a more fundamental level, understanding the role and behavior of liquid metal catalyst droplets furthers the pursuit of controlled synthesis of 1D nanostructures. Extension of the *in situ* experiments presented in this work will first require more quantitative characterization approaches, particularly to quantify the amount and evolution of oxide shell during annealing – a complicated task that may be tackled by the use of quantitative *in situ* electron-energy-loss spectroscopy coupled with HRTEM, as well as novel synchrotron-based x-ray transmission microscopy studies (proposed for study at the SLAC National Accelerator Laboratory). Visually, *in situ* SEM studies would allow for approximate 3D evaluation of the oxide shell collapse during annealing (newly available with facilities at the UCLA Molecular and Nano Archaeology Lab), as well as concurrent energy-disbursive spectroscopy to monitor changes in signal intensity of the material as a function of temperature. Coupling SEM imaging and deposition with a customized *in situ* UHV system (housed by Kodambaka Lab), it will be possible to deposit truly

pure, oxygen-free gallium and other liquid metal droplets from a metalorganic source, and thus monitor pure droplet evolution as a function of time, temperature, flow, and other controllable experimental conditions. All of the methods developed in turn would be applicable to other systems based on metal catalysts, both with low-melting materials such as group III elements and other catalyst nanoparticles that are required to grow nanostructures.

As a whole, this work focused on the understanding and control of material behaviors during growth and annealing at elevated temperatures. Continued research into these fundamental processes will ultimately drive the development of next-generation materials for future applications, with less reliance on serendipitous discovery and more progress based on intuitive design.

APPENDIX

JOURNAL AUTHORIZATIONS TO USE COPYRIGHTED WORKS (CHAPTERS 2 AND 4)

A.1 Background

This appendix contains the rights retained by journal authors from the Journal of Crystal Growth and Applied Physics Letters, as well as email correspondence from the coauthors granting permission to use the publications as chapters in this thesis.

A.2 Rights retained by journal authors

A.2.1 Chapter 2 – Journal of Crystal Growth

INTRODUCTION

1. The publisher for this copyrighted material is Elsevier. By clicking "accept" in connection with completing this licensing transaction, you agree that the following terms and conditions apply to this transaction (along with the Billing and Payment terms and conditions established by Copyright Clearance Center, Inc. ("CCC"), at the time that you opened your Rightslink account and that are available at any time at http://myaccount.copyright.com).

GENERAL TERMS

2. Elsevier hereby grants you permission to reproduce the aforementioned material subject to the terms and conditions indicated.

3. Acknowledgement: If any part of the material to be used (for example, figures) has appeared in our publication with credit or acknowledgement to another source, permission must also be sought from that source. If such permission is not obtained then that material may not be included in your publication/copies. Suitable acknowledgement to the source must be made, either as a footnote or in a reference list at the end of your publication, as follows:

"Reprinted from *Journal of Crystal Growth*, Vol 336/Issue 1, Authors Chilan Ngo, Hailong Zhou, Matthew Mecklenburg, Marta Pozuelo, B.C. Regan, Q.F. Xiao, V.B. Shenoy, R.F. Hicks, and S. Kodambaka, 'Effect of precursor flux on compositional evolution in $InP_{1-x}Sb_x$ nanowires grown via self-catalyzed vapor–liquid–solid process', Pages 14–19, Copyright (2011), with permission from Elsevier." Also Lancet special credit - "Reprinted from The Lancet, Vol. number, Author(s), Title of article, Pages No., Copyright (Year), with permission from Elsevier."

4. Reproduction of this material is confined to the purpose and/or media for which permission is hereby given.

5. Altering/Modifying Material: Not Permitted. However figures and illustrations may be altered/adapted minimally to serve your work. Any other abbreviations, additions, deletions and/or any other alterations shall be made only with prior written authorization of Elsevier Ltd. (Please contact Elsevier at permissions@elsevier.com)

6. If the permission fee for the requested use of our material is waived in this instance, please be advised that your future requests for Elsevier materials may attract a fee.

7. Reservation of Rights: Publisher reserves all rights not specifically granted in the combination of (i) the license details provided by you and accepted in the course of this licensing transaction, (ii) these terms and conditions and (iii) CCC's Billing and Payment terms and conditions.

8. License Contingent Upon Payment: While you may exercise the rights licensed immediately upon issuance of the license at the end of the licensing process for the transaction, provided that you have disclosed complete and accurate details of your proposed use, no license is finally effective unless and until full payment is received from you (either by publisher or by CCC) as provided in CCC's Billing and Payment terms and conditions. If full payment is not received on a timely basis, then any license preliminarily granted shall be deemed automatically revoked and shall be void as if never granted. Further, in the event that you breach any of these terms and conditions or any of CCC's Billing and Payment terms and conditions, the license is automatically revoked and shall be void as if never granted. Use of materials as described in a revoked license, as well as any use of the materials beyond the scope of an unrevoked license,

may constitute copyright infringement and publisher reserves the right to take any and all action to protect its copyright in the materials.

9. Warranties: Publisher makes no representations or warranties with respect to the licensed material.

10. Indemnity: You hereby indemnify and agree to hold harmless publisher and CCC, and their respective officers, directors, employees and agents, from and against any and all claims arising out of your use of the licensed material other than as specifically authorized pursuant to this license.

11. No Transfer of License: This license is personal to you and may not be sublicensed, assigned, or transferred by you to any other person without publisher's written permission.

12. No Amendment Except in Writing: This license may not be amended except in a writing signed by both parties (or, in the case of publisher, by CCC on publisher's behalf).

13. Objection to Contrary Terms: Publisher hereby objects to any terms contained in any purchase order, acknowledgment, check endorsement or other writing prepared by you, which terms are inconsistent with these terms and conditions or CCC's Billing and Payment terms and conditions. These terms and conditions, together with CCC's Billing and Payment terms and conditions (which are incorporated herein), comprise the entire agreement between you and publisher (and CCC) concerning this licensing transaction. In the event of any conflict between your obligations established by these terms and conditions and those established by CCC's Billing and Payment terms and conditions, these terms and conditions shall control.

14. Revocation: Elsevier or Copyright Clearance Center may deny the permissions described in this License at their sole discretion, for any reason or no reason, with a full refund payable to you. Notice of such denial will be made using the contact information provided by you. Failure to receive such notice will not alter or invalidate the denial. In no event will Elsevier or Copyright Clearance Center be responsible or liable for any costs, expenses or damage incurred by you as a result of a denial of your permission request, other than a refund of the amount(s) paid by you to Elsevier and/or Copyright Clearance Center for denied permissions.

LIMITED LICENSE

The following terms and conditions apply only to specific license types:

15. **Translation**: This permission is granted for non-exclusive world **English** rights only unless your license was granted for translation rights. If you licensed translation rights you may only translate this content into the languages you requested. A professional translator must perform all translations and reproduce the content word for word preserving the integrity of the article. If this license is to re-use 1 or 2 figures then permission is granted for non-exclusive world rights in all languages.

16. **Posting licensed content on any Website**: The following terms and conditions apply as follows: Licensing material from an Elsevier journal: All content posted to the web site must maintain the copyright information line on the bottom of each image; A hyper-text must be included to the Homepage of the journal from which you are licensing at http://www.sciencedirect.com/science/journal/00220248 or the Elsevier homepage for books at http://www.elsevier.com; Central Storage: This license does not include permission for a scanned version of the material to be stored in a central repository such as that provided by Heron/XanEdu.

Licensing material from an Elsevier book: A hyper-text link must be included to the Elsevier homepage at http://www.elsevier.com . All content posted to the web site must maintain the copyright information line on the bottom of each image.

Posting licensed content on Electronic reserve: In addition to the above the following clauses are applicable: The web site must be password-protected and made available only to bona fide students registered on a relevant course. This permission is granted for 1 year only. You may obtain a new license for future website posting.

17. **For journal authors:** the following clauses are applicable in addition to the above:

Preprints:

A preprint is an author's own write-up of research results and analysis, it has not been peer-reviewed, nor has it had any other value added to it by a publisher (such as formatting, copyright, technical enhancement etc.).

Authors can share their preprints anywhere at any time. Preprints should not be added to or enhanced in any way in order to appear more like, or to substitute for, the final versions of articles however authors can update their preprints on arXiv or RePEc with their Accepted Author Manuscript (see below).

If accepted for publication, we encourage authors to link from the preprint to their formal publication via its DOI. Millions of researchers have access to the formal publications on ScienceDirect, and so links will help users to find, access, cite and use the best available version. Please note that Cell Press, The Lancet and some society-owned have different preprint policies. Information on these policies is available on the journal homepage.

Accepted Author Manuscripts: An accepted author manuscript is the manuscript of an article that has been accepted for publication and which typically includes author-incorporated changes suggested during submission, peer review and editor-author communications.

Authors can share their accepted author manuscript:

- – immediately
    - *via* their non-commercial person homepage or blog
    - by updating a preprint in arXiv or RePEc with the accepted manuscript
    - *via* their research institute or institutional repository for internal institutional uses or as part of an invitation-only research collaboration work-group
    - directly by providing copies to their students or to research collaborators for their personal use
    - for private scholarly sharing as part of an invitation-only work group on commercial sites with which Elsevier has an agreement

- – after the embargo period
    - *via* non-commercial hosting platforms such as their institutional repository
    - *via* commercial sites with which Elsevier has an agreement

In all cases accepted manuscripts should:

- – link to the formal publication via its DOI
- – bear a CC-BY-NC-ND license - this is easy to do
- – if aggregated with other manuscripts, for example in a repository or other site, be shared in alignment with our hosting policy not be added to or enhanced in any way to appear more like, or to substitute for, the published journal article.

Published journal article (JPA): A published journal article (PJA) is the definitive final record of published research that appears or will appear in the journal and embodies all value-adding publishing activities including peer review co-ordination, copy-editing, formatting, (if relevant) pagination and online enrichment.

Policies for sharing publishing journal articles differ for subscription and gold open access articles:

Subscription Articles: If you are an author, please share a link to your article rather than the full-text. Millions of researchers have access to the formal publications on ScienceDirect, and so links will help your users to find, access, cite, and use the best available version.

Theses and dissertations which contain embedded PJAs as part of the formal submission can be posted publicly by the awarding institution with DOI links back to the formal publications on ScienceDirect.

If you are affiliated with a library that subscribes to ScienceDirect you have additional private sharing rights for others' research accessed under that agreement. This includes use for classroom teaching and internal training at the institution (including use in course packs and courseware programs), and inclusion of the article for grant funding purposes.

Gold Open Access Articles: May be shared according to the author-selected end-user license and should contain a CrossMark logo, the end user license, and a DOI link to the formal publication on ScienceDirect.

Please refer to Elsevier's posting policy for further information.

18. **For book authors** the following clauses are applicable in addition to the above: Authors are permitted to place a brief summary of their work online only. You are not allowed to download and post the published electronic version of your chapter, nor may you scan the printed edition to create an electronic version. **Posting to a repository:** Authors are permitted to post a summary of their chapter only in their institution's repository.

19. **Thesis/Dissertation**: If your license is for use in a thesis/dissertation your thesis may be submitted to your institution in either print or electronic form. Should your thesis be published commercially, please reapply for permission. These requirements include permission for the Library and Archives of Canada to supply single copies, on demand, of the complete thesis and include permission for Proquest/UMI to supply single copies, on demand, of the complete thesis. Should your thesis be published commercially, please reapply for permission. Theses and dissertations which contain embedded PJAs as part of the formal submission can be posted publicly by the awarding institution with DOI links back to the formal publications on ScienceDirect.

Elsevier Open Access Terms and Conditions

You can publish open access with Elsevier in hundreds of open access journals or in nearly 2000 established subscription journals that support open access publishing. Permitted third party re-use of these open access articles is defined by the author's choice of Creative Commons user license. See our open access license policy for more information.

Terms & Conditions applicable to all Open Access articles published with Elsevier:

Any reuse of the article must not represent the author as endorsing the adaptation of the article nor should the article be modified in such a way as to damage the author's honour or reputation. If any changes have been made, such changes must be clearly indicated.

Commercial reuse includes:

- – Associating advertising with the full text of the Article
- – Charging fees for document delivery or access
- – Article aggregation
- – Systematic distribution via e-mail lists or share buttons

Posting or linking by commercial companies for use by customers of those companies.

A.2.2 Chapter 4 – Applied Physics Letters

AIP Publishing LLC -- Terms and Conditions: Permissions Uses

AIP Publishing LLC ("AIPP"") hereby grants to you the non-exclusive right and license to use and/or distribute the Material according to the use specified in your order, on a one-time basis, for the specified term, with a maximum distribution equal to the number that you have ordered. Any links or other content accompanying the Material are not the subject of this license.

1. You agree to include the following copyright and permission notice with the reproduction of the Material:"Reprinted with permission from [FULL CITATION]. Copyright [PUBLICATION YEAR], AIP Publishing LLC." For an article, the copyright and permission notice must be printed on the first page of the article or book chapter. For photographs, covers, or tables, the copyright and permission notice may appear with the Material, in a footnote, or in the reference list.

2. If you have licensed reuse of a figure, photograph, cover, or table, it is your responsibility to ensure that the material is original to AIPP and does not contain the copyright of another entity, and that the copyright notice of the figure, photograph, cover, or table does not indicate that it was reprinted by AIPP, with permission, from another source. Under no circumstances does AIPP, purport or intend to grant permission to reuse material to which it does not hold copyright.

3. You may not alter or modify the Material in any manner. You may translate the Material into another language only if you have licensed translation rights. You may not use the Material for promotional purposes. AIPP reserves all rights not specifically granted herein.

4. The foregoing license shall not take effect unless and until AIPP or its agent, Copyright Clearance Center, receives the Payment in accordance with Copyright Clearance Center Billing and Payment Terms and Conditions, which are incorporated herein by reference.

5. AIPP or the Copyright Clearance Center may, within two business days of granting this license, revoke the license for any reason whatsoever, with a full refund payable to you. Should you violate the terms of this license at any time, AIPP, AIP Publishing LLC, or Copyright Clearance Center may revoke the license with no refund to you. Notice of such revocation will be made using the contact information provided by you. Failure to receive such notice will not nullify the revocation.

6. AIPP makes no representations or warranties with respect to the Material. You agree to indemnify and hold harmless AIPP, AIP Publishing LLC, and their officers, directors, employees or agents from and against any and all claims arising out of your use of the Material other than as specifically authorized herein.

7. The permission granted herein is personal to you and is not transferable or assignable without the prior written permission of AIPP. This license may not be amended except in a writing signed by the party to be charged.

8. If purchase orders, acknowledgments or check endorsements are issued on any forms containing terms and conditions which are inconsistent with these provisions, such inconsistent terms and conditions shall be of no force and effect. This document, including the CCC Billing and Payment Terms and Conditions, shall be the entire agreement between the parties relating to the subject matter hereof.

This Agreement shall be governed by and construed in accordance with the laws of the State of New York. Both parties hereby submit to the jurisdiction of the courts of New York County for purposes of resolving any disputes that may arise hereunder.